2013

Biologically Inspired Energy Manager Design For The Greatt Residential Microgrid

Wen Fang
North Carolina Agricultural and Technical State University

Biologically Inspired Energy Manager Design for the GREATT Residential Microgrid

Wen Fang

North Carolina A&T State University

A dissertation submitted to the graduate faculty

in partial fulfillment of the requirements for the degree of

DOCTOR OF PHILOSOPHY

Department: Electrical and Computer Engineering

Major: Electrical Engineering

Major Professor: Dr. Gary L. Lebby

Greensboro, North Carolina

2013

School of Graduate Studies
North Carolina Agricultural and Technical State University
This is to certify that the Doctoral Dissertation of

Wen Fang

has met the dissertation requirements of
North Carolina Agricultural and Technical State University

Greensboro, North Carolina
2013

Approved by:

Dr. Gary L. Lebby Major Professor	Dr. Christopher C. Doss Committee Member
Dr. Albert C. Esterline Committee Member	Dr. Clinton B. Lee Committee Member
Dr. John C. Kelly Department Chair	Dr. Robert Y. Li Committee Member

Sanjiv Sarin, PhD
Dean, The Graduate School

Biographical Sketch

Wen Fang was born on November 23rd, 1983, in Shanghai, China to Qifei Fang and Shunhua Lu. He is the husband of Xiaojue Tao, the father of Emily Fang, and the elder brother of Hui Fang. In 2008, he received the Master of Science degree in Electrical Engineering from North Carolina Agricultural and Technical State University. In 2006 he received the Bachelor of Science degree in Electrical Engineering from Shanghai University of Electric Power. He is a summa cum laude candidate for the Doctor of Philosophy degree in Electrical Engineering.

Dedication

This dissertation is dedicated to my daughter, Emily Fang, my wife, Xiaojue Tao, my father, Qifei Fang, my mother, Shunhua Lu, and my twin brother, Hui Fang, for their love and encouragement.

Acknowledgements

Many people have helped me in my way of seeking the doctoral degree. For me, this dissertation not only stands a result of my hard research work, but also a gift to those who loves and supports me throughout my graduate years at aggie land.

First and foremost, my deepest gratitude goes to my advisor Professor Gary Lebby. I am very grateful for his guidance and wisdom throughout the long-term commitment. He encouraged me to stay focus on the biologically inspired technology and its potential applications on the smart microgrid. His constructive suggestion and advice help me improve this doctoral research a lot.

I also want to express my gratitude to my committee members: Dr. Robert Li, Dr. Clinton Lee, Dr. Albert Esterline and Dr. Christopher Doss. Their valuable suggestion and comments in the preliminary defense helped me narrow my topic and stay focus on the important matters. Many thanks to all the faculty members and staff members in the department of Electrical Engineering at A&T. Their supports and help made this research available.

I immensely appreciated the support from my colleagues and friends from the Institute of Green Renewable Energy and Technology Transfer (GREATT) especially the support from Kenneth Jones, Joseph Tabron, and Charles Winley.

Last, but certainly not least, I thank my family for their love and support. Without them, I could not have walked this far, and I dedicate this dissertation to them, especially for my lovely daughter and her mother.

Table of Contents

List of Figures

List of Tables

Abstract

A biologically inspired method, involving the design of an energy manager, for coordinating the operation of a hybrid renewable residential micro-grid is presented. Flexible optimization procedures that minimize the cost of renewable distribution generators based upon the climate and location of the load profile have been developed and modeled in simulation. A novel design of a dual channel converter system and its control system forms the distributed energy storage (DES) system that features the capability of balancing the power flow in the micro-grid (even in the grid-off mode). The proposed energy management system utilizes a back propagation neural network in order to predict the state of charge (SOC) of the DES, yielding the reference value of control variables, which allows the micro-grid to respond to the desired operation conditions rapidly fast with acceptable controller error. Preliminary results indicate that the DES system allows for the implementation of energy management strategies in a technically viable manner.

CHAPTER 1

Introduction

1.1 Problem Statement and Dissertation Objectives

Environmental, economic, technical and government incentives make it essential to promote deregulation of the current power system structure. Traditional centralized power systems are merging to a new revolutionary network concept, smart grid, which represents the people's best wishes of the next generation of the robust electricity grid. The emergence of distributed generation systems (DGs), including wind turbines, photovoltaics, fuel cells, internal combustion engines, and others, has opened new opportunities for electricity end users to generate power on site [1]. This fact introduces the microgrid concept, a fuzzy but constructive distribution network topic, which leads the direction for rethinking how to accomplish the desired distribution network restructuring and improvement. Furthermore, the microgrid brings various desired benefits, which include: increasing the reliability of power supplement; a high share of renewables which improves the environmental profile; high power quality decided by the local control system; low cost or no cost of the fossil fuel and its transportation [1-4].

In 2000, Baker and De Mello defined the microgrid as "the portion of an electric power distribution system located at the downstream of the distribution substation includes a variety of DGs and different types of end users of electricity" [5]. In this research, the microgrid only uses renewable energy technologies, including wind and solar power conversion systems, as the power generation methods to meet the general purpose of the Green Renewable Energy and Technology Transfer (GREATT).

In a given location where a renewable microgrid project is being considered, renewable energy resource assessment, residential load profile modeling, optimal sizing and control of the

DGs, DESs and energy management strategy developing are significantly different from those applied to the conventional power systems. The main reasons are: (1) "non-dispatchable" generation of the DGs, (2) fast dynamical controller design of the electronic interfaces, (3) different energy management concentration.

The implications of the above challenges on planning, control, and energy management strategy development and implementation of a renewable microgrid have never been comprehensively investigated.

The objectives of this dissertation are:

1. To develop a schematic to assess the natural resources and optimize the size of the renewable distributed generators at any given location based on historical climate measurements and load profile.
2. To develop a dynamic model of electronically-interfaced distributed generators and energy storages.
3. To develop the algorithm and controllers that ensure the microgrid is stable and meets the operational requirements by adjusting the related system parameters based on Objective 1 and 2.
4. To develop an energy management strategy that ensures microgrid stability in autonomous operation without shading the residential loads based on Objective 3.
5. To develop an artificial neural network based energy manager for learning and implementing the energy management strategy developed in Objective 4.

1.2 Dissertation Layout

The rest of this dissertation is organized as follows:

Chapter 2 introduces the probability modeling of the climate measurements, including the wind speed, the global solar radiation, and the air temperature. The residential load modeling applies the Fourier decomposition and regression method. The procedure of optimal sizing of the renewable DGs by the non-uniform simulated annealing is presented in the last section of this chapter.

Chapter 3 covers the dynamically modeling and controller design of the electronically interfaced DGs, including the solar and wind energy conversion systems, distributed energy storage system, and their associated power electronic interface systems.

Chapter 4 discusses the microgrid operation modes, and the challenge of microgrid power flow analysis in autonomous operation mode. The procedure of microgrid planning combined with system stable operation algorithm in autonomous mode is proposed in the last section of this chapter.

Chapter 5 introduces the back propagation neural network (BPN) and proposes the BPN based energy manager design. The co-operation procedure between the BPN based energy manager and the microgrid is concluded in the last section of this chapter.

Chapter 6 conducts an experimental case study of the biologically inspired energy manager design. The desired microgrid aims to support 1000 households in the study area located in Phoenix, Arizona. The experimental results demonstrate that the proposed methods can realize the desired functions fast and precisely. Compared with other methodologies, the predicted state of charge of the distributed energy storage by using the back-propagation neural network based energy manager is more accurate.

Chapter 7 provides the comprehensive summary and conclusions of the work undertaken in this dissertation and also suggests potential research topics for future studies.

CHAPTER 2

Optimal Sizing of Renewable Distributed Generators in a Residential Microgrid

2.1 Introduction

Compared with other distributed renewable energy generation technologies, photovoltaic (PV) systems and wind turbine (WT) generation systems are less limited by the geographical features and conditions for continuous power production. Considering the PV and WT are excited by different climate conditions, a hybrid PV and WT distributed generation system is a desired clean energy option for the microgrid autonomous operation. However, the main challenge to promote such a significant system is the cost of system installation, maintenance and operation. As a result, the optimally distributed generator sizing for reliable power supplement is extremely necessary for cost reduction.

2.2 Probability Modeling of Wind Speed

Different methods were applied to wind speed modeling. Soman presented a review of Wind Power and wind speed modeling methods with different time horizons [6]. All of the reviewed technologies, including numeric weather predictors (NWP), artificial neural networks (ANN), time-series models, and so on, focused on relative short-term forecasting in the time domain, compared with long-term micro grid planning. The main reason is that the wind speed is uncertain and stochastic in nature. Since the wind speed is a random variable, the long-term historical data is required for the probability model for the wind energy potential evaluation at any given location. Various probability models have been used to describe wind speed distribution. The histogram of the frequency versus wind speed shows that the two-parameter Weibull distribution function is the best model for representing common wind behavior, and it is

the most widely used model as well [7-9]. In this research, the Weibull distribution is applied to model the wind speed profile at a given location.

The two-parameter cumulative Weibull distribution function $F(u)$ is defined as [8-10]:

$$F(u) = 1 - \exp\left[-(u/c)^k\right] \tag{2.1}$$

where k is the Weibull shape parameter; c is the Weibull scale parameter, ms^{-1}; u is the sampled observations of wind speed, ms^{-1}.

The two-parameter probability density function $f(u)$ is defined as [8-10]:

$$f(u) = \frac{\partial F(u)}{\partial u} = \left(\frac{k}{c}\right)\left(\frac{u}{c}\right)^{k-1} \exp\left(-\left(\frac{u}{c}\right)^k\right) \tag{2.2}$$

Before the two-parameter Weibull distribution function model is applied to model the wind speed profile, the measured wind speeds that were not calm were stored into 25 classes as shown in Table 1, which are defined by National Climatic Data Center (NCDC) for the Wind Energy Resource Information System [10]. The upper wind speed limit is inclusive. The central wind speed of the 25th class is chosen as 43 ms^{-1}, as if the upper limit is 45.5 ms^{-1}. In reality, the upper limit of the last class is infinity.

The normalization equation for eliminating the calm frequency in each wind speed class is given as:

$$F_{i,n}(u) = \frac{F_i(u) - F_0}{1 - F_0} \qquad i = 1 \cdots 25 \tag{2.3}$$

where $F_i(u)$ is the cumulative distribution probability for the i_{th} wind speed class; $F_{i,n}(u)$ is the normalized cumulative distribution probability for the i_{th} wind speed class without the calm

periods, and F_0 is the probability of the calm periods. By emerging Equations 2.1 and 2.3, we can obtain the normalized non-calm cumulative probability for the i_{th} wind speed class.

$$F_{i,n}(u) = 1 - \exp\left[-(u/c)^k\right] \tag{2.4}$$

Table 1

25 Classes Used for Sorting the Non-Calm Wind Speeds.

Class	Wind Speed (m/s)		
	Lower	Upper	Central
1	0.5	1.5	1
2	1.5	2.5	2
3	2.5	3.5	3
.	.	.	.
.	.	.	.
19	18.5	19.5	19
20	19.5	20.5	20
21	20.5	25.5	23
22	25.5	30.5	28
23	30.5	35.5	33
24	35.5	40.5	38
25	40.5	inf.	43

Many methods can estimate the two parameters of the Weibull distribution, including Weibull probability plotting, hazard plotting technique, maximum likelihood estimator (MLE), and so on [11]. In this research, the least squares (LS) method is applied.

By taking the logarithm twice at both side of Equation 2.4, it transfers to:

$$\ln\left(-\left(1-F_{i,n}(u)\right)\right) = -k\ln(c) + k\ln(u) \tag{2.5}$$

If we let $y = \ln\left(-\left(1-F_{i,n}(u)\right)\right)$, $a = -k\cdot\ln(c)$, $b = k$, and $x = \ln(u)$, Equation 2.5 can be rewritten as:

$$y = a + bx \tag{2.6}$$

or in matrix form:

$$Y = W \cdot X \tag{2.7}$$

where $X = \left[\ln(u_i), 1\right]$; $Y = \ln\left(-\left(1 - F_{i,n}(u_i)\right)\right)$; $i = 1 \cdots 25$. By using the least squares method, the weight matrix W would be obtained by:

$$W = \begin{bmatrix} b \\ a \end{bmatrix} = \left(X^T X\right)^{-1} X^T Y \tag{2.8}$$

By using the method described above, the Weibull shape parameter k and scale parameter c can be estimated. Figure 1 shows the comparison between the probability density functions of the measured samples and the modeled results in May. The blue curve is the measured hourly wind speed probabilities, and the red curve is the simulated probabilities by using the Weibull distribution probability model. Figure 2 displays the comparison between the cumulative distribution functions of the measured samples and the modeled results in May. The blue curve is the measured hourly wind speed cumulative probabilities, and the red curve is the simulated cumulative probabilities by using the Weibull distribution probability model. Once the two parameters are estimated, the simulated Weibull distribution based wind speed model is constructed. The average wind speed $\overline{v}_j$ of the j_{th} month is defined as:

$$\overline{v}_j = \sum_{i=1}^{25} u_i \cdot p(u_i) \qquad j = 1 \cdots 12 \tag{2.9}$$

where i is the index of the wind speed classes, u_i is the central speed of the i_{th} wind speed class in the j_{th} month , and $p(u_i)$ is the probability of the i_{th} wind speed class. Usually, the wind

speeds are measured at anemometer height due to the wind shear, and it is significantly lower than the wind speeds at hub height.

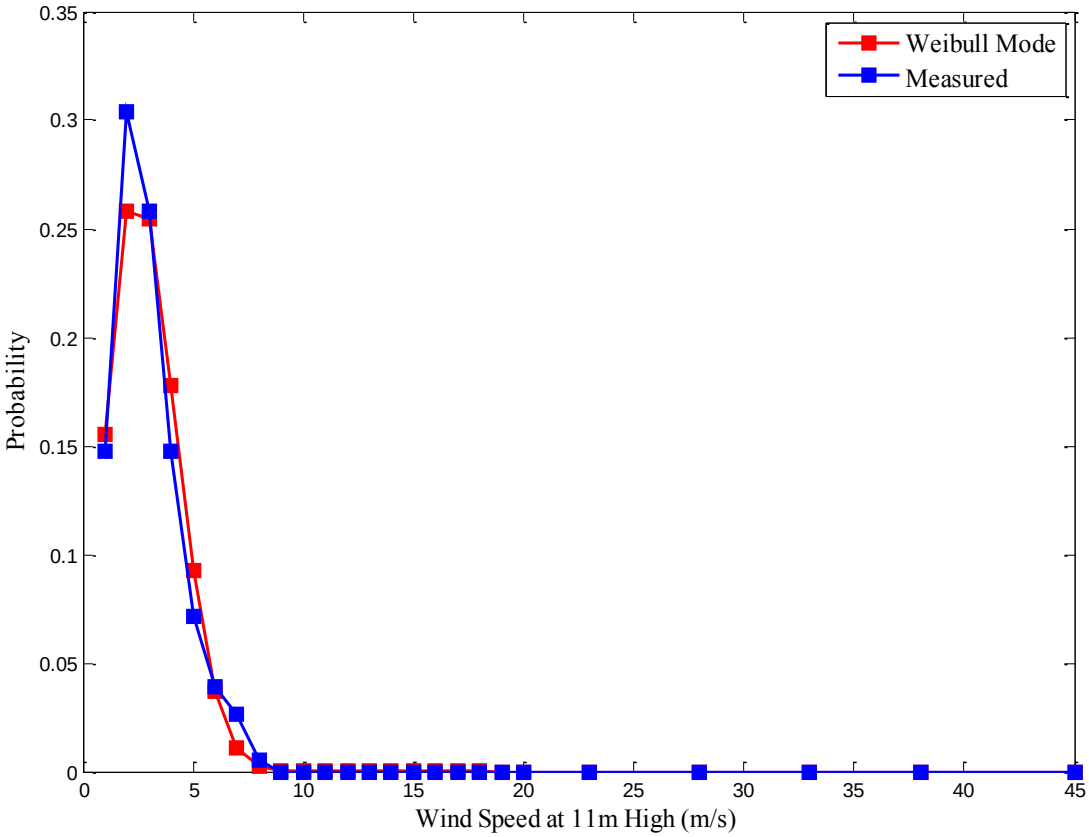

Figure 1. Comparison between the measured hourly wind speeds probability density function and the simulated Weibull distribution probability density function.

The power law equation is applied to calculate the average wind speed at hub height [8].

$$\frac{\bar{V}}{\bar{V}_0} = \left(\frac{H}{H_0} \right)^{\alpha} \tag{2.10}$$

where $\bar{V}$ is the average wind speed at hub height H, $\bar{V}_0$ is the wind speed at anemometer height H_0, and α is the wind shear exponent. In the low altitude, the wind shear exponent is approximately equal to 1.

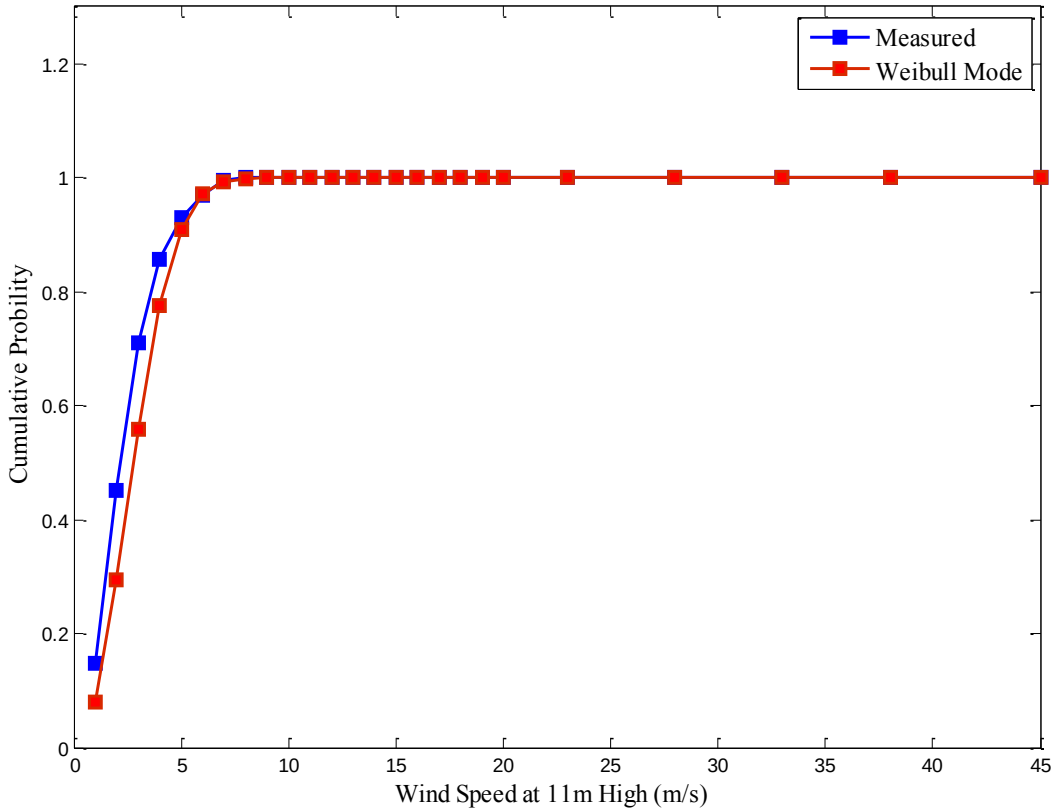

Figure 2. Comparison between the measured hourly wind speed cumulative probability function and the simulated Weibull distribution cumulative probability function.

2.3 Probability Modeling of Global Solar Radiation and Cell Temperature

The solar energy conversion at a specific site is decided by the global solar radiation received by the PV cells and the PV cell temperature [12].

Many previous studies have been made to model the behavior of global solar radiation directly or indirectly, and the most commonly used methods are based on the probability models. Assuncao proposed an hourly index frequency model of the solar radiation by using the Beta probability function [13]. Yaramoglu improved Assuncao's model that the solar radiation index was replaced by the cloud cover index [14].

In recent years, researchers focus on modeling the clearness indices or cloud cover indices by using different distribution functions, such as Weibull, Normal, Log-normal, Log-sigmoid, and so on. However, none of them are proved that it is generalized for any given location, and the physically based model is insufficient because of lack of measurements of all variables it needs. According to these difficulties, the average global solar radiation calculation in this section is only based on expected value $E(x)$ of measured samples without considering any pre-defined distribution functions.

Similarly, the global solar radiation is distributed to 25 pre-defined classes. Each class has equal step size based on the maximum and minimum observations during the research period.

If X is a discrete random variable with probability mass function $p(x)$, the expected value becomes:

$$E(X) = \sum_{i=1}^{n} x_i p(x_i) \tag{2.11}$$

Assume G contains n measured global solar radiation samples over a range of time, the mean global solar radiation over this range of time is:

$$E(G) = \sum_{i=1}^{n} g_i p(g_i) \tag{2.12}$$

where $E(G)$ is the discrete expected value of a vector contains n classes. In practical, random variables are classified into a number of classes, and replaced by the mean value g_i of samples in the i_{th} class. $p(g)$ is the probability density function of the vector G.

The cell temperature T_c is obtained by using the Normal Operating Cell Temperature (NOCT), listed on the PV module manufacturer datasheet [15]:

$$T_c = T_a + \left(NOCT - 20°C\right)\left(\frac{G}{800}\right) \tag{2.13}$$

Equation 2.12 can be revised and applied to calculate the average air temperature as:

$$E\left(T_a\right) = \sum_{i=1}^{n} t_{a,i}\, p\left(t_{a,i}\right) \tag{2.14}$$

and the average cell temperature is calculated as:

$$E(T_c) = E(T_a) + \left(NOCT - 20°C\right)\left(\frac{E(G)}{800}\right) \tag{2.15}$$

Once the average global solar radiation and air temperature are obtained, the average cell temperature is obtained.

2.4 Average Solar and Wind Power Calculation

The average monthly wind power converted $P_{WT_{avg,i}}$ for a particular wind energy conversion system can be calculated as:

$$P_{WT_{avg,i}} = C_p\left(\beta, \lambda_{opt}\right)\left(\frac{1}{2}\rho A {v_{w,avg,i}}^3\right) \tag{2.16}$$

where C_p is the wind power extraction fraction; λ_{opt} is the optimal tip speed ratio; β is the blade pitch angle; ρ is air density; A is the blade swept area; $v_{w,avg,i}$ is the average wind speed in the i_{th} month obtained from the wind speed probability model. The detailed information of Equation 2.16 will be discussed in the next chapter.

The average hourly solar power converted $P_{solar_{avg,i}}$ for a particular solar energy conversion system in the i_{th} month can be calculated as:

$$P_{solar_{avg,i}} = I_{avg,i} \cdot V_{opt,i} \tag{2.17}$$

where $I_{avg,i}$ is the average hourly terminal current outputs under the maximum power point tracking in the i_{th} month; $V_{opt,i}$ is the optimal terminal voltage, which yields to the maximum power output in the i_{th} month. The detailed information of Equation 2.17 will be discussed in the next chapter.

2.5 Residential Load Modeling

This section concentrates on the modeling of residential power loads using the Fourier series decomposition of historical loads. A general residential power load model can be divided in to three components shown in Figure 3. Compared with the wind speed model and global solar radiation model, the residential power load can be modeled based on its periodical features. As shown in Figure 4, the hourly average residential load curve over 2 years has an obvious character of seasonal effects, which are summer cooling and winter heating. This fact can be written as:

$$Load = Load_{Base} + Load_{Growth} + Load_{Seasonal} \tag{2.18}$$

By using the Fourier series decomposition, Equation 2.18 can be rewritten as:

$$\begin{aligned} RL_i = {} & b_0 + b_1 m_i + b_2 \cos(\omega_0 m_i) + b_3 \sin(\omega_0 m_i) + b_4 \cos(2\omega_0 m_i) \\ & + b_5 \sin(2\omega_0 m_i) + \cdots + b_{2n} \cos(n\omega_0 m_i) + b_{2n+1} \sin(n\omega_0 m_i) \end{aligned} \tag{2.19}$$

where b_0 is the base load, b_1 is the linear growth rate, b_2 to b_{2n+1} are the coefficients of Fourier fundamental and the harmonics, m_i represents the i_{th} month, $\omega_0 = \frac{2\pi}{12} = \frac{\pi}{6}$ is the fundamental frequency, which means there are two peaks in a year if using the monthly data, and $n \cdot \omega_0 = n \cdot \frac{\pi}{6}$ represents the frequency of the n_{th} order harmonic.

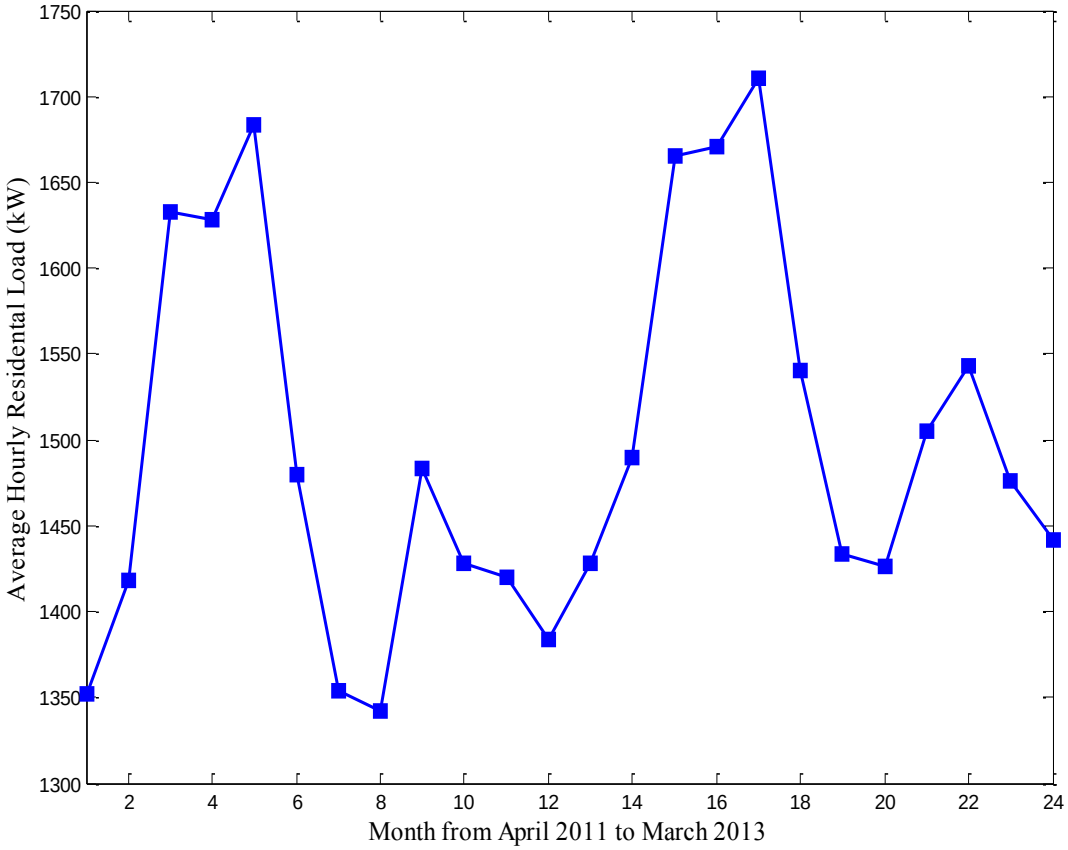

Figure 3. Average hourly residential load curve.

Equation 2.19 can be rewritten in the matrix form as Equations 2.20 and 2.21, and solved by the least square method as shown in Equation 2.22.

$$X = \begin{bmatrix} 1 & 1 & \sin(\omega_0) & \cos(\omega_0) & \sin(2\omega_0) & \cos(2\omega_0) & \cdots & \sin(n\omega_0) & \cos(n\omega_0) \\ 1 & 2 & \sin(\omega_0 2) & \cos(\omega_0 2) & \sin(2\omega_0 2) & \cos(2\omega_0 2) & \cdots & \sin(n\omega_0 2) & \cos(n\omega_0 2) \\ \vdots & \vdots & \vdots & \vdots & \vdots & \vdots & \ddots & \vdots & \vdots \\ 1 & N & \sin(\omega_0 N) & \cos(\omega_0 N) & \sin(2\omega_0 N) & \cos(2\omega_0 N) & \cdots & \sin(n\omega_0 N) & \cos(n\omega_0 N) \end{bmatrix} \tag{2.20}$$

$$Y = \begin{bmatrix} RL_1 \\ RL_2 \\ \vdots \\ RL_N \end{bmatrix} \tag{2.21}$$

then

$$W = \begin{bmatrix} b_0 \\ b_1 \\ \vdots \\ b_{2n+1} \end{bmatrix} = \left(X^T X \right)^{-1} X^T Y \tag{2.22}$$

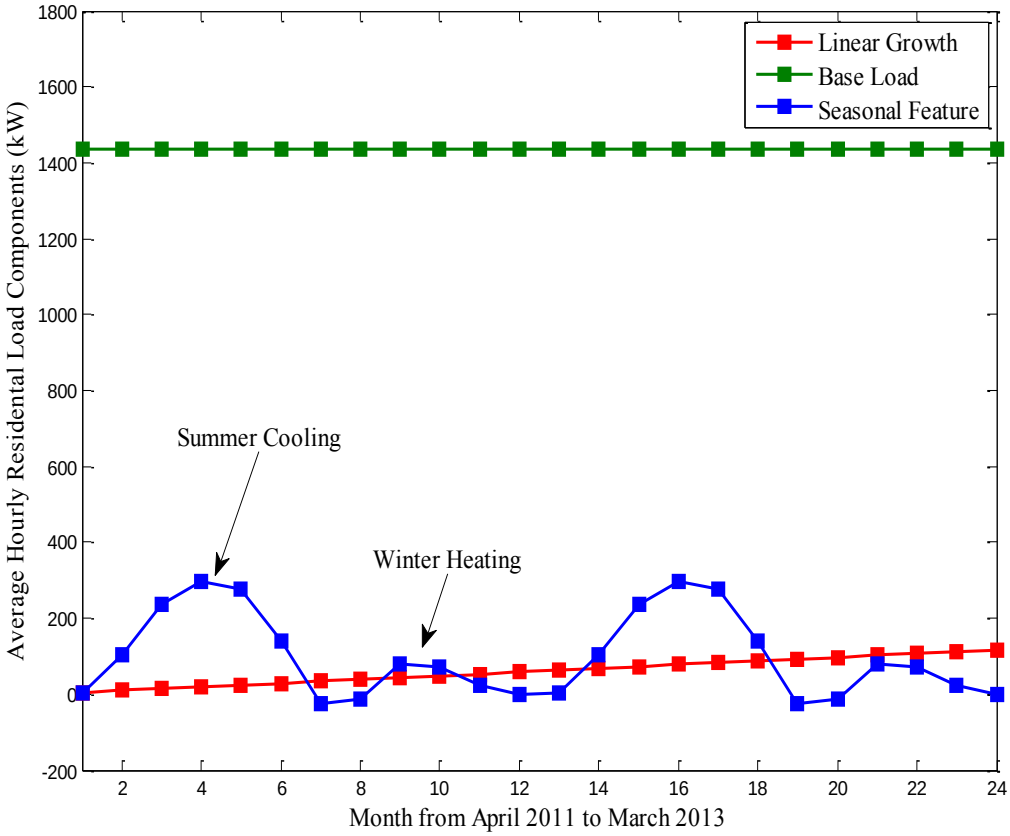

Figure 4. Residential loads decomposition.

The simulated average hourly load curve can be obtained by:

$$\hat{Y} = W \cdot X \tag{2.23}$$

Figure 5 depicts the comparison between the measured average hourly load curve and the simulated average hourly load curve. By expanding the index of the month, this model is also able to predict the average hourly residential load in future months.

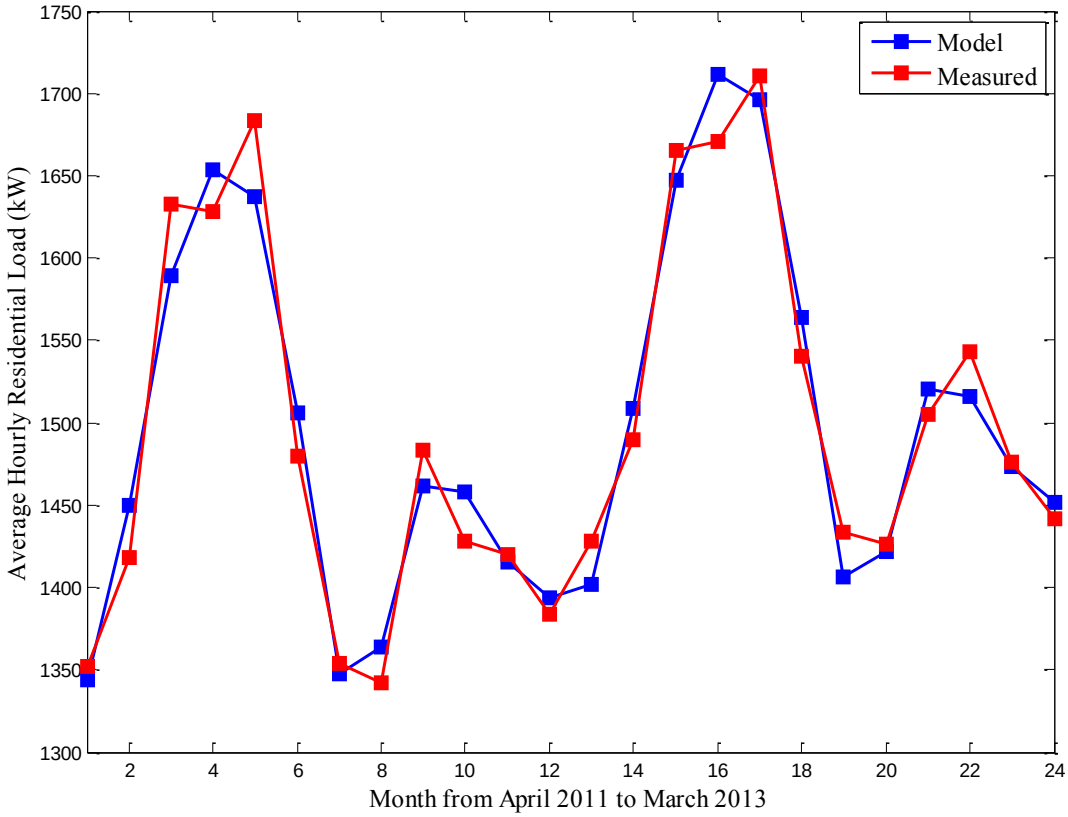

Figure 5. Average hourly residential load modeling.

2.6 Objective Function Setup

The objective of optimal sizing the distributed generators is to minimize the cost of installation, operation & management, subject to the different nature and demand profiles, within a certain time period.

Many previous studies are completed to generalize the objective function for optimal sizing the DGs. Some of these researches over simplified the residential power demands by treating the dynamic load as a constant one. Some others used the controllable distributed generators like micro gas-burn turbines to compensate the disadvantages of the renewable generators, which makes the problem more flexible but less challenged. Agalgaonkar, et al

presented an optimal sizing method to find the minimum cost of energy and optimal mix of dispatchable distributed energy resources with multiple sources and sinks over a year [16]. Wang, et al proposed a life time optimal renewable micro grid design, but its demonstration is based on short-term climate and load data set, which may accumulate the prediction errors if using in long-term simulation [17].

To secure the long-term micro-grid demand and low renewable DG costs, the optimization strategy should consider:

1. A long term planning project should be separated to several subjective short term projects for adjusting to the rapid changing of the cost of renewable DGs and the growth of load.
2. The energy production calculation should only be based on the actual power generation derived from the climate information rather than the rate information listed on the device name plates.
3. The power generated from the renewable generators should always meet the load demands, especially in the poor nature resource seasons, which ensure the power supplement.

A fully functional microgrid can operate in both grid-connected and grid-off modes. However, it is prior to consider the optimal sizing problem under autonomous (grid-off) operation mode due to the energy supplement reliability, even grid-connected operation mode requiring less investment. Also, the different financial options can generate different objective function. In this research, a general objective function of the cost minimization is considered as following:

$$Objective: Min\left(C_{ann}\right) = Min\left(C_{totoal}^{Installtion} + C_{ann}^{O\&M} - C_{ann}^{Salvage}\right) \tag{2.24}$$

subject to:

$$P_{DG_i \min} \le P_{DG_i} \le P_{DG_i \max} \tag{2.25}$$

$$\sum_{i=1}^{n} P_{DG_i,j} \ge P_{load,j} \qquad j = 1 \cdots 12 \tag{2.26}$$

where C_{ann} is the annual total cost of a DG combination; $C_{ann}^{installation}$, $C_{ann}^{O\&M}$, and $C_{ann}^{salvage}$ are the capital installation, O&M (operation and management) cost, and salvage value after a year, respectively; $P_{DG_i,j}$ is the power production of the i_{th} distributed generator in the j_{th} month, and $P_{load,j}$ is the load demanded in the j_{th} month.

If the average solar power and wind power output are known for particular solar panel and wind turbines, and the average residential load is known as well. The constraints of the objective function can be replaced by:

$$C_{total}^{Installtion} = a \cdot C_{WT}^{installtion} \cdot P_{WT}^{rated} + b \cdot C_{solar}^{installtion} \cdot P_{solar}^{rated} \tag{2.27}$$

$$C_{ann}^{O\&M} = a \cdot C_{WT}^{o\&m} \cdot P_{WT}^{rated} + b \cdot C_{solar}^{o\&m} \cdot P_{solar}^{rated} \tag{2.28}$$

$$C_{ann}^{Salvage} = a \cdot C_{WT}^{installtion} \cdot P_{WT}^{rated} \cdot \left(1 - D_{WT}\right) + b \cdot C_{solar}^{installtion} \cdot P_{solar}^{rated} \left(1 - D_{solar}\right) \tag{2.29}$$

$$a \cdot P_{WT_{avg,i}} + b \cdot P_{solar_{avg,i}} \ge P_{load,i} \qquad i = 1 \cdots 12 \tag{2.30}$$

$$a \in [0, \max\left(\frac{P_{load,i}}{P_{WT_{avg,i}}}\right) + 1] \qquad i = 1 \cdots 12 \tag{2.31}$$

$$b \in [0, \max\left(\frac{P_{load,i}}{P_{solar_{avg,i}}}\right) + 1] \qquad i = 1 \cdots 12 \tag{2.32}$$

where a and b are numbers of the wind and solar power conversion systems planned; $C_{WT}^{installation}$ and $C_{solar}^{installation}$ are the installation costs for the wind and solar power conversion systems in $\$/kW$; P_{WT}^{rated} and P_{solar}^{rated} are the rated powers of the wind and solar power conversion systems in

kW ; D_{WT} and D_{solar} are the monthly depreciation ratio of the wind and solar power conversion systems.

2.7 Non-uniform Simulated Annealing Algorithm

Simulated annealing (SA) is a local search algorithm (meta-heuristic) capable of escaping from local minimum by applying the hill-climbing strategy as shown in Figure 6. SA mimics the metaphor of the process of physical annealing with solids, in which a crystalline solid is heated and then allowed to cool very slowly until it achieves its most regular possible crystal lattice configuration (i.e., its minimum lattice energy state), and thus is free of crystal defects.

If the cooling schedule is sufficiently slow, the final configuration results in a solid with such superior structural integrity. Simulated annealing establishes the connection between this type of thermodynamic behavior and the search for global minima for a discrete optimization problem. Furthermore, it provides an algorithmic means for exploiting such a connection.

Theoretically, the convergence of simulated annealing for finding the globe minimum was proven based on both homogeneous and inhomogeneous Markov chain theories in [18-25]. The proofs using homogeneous Markov chain requires that each temperature t_k is held constant for a sufficient number of iterations m such that a non-negative square stochastic matrix, defined by the transition probabilities of generating a candidate solution ω' from the neighbors of solution $\omega \in \Omega$ can reach its stationary distribution. The proofs using inhomogeneous Markov chain need not to reach a stationary distribution, but an infinite sequence of iterations k must still be examined with the condition that the temperature parameter t_k cool sufficiently slowly. In a word, the theoretical convergence proofs of simulated annealing require a very large number of new solutions to examine whether the state of energy is frozen or not, and it is very difficult or impossible in practice.

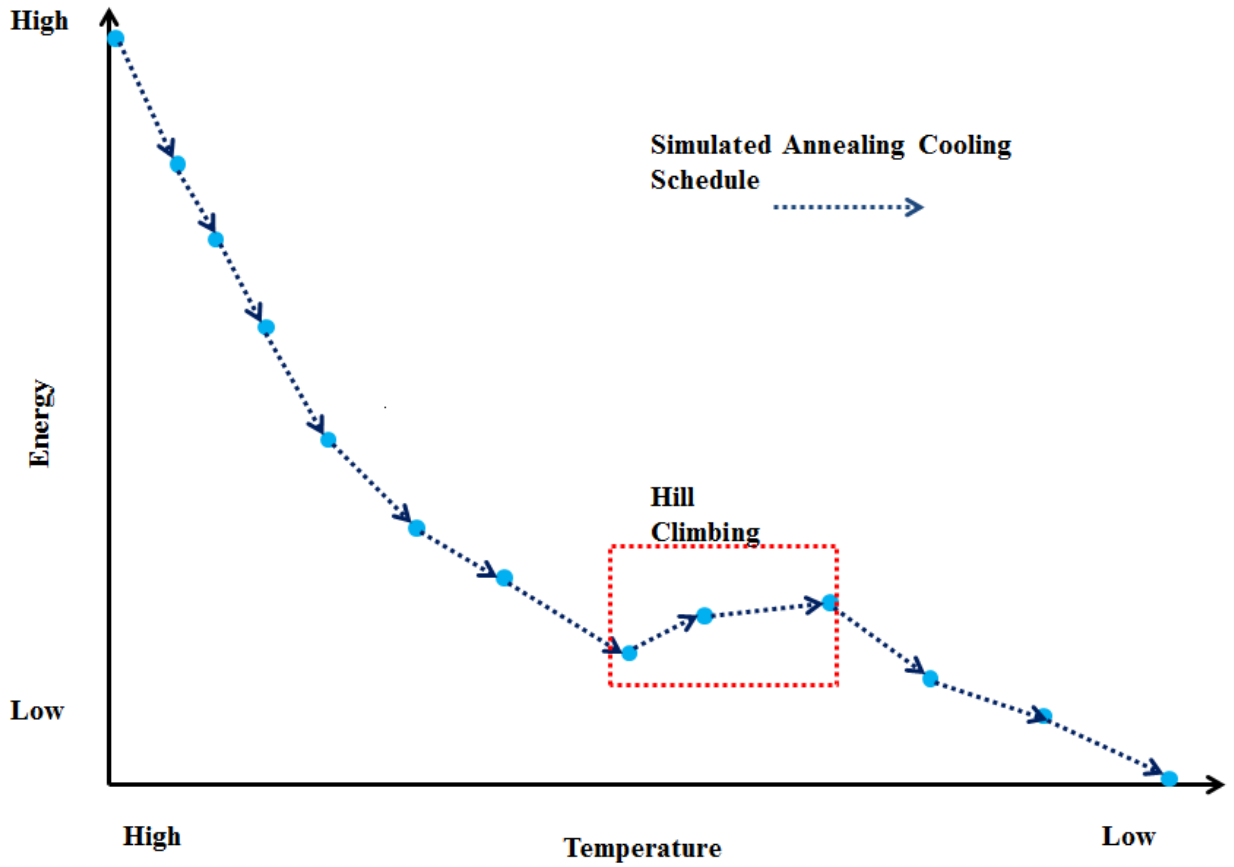

Figure 6. Simulated annealing cooling procedure and its hill climbing feature.

In practical, the challenges of applying simulated annealing for optimization problems can be divided into two problem-specific aspects.

1. Choice of a new solution generator.
2. Choice of cooling schedule.

The efficiency of simulated annealing is highly influenced by the neighborhood function used. However, the neighborhood structure is decided by the nature of the problem, which is not easy to be captured in most cases. In general, a uniformed mutation function is applied to generated new solutions as follow:

$$\omega' = round\left(U\left(\omega_{\max} - \omega_{\min}\right) + \omega_{\min}\right) \tag{2.33}$$

where ω' is a new solution, $\omega' \in \Omega$, $U(x)$ is a uniformed random number generator, $U(x)$ ranges from [0, 1], and $\omega_{\min}$, and $\omega_{\max}$ are the lower limit and upper limit of the ω based on the hard constraints of the objective function, respectively. If this uniformed mutation function is executed with enough times, all the possible solutions will be explored, which is similar to the greedy algorithm. Hence, the genetic mutation function has to be modified to enhance the efficiency of searching the optimal solution in the space. Ideally, a desired mutation function is capable of searching the space uniformly at early stages and locally at later stages. For this reason, Michalewicz proposed a dynamical non-uniform mutation operator to reduce the disadvantage of random mutation in evolution algorithm, and it is also valid for the simulated annealing [26-28].

For each individual Ω_i^t in a population of the t_{th} generation, create an offspring Ω_i^{t+1} through a non-uniform mutation as follows: if $\Omega_i^t = \{\omega_1, \cdots \omega_k, \cdots, \omega_m\}$ is a chromosome (t is the generation number) and the element ω_k is selected for this mutation, the result is a vector $\Omega_i^{t+1} = \{\omega_1, \cdots \omega_k', \cdots, \omega_m\}$, where

$$\omega_{n+1} = \begin{cases} \omega_n + \Delta(n, \omega_{\max} - \omega_n) & if \quad \eta = 1 \\ \omega_n - \Delta(n, \omega_n - \omega_{\min}) & if \quad \eta = -1 \end{cases} \tag{2.34}$$

where η is a random number, which has the equal probability of $\eta = 1$ or $\eta = -1$; n is the number of the current epoch.

The function $\Delta(n, y)$ returns a value in the range $[0, y]$ such that $\Delta(n, y)$ approaches to zero as n increases. This property allows this operator to search the space uniformly at early stages (when n is small), and locally at later stages. The definition of $\Delta(n, y)$ is as follow:

$$\Delta(n, y) = y \cdot \left(1 - r^{\left(1-\frac{n}{N}\right)^b}\right) \tag{2.35}$$

where r is a uniform random number between $[0,1]$, N is the maximal generation number, n is the current generation number, and b is a system parameter determining the degree of non-uniformity.

The distance D between the old solution x and new solution x' in a neighborhood N will be:

$$\begin{aligned} D &= \|x - x'\| \\ &= \frac{1+r}{2}(x_{\max} - x)\left(1 - r^{\left(1-\frac{n}{N}\right)^b}\right) + \frac{1-r}{2}(x - x_{\min})\left(1 - r^{\left(1-\frac{n}{N}\right)^b}\right) \end{aligned} \tag{2.36}$$

The expectation of the random radius of two adjacent neighborhoods is:

$$\begin{aligned} E(D) &= P(\eta = 1)(x_{\max} - x)E\left(1 - r^{\left(1-\frac{n}{N}\right)^b}\right) + P(\eta = -1)(x - x_{\min})E\left(1 - r^{\left(1-\frac{n}{N}\right)^b}\right) \\ &= \frac{x_{\max} - x_{\min}}{2} E\left(1 - r^{\left(1-\frac{n}{N}\right)^b}\right) = \frac{x_{\max} - x_{\min}}{2} \int_0^1 \left(1 - r^{\left(1-\frac{n}{N}\right)^b}\right) dr \\ &= \frac{x_{\max} - x_{\min}}{2}\left(1 - \frac{1}{1 + (1 - (n/N))^b}\right) \end{aligned} \tag{2.37}$$

when $n = 0$, $E(D) \to \frac{x_{\max} - x_{\min}}{4}$, when $n = N$, $E(D) \to 0$. Neither likes the Gaussian mutation which only locally searches nor Cauchy mutation which makes large step size in the whole search process [29, 30]. Let $f(n) = E(D)$, which is a differentiable function, then we have that $f(n)$ is a decreasing function of n (supposing n being a continuous variable though it is a discrete one), because

$$\frac{df(n)}{dn} = \frac{x_{\max} - x_{\min}}{2} \cdot \frac{d\left(1-\left(1/\left(1+\left(1-\frac{n}{N}\right)^{b}\right)\right)\right)}{dn} = -\left(\frac{x_{\max} - x_{\min}}{2} \cdot \frac{(b/N)\left(1-(n/N)\right)^{b-1}}{\left(1+\left(1-(n/N)^{b}\right)\right)^{2}}\right) < 0 \tag{2.38}$$

Equation 2.38 provides the main property of non-uniform mutation operator. That is, the expectation of the random radius of neighborhood monotonously decreases with the progress of the algorithm in the sense of probability. Furthermore, this dynamic operator has the features of searching the space uniformly at early stages (when n is small), and locally at later stages.

Once the choice of a new solution generator is made, the next step is to choose the proper cooling schedule. The simulated annealing cooling schedule is fully defined by an initial temperature, a schedule for reducing/changing the temperature, and a stopping criterion. Romeo and Sangiovanni-Vincentelli noted that an effective cooling schedule is essential to reducing the amount of time required for finding an optimal solution [31]. Therefore, much of the literature on cooling schedules is devoted to this topic theoretically. However, as same as the choice of a new solution generator, it is also very difficult to apply those theoretical cooling schedule in practice. A common used cooling schedule is defined as follow:

$$t_{n+1} = \alpha \cdot t_n \tag{2.39}$$

Where α is a decreasing coefficient, $0.9 \le \alpha < 1$. The temperature is decreasing, while the iteration number is increasing. In theory, the initial temperature should be high enough to excite the inner particles. However, in practice, if the initial temperature over heats the inner particles, the annealing process will be trapped in iterative uphill and downhill movements. In this paper, the initial temperature will define by experience obtained in the experiments.

Based on the explanation above, the non-uniform simulated annealing algorithm is concluded as follows:

1. Set the initial temperature to t_0, maximum iteration number N, the temperature decreasing coefficient α and the initial iteration index $n=0$.
2. Generate the initial neighborhood of k solutions $\omega_1^n \cdots \omega_k^n$, $\omega_i^n \in \Omega$, $i=1\cdots k$, each of which has m independent components, $\omega_i^n = \left[x_{i,1}^n, x_{i,2}^n, x_{i,3}^n, \cdots, x_{i,m}^n \right]$. Evaluate the initial solutions based on the energy function, $E\left(\omega_i^n\right)$.
3. Choose the best solution ω_b^n as the current state ω_c, $n=n+1$.
4. For each parental individual, $\omega_i^n = \left[x_{i,1}^n, x_{i,2}^n, x_{i,3}^n, \cdots, x_{i,m}^n \right]$, randomly generate a m-length decimal sequence $\left[r_1, r_2, \cdots, r_m \right]$. For each component of ω_i^n, $x_{i,j}{}^n$, $i=1\cdots k$, $j=1\cdots m$, construct $x_{i,j}^n{}'$ using the Equation 2.34 and new individual is denoted by $\omega_i^n{}'$. Evaluate the solutions based on the energy function, $E\left(\omega_i^n{}'\right)$.
5. Choose the best solution $\omega_b^{n'}$ as the alternative state ω_a.
6. If $E\left(\omega_a\right) \le E\left(\omega_c\right)$, $\omega_a \to \omega_c$, $t=\alpha \cdot t$.
7. If $f\left(\omega_a\right) > f\left(\omega_c\right)$ with a probability $\exp\left(-\left(E\left(\omega_c\right)-E\left(\omega_a\right)\right)/\left(k \cdot t\right)\right) < r$, then $\omega_a \to \omega_c$, $t=\alpha \cdot t$ where r is a randomly generated decimal; k is Boltzmann constant; t is the current temperature.
8. Repeat steps from 3 to 7, until the stopping criteria until current epoch number n is equal to the maximum epoch number N.

Figure 7 displayed the charts flow of the non-uniform simulated annealing optimization procedure.

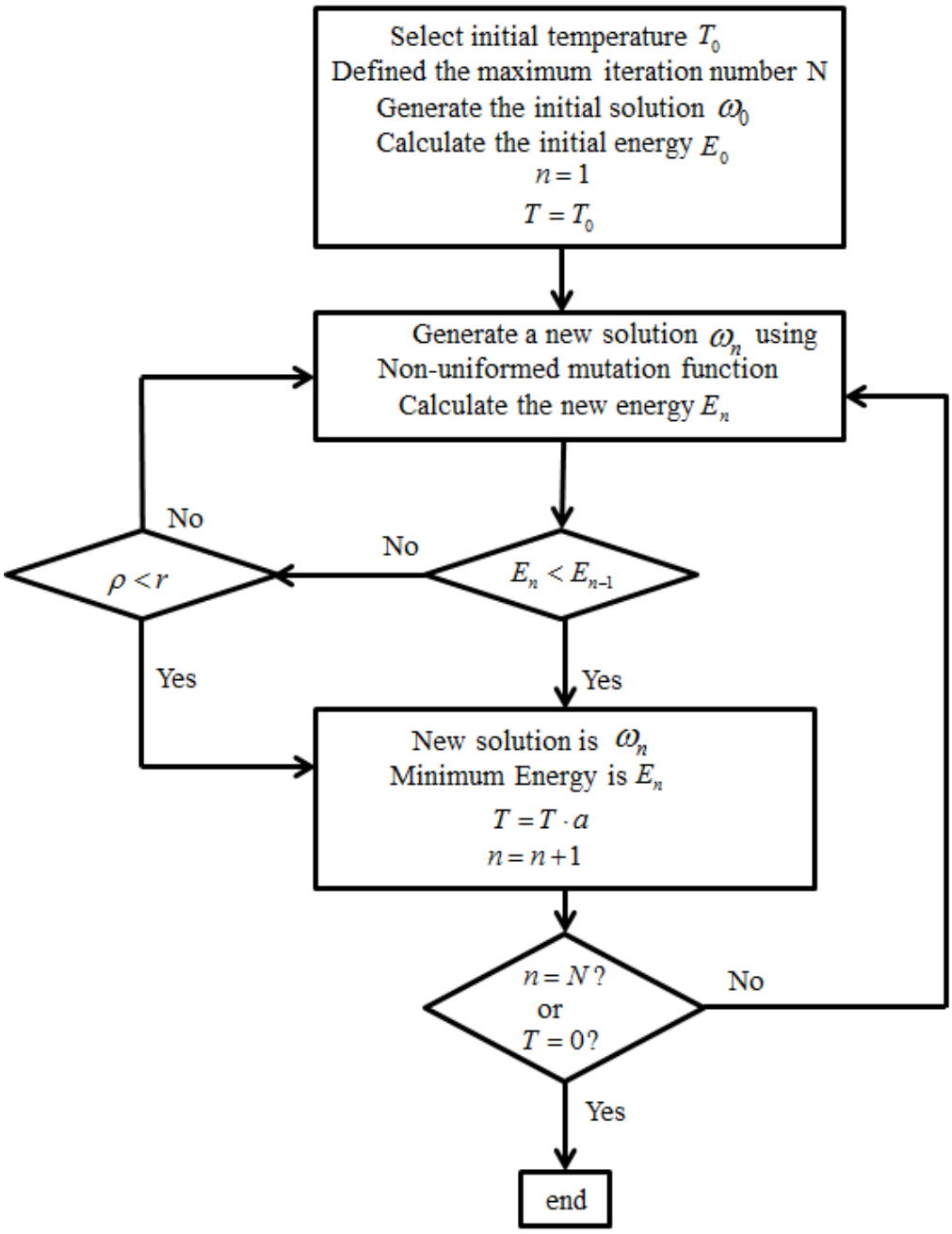

Figure 7. Non-uniform simulated annealing optimization procedure.

In the condition block $\rho < r$ there is a bi-directional signal flow. This block determines the non-uniform simulated annealing is capable of avoiding the local minimum, when it is

searching the global optimum solution. Different selections of initial temperature, maximum iteration number, or degree of non-uniformity of the mutation function will yield to different performances of the non-uniform simulated annealing.

CHAPTER 3

Dynamic Modeling of Residential Microgrid

3.1 Introduction

In the last chapter, the optimal sizing of renewable distributed generators is discussed based on the long-term probability models of variant types of nature recourses, including wind speed, global solar radiation, and cell temperature. The generation capacities of different DGs at a given location over a specified period are available. In this section, the dynamic models and their control systems will be presented.

3.2 Photovoltaic (PV) Modeling

The PV system produces power without harming the environment by transferring a free inexhaustible source of energy, solar irradiation, to the electricity. This factor associated with continuously decrement of the cell cost and increment of the conversion efficiency promises a good future of PV generation.

3.2.1 Mathematical model of PV arrays The fundamental unit of a PV array is the solar cell, which is basically a P-N semiconductor junction that directly converts the light energy into electricity [32]. Figure 8 displayed the equivalent circuit. The current source I_{pv} represents the cell photocurrent inspired by the global solar radiation and constrained by the cell temperature. The diode is used to mimic the non-linear performance of the P-N junction, and the Shockley diode current I_d varies with the terminal voltage V. Based on the Kirchhoff current law, the terminal current output I can be calculated. Because the Shockley diode current I_d is constrained by the terminal voltage V, terminal current I is also constrained by the terminal

voltage V . As a result, this fact introduces the maximum power tracking problem, which will be covered in the next section.

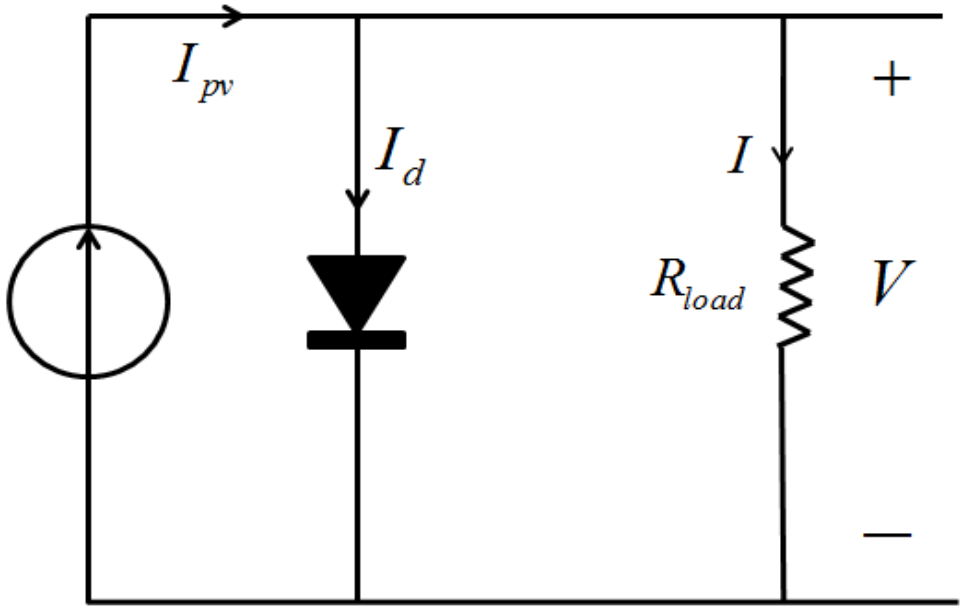

Figure 8. Equivalent Circuit Diagram of a PV Cell.

The cell photocurrent I_{pv} is governed as:

$$I_{pv} = \left[I_s + k_i \left(T_c - T_{c,ref} \right) \right] \frac{G}{G_{ref}} \tag{3.1}$$

where I_s is the short-circuit current at cell reference temperature $T_{c,ref}$ $\left(300k\right)$; G_{ref} is the reference radiation $\left(1000w/m^2\right)$; k_i is the short circuit current temperature coefficient, which is decided by different types of cell materials; T_c and G are the arbitrary cell temperature and radiation. T_c is calculated by the equation as follow:

$$T_c = T_a + \left(NOCT - 20°C \right) \left(\frac{S}{800} \right) \tag{3.2}$$

This method yields satisfying results if the PV modules are not roof integrated. NOCT is calculated for a wind speed $v = 1ms^{-1}$, an ambient temperature $T_a = 20°C$ and irradiance $S = 800W/m^2$ [33, 34].

The Shockley diode current I_d is defined as:

$$I_d = I_{rs}\left[\exp\left(\frac{qV}{kT_cA}\right)-1\right] \tag{3.3}$$

where q is the charge of an electron; k is the Boltzmann's constant; A is the P-N junction ideality factor, which determines the cell deviation from the ideal P-N junction characteristics, normally $1 \le A \le 1.6$. The cell reverse saturation current I_{rs} varies with the cell temperature respect to the following [35-39]:

$$I_{rs} = I_{rr}\left[\frac{T_c}{T_{c,ref}}\right]^3 \exp\left(\frac{qE_G}{kA}\left[\frac{1}{T_{c,ref}}-\frac{1}{T_c}\right]\right) \tag{3.4}$$

where E_G is the band-gap energy of the semiconductor used in the cell ($E_G = 1.12eV$ for the polycrystalline Si at 20^oC [36]); I_{rr} is the reverse saturation current at cell reference cell temperature calculated as:

$$I_{rr} = \frac{I_{sc,ref}}{\exp\left(V_{oc,ref}/AV_{t,n}\right)-1} \tag{3.5}$$

By using the Kirchhoff current law, the current output I will be obtained by:

$$I = I_{pv} - I_{rs}\left[\exp\left(\frac{qV}{kT_cA}\right)-1\right] \tag{3.6}$$

As a result, the output power can be calculated as:

$$P = I \cdot V \tag{3.7}$$

Figure 9 plots the I-V curve, which is modeling a practical PV array, KC200GT Solar Array, under the standard test condition. The terminal voltage is increasing from 0V to the open circuit voltage. The terminal current is decreasing from the short circuit current to 0A.

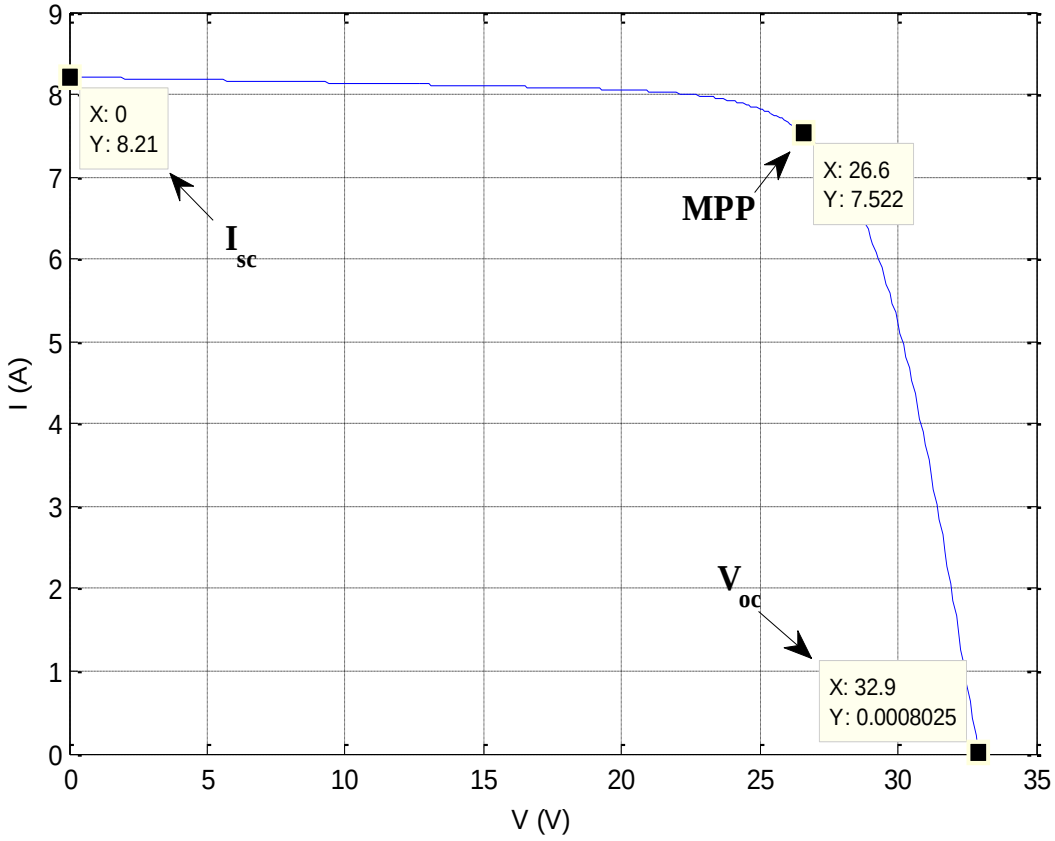

Figure 9. I–V curve of the KC200GT solar array in the standard test condition.

Figure 10 plots the P-V curve in the standard test condition. When the terminal voltage is increasing from 0V to the open circuit voltage, the power output is increasing at early stages rapidly. After the power curve passes the maximum power point, it will begin to decrease at later stages. This feature introduces the maximum power point tracking of the solar panels, which allows it produce the maximum power by varying the terminal voltage.

Figure 11 plots the P-V curves under different solar irradiances and temperatures, the blue curves represented at $25^{o}C$; the red curves represented at $50^{o}C$; the black curves

represented at $75^{o}C$. The lower cell temperature yields to the higher power output. The solar array parameters of KC200T are shown in Appendix.

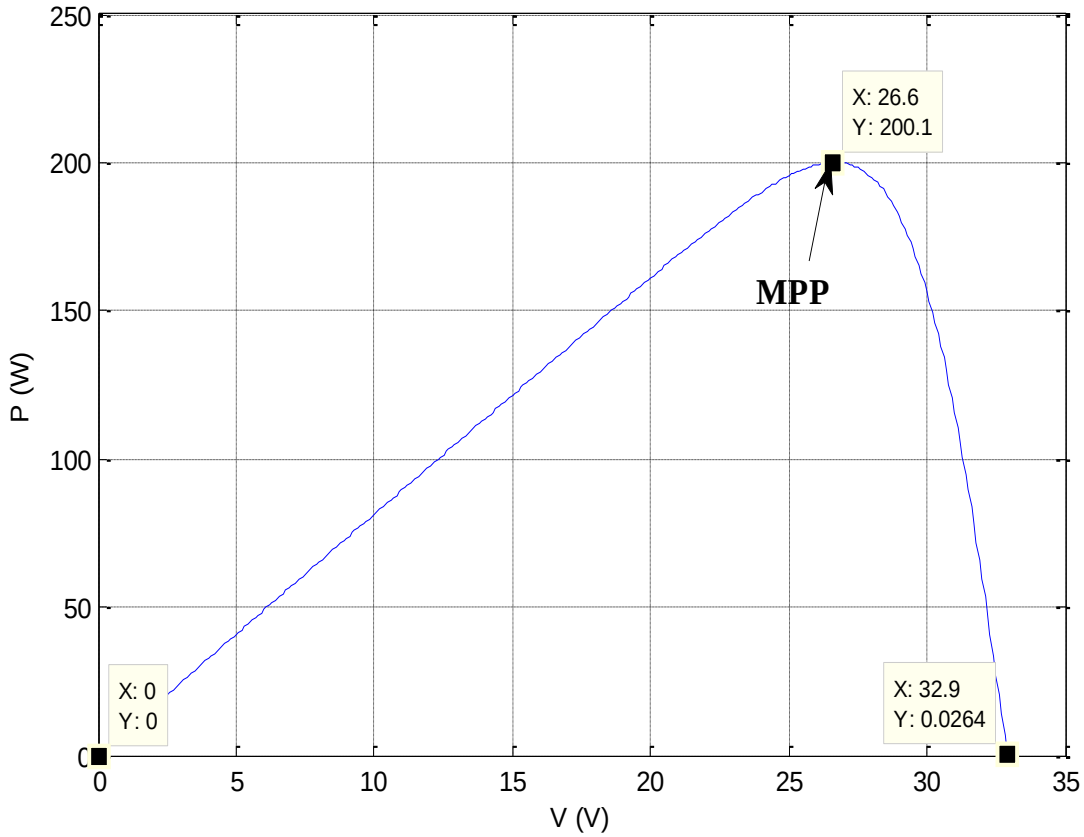

Figure 10. P-V curve of the KC200GT solar array under standard test condition.

3.2.2 Optimal power point tracking As shown in Figure 12, the power generated by the PV arrays at any pair of global radiation and cell temperature varies based on different terminal voltage applied. For tracking the maximum power output, a variable DC voltage generator is required to be mounted at the terminal end of the PV array. The voltage level should be adjusted to meet the optimal voltage which generates the maximum power output. The optimal terminal voltage V_m is determined as:

when

$$\frac{dP}{dV_i} = 0 \tag{3.8}$$

then

$$V_m = V_i \tag{3.9}$$

where V_i is the terminal voltage, which ranges from 0 to V_{oc}.

As a conclusion of previous modeling steps, the equivalent circuit diagram of a PV array shown in Figure 8 has been further developed and displayed in Figure 12. The radiation inspired current I_{pv}, the terminal voltage dependent current I_{rs}, and the optimal terminal voltage V_m are the inputs of the diagram, and the output is the maximum power output $P_{\max}$.

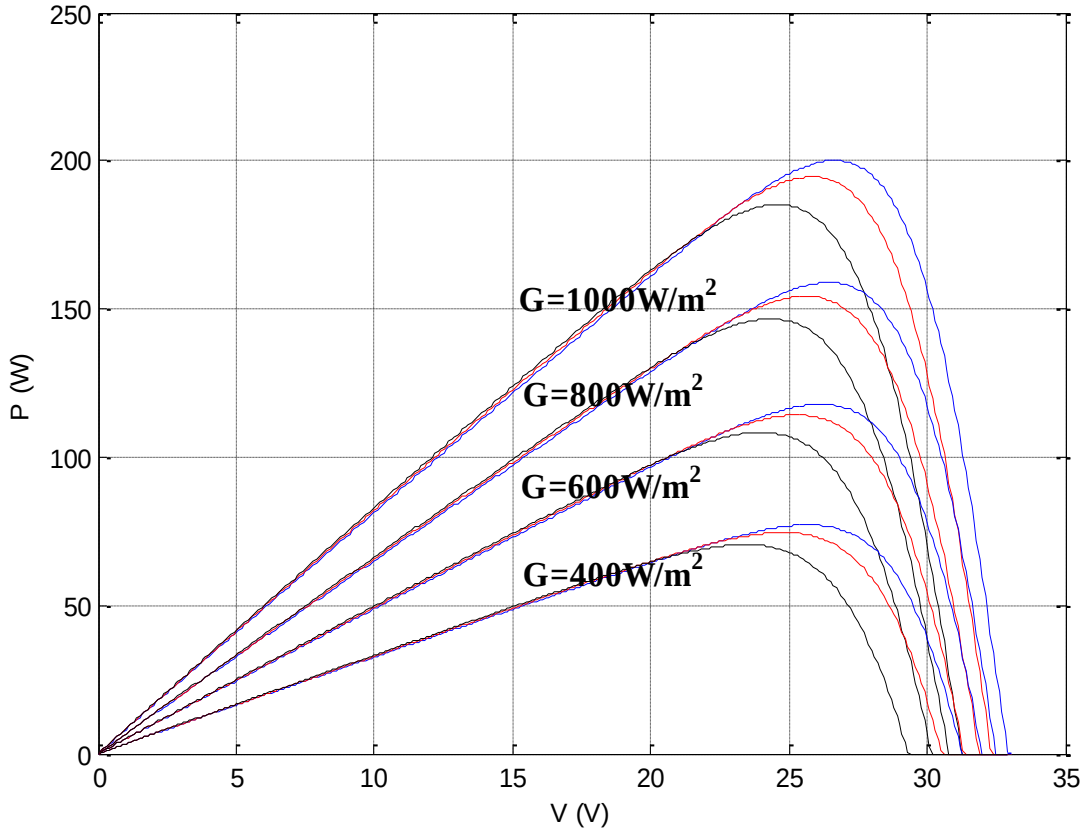

Figure 11. P-V curves of the KC200GT solar array under different test conditions.

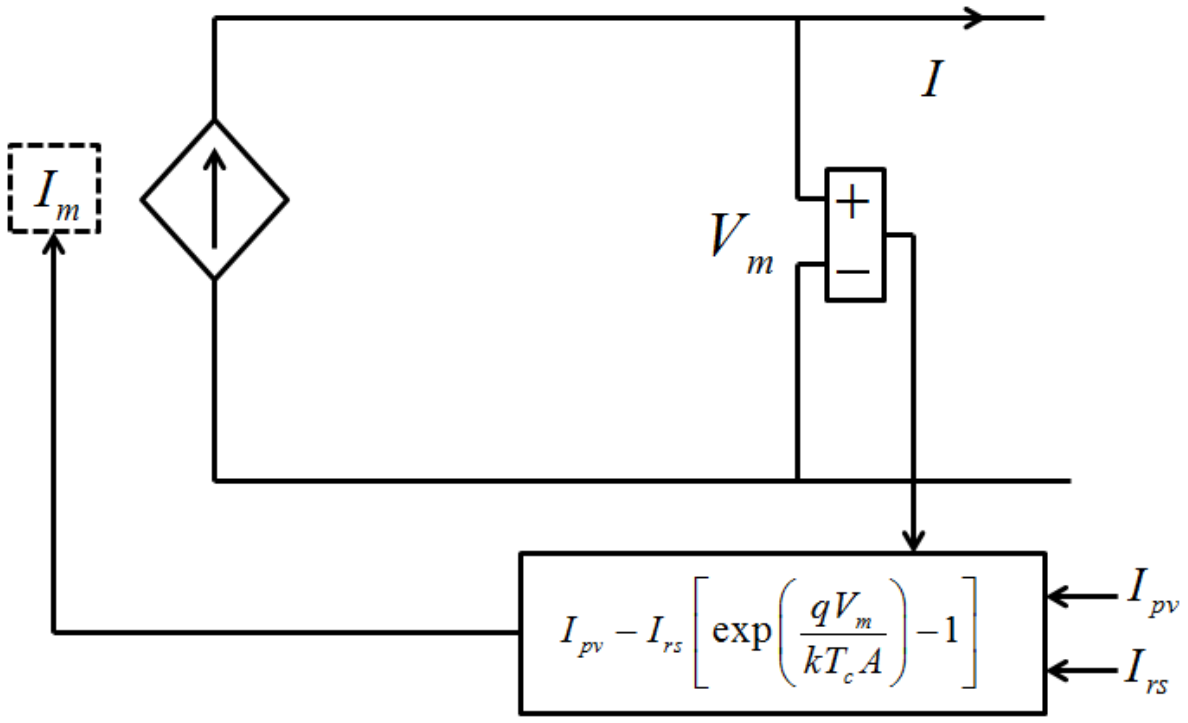

Figure 12. Equivalent circuit diagram of a PV Cell with a controlled current source, equivalent resistors, and the equation of the model current I_m.

3.2.3 Power electronic interface of the PV As concluded in the last section, the terminal voltage of the PV circuit varies to generate the maximum power output. In order to maintain a constant terminal DC voltage, an inductive DC/DC boost converter is required. Another DC/AC three phase inverter is also required for inverting the DC power to three phase power.

3.2.3.1 Inductive DC/DC boost converter The equivalent circuit of a general inductive DC/DC boost converter is shown in Figure 13(a). For maintaining the continuous conduction mode (CCM), the current through the inductor $i_L(t)$ has a finite, positive value, which is not zero and the operation mode consists two phases [40]:

1. The inductor charging phase: The equivalent circuit for this phase is shown in Figure 13(b), which is achieved by closing switch 1 and opening switch 2 for a certain period t_{on}.

During this phase, the inductor L is charge by the voltage source U_{in}, causing the inductor current $i_L(t)$ to increase from its minimum value $i_{L,\min}$ to its maximum value $i_{L,\max}$. At the same time, the capacitor C is discharged through the load resistor R_L.

2. The inductor discharging phase: The equivalent circuit for this phase is shown in Figure 13(c), which is achieved by closing switch 2 and opening switch 1 for a certain period t_{off}. During this phase, the inductor L is discharged into the capacitor C and the load resistor R_L, causing the inductor current $i_L(t)$ to decrease from its maximum value $i_{L,\max}$ to its minimum value $i_{L,\min}$. As a result, $i_L(t)$ is divided over C and R_L, thereby charging C and supplying the power to R_L.

From Figure 13(b) and (c), Equation 3.10 can be concluded that the voltage over the inductor L in an operating cycle.

$$\begin{cases} 0 \to t_{on}, & u_L(t) = U_{in} \\ t_{on} \to t_{off}, & u_L(t) = U_{in} - U_{out} \end{cases} \tag{3.10}$$

In steady-state operation, the net energy change in the inductor per cycle is zero, thus the volt-second balance of the inductor is also zero. This yields Equation 3.11:

$$\int_0^t u_L(t)dt = U_{in}t_{on} + (U_{in} - U_{out})t_{off} = 0 \tag{3.12}$$

Equation 3.11 can be rewritten as:

$$\frac{U_{out}}{U_{in}} = \frac{t_{on} + t_{off}}{t_{off}} = \frac{1}{1-\delta} \tag{3.12}$$

where δ is called the duty cycle, and defined as:

$$\delta = \frac{t_{on}}{t_{on} + t_{off}} = \frac{t_{on}}{T} \tag{3.13}$$

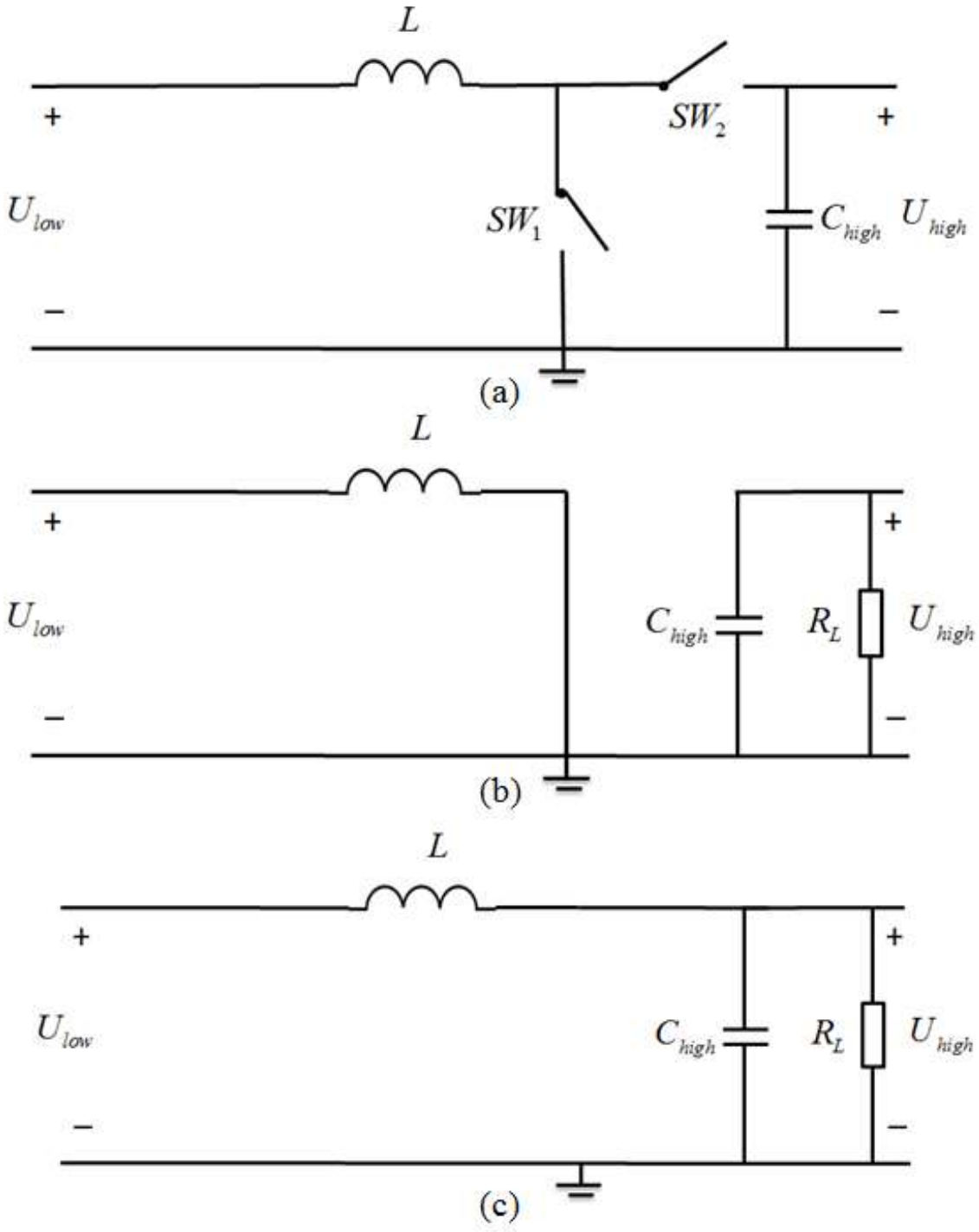

Figure 13. (a) Circuit of an inductive DC/DC boost converter, (b) equivalent circuit of the inductor charging phase, and (c) the inductor discharging phase.

When the converter is working in the inductor charging phase, the current though the inductor at $\delta \cdot T$ is calculated as:

$$\begin{aligned} I_L(\delta \cdot T) - I_L(t_0) &= \frac{1}{L}\int_0^{\delta \cdot T} u_L(t)\,dt \\ &= \frac{1}{L} U_{in} \cdot \delta \cdot T \end{aligned} \tag{3.14}$$

$$I_L(\delta \cdot T) = \frac{1}{L} U_{in} \cdot \delta \cdot T + I_L(t_0) \tag{3.15}$$

The current though the capacitor at $\delta \cdot T$ is calculated as:

$$I_C(\delta \cdot T) = -\frac{U_{out}}{R_L} = -\frac{P}{U_{out}} \tag{3.16}$$

When the converter is working in the inductor discharging phase, the current though the inductor at T is calculated as:

$$\begin{aligned} I_L(T) - I_L(\delta \cdot T) &= \frac{1}{L}\int_{\delta \cdot T}^{T} u_L(t)\,dt \\ &= \frac{1}{L}(U_{out} - U_{in}) \cdot (T - \delta \cdot T) \end{aligned} \tag{3.17}$$

$$I_L(T) = \frac{1}{L}(U_{out} - U_{in}) \cdot (T - \delta \cdot T) + I_L(\delta \cdot T) \tag{3.18}$$

The current though the capacitor at T is calculated as:

$$I_C(T) = I_L(T) - \frac{U_{out}}{R_L} = I_L(T) - \frac{P}{U_{out}} \tag{3.19}$$

During the phase one, the output voltage is decreasing because the capacity is discharging. During the phase two, the output voltage is increasing because the capacity is charging.

In the phase one, the discharge current $i_C(t)$ of C can be approximated to have a constant value as:

$$i_C(t) = C\frac{dU_{out}(t)}{dt} = -\frac{\bar{U}_{out}}{R_L} = -\frac{P}{\bar{U}_{out}} \tag{3.20}$$

Thus, the net change of $U_{out}(t)$ can be calculated by:

$$\Delta U_{out} = -\frac{1}{C}\int_0^{\delta T} i_C(t)dt = \frac{P}{\bar{U}_{out}C}\delta T \tag{3.21}$$

3.2.3.2 Pulse width modulation (PWM) based three phase DC/AC inverter The three phases DC/AC converting is achieved by the PWM inspired three phase DC/AC full-wave bridge converter as shown in Figure 14 [41].

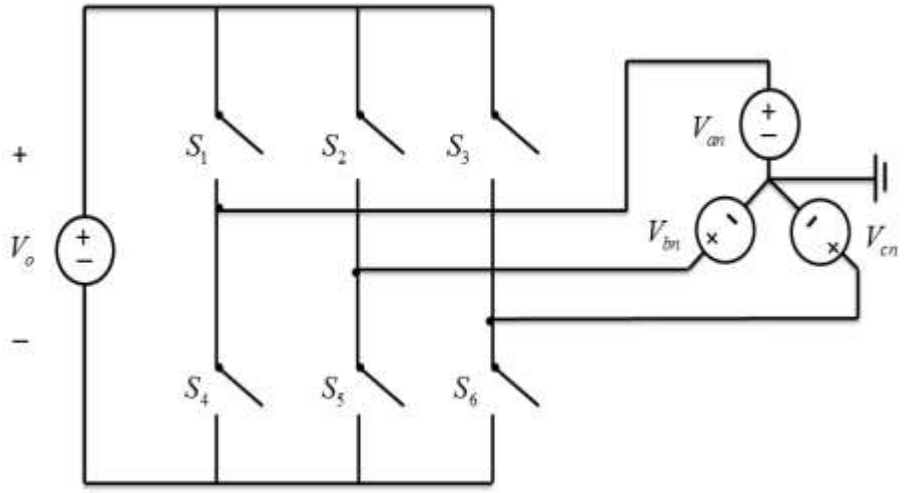

Figure 14. Three phase full bridge DC/AC inverter.

The switching mechanism is controlled by the PWM technology. The three phase full bridge inverter requires three reference signals, V_a, V_b, V_c and one carrier signal, $V_{carrier}$, which is commonly using the triangular signal synchronized with the grid voltage vector. The frequency modulation ratio mf is defined as the ratio of the frequencies of the carrier and reference signals:

$$mf = \frac{f_{carrier}}{f_{reference}} = \frac{f_{tri}}{f_{\sin}} \tag{3.22}$$

The amplitude modulation ratio ma is defined as the ratio of the amplitude of the carrier and reference signals:

$$ma = \frac{V_{m,reference}}{V_{m,carrier}} = \frac{V_{m,\sin}}{V_{m,tri}} \tag{3.23}$$

According to Figure 14, it states the nature of the two switches in the same leg is complementary and the detailed switching schedule is as follows:

S_1 is on when $V_a > V_{tri}$.

S_2 is on when $V_b > V_{tri}$.

S_3 is on when $V_c > V_{tri}$.

S_4 is on when $V_a < V_{tri}$.

S_5 is on when $V_b < V_{tri}$.

S_6 is on when $V_c < V_{tri}$.

An experimental demonstration is performed. The carrier signal is synchronized with the grid voltage vector with $mf = 10$. The reference signals are mimic the phase to ground voltages, which are 120^o apart with the amplitude $400/\sqrt{3}$ V. Figure 15 shows the reference and carrier signals of a full-bridge converter for the unipolar PWM. Figure 16 displayed the reference Phase A to Phase B voltage curve and the PWM based three phase DC/AC inverter output voltage waveform. The voltage waveform generated by the PWM based three phase DC/AC inverter is in square wave form. If only count the fundamental of the square waveform, the output wave form can be looked as the pure sin curve. However, in some circuits, the terminal reactance is not large enough to filter the high order harmonics. As a result, the total harmonic distortion (THD) is large enough to damage the end user appliance.

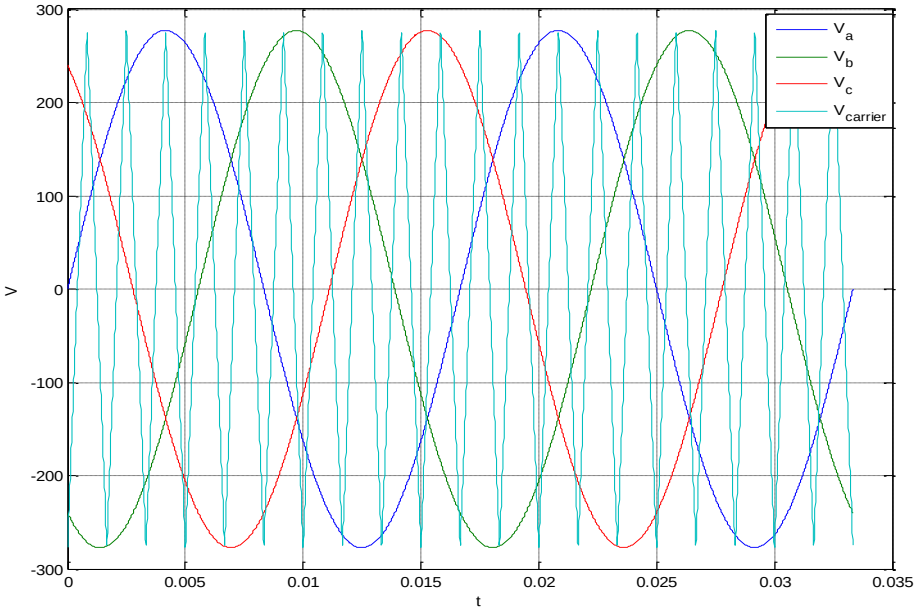

Figure 15. Reference and carrier signals for a unipolar PWM generator.

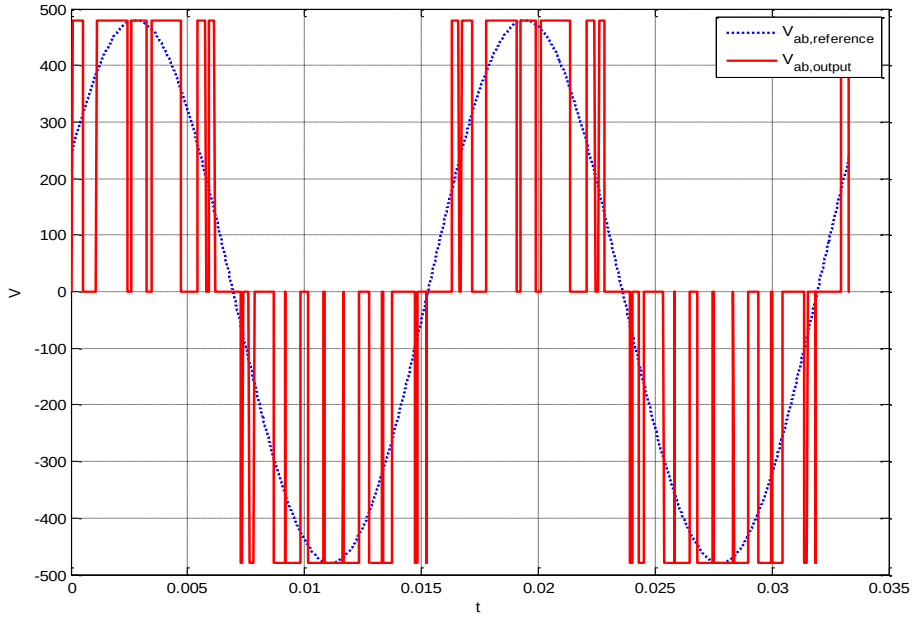

Figure 16. Phase A to phase B reference voltage curve and inverter output waveform.

3.3 Wind Power Conversion System Modeling

3.3.1 Fundamentals of wind energy extraction The wind energy conversion system is a multi-type energy transformation mechanism, and it transforms the air kinetic energy presented in the blowing wind to electrical energy with two phase stages. The kinetic energy in a parcel of air mass m flowing at speed v_w in the horizontal direction is:

$$E_{air} = \frac{1}{2} m v_w^{\,2} = \frac{1}{2} (\rho A x) v_w^{\,2} \tag{3.24}$$

where, E_{air} is the kinetic energy in joule, A is the cross-sectional area in m^2, ρ is the air density in kg/m^3, and x is the thickness of the parcel in m. If time derivative is taken at both side of Equation 3.24 on both side, then the wind kinetic power P_w can be obtained.

$$P_w = \frac{dE_{air}}{dt} = \frac{1}{2} \rho A v_w^{\,2} \frac{dx}{dt} = \frac{1}{2} \rho A v_w^{\,3} \tag{3.25}$$

Ideally, the power absorbed by the wind turbine is the wind energy difference between before and after the wind passes the turbine blades. It can be shown that under the optimal condition, the following relationships exist, when the maximum wind power is absorbed by the wind turbine [42].

$$u_2 = u_3 = \frac{2}{3} u_1 \tag{3.26}$$

$$u_4 = \frac{1}{3} u_1 \tag{3.27}$$

$$A_2 = A_3 = \frac{3}{2} A_1 \tag{3.28}$$

$$A_4 = 3A_1 \tag{3.29}$$

where u_1, u_2, u_3, and u_4 are the wind speeds corresponding to four positions listed in Figure 17; A_1, A_2, A_3, and A_4 are the cross-section areas corresponding to four positions, which are yielded from the pressures, p_1, p_2, and p_3.

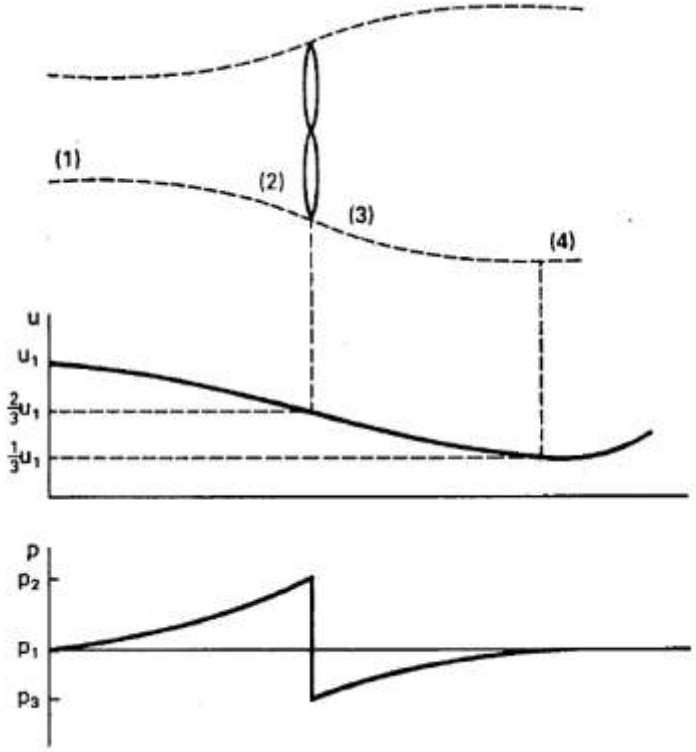

Figure 17. Circular tube of air flowing through an ideal wind turbine [42].

The mechanical power extracted from the wind under ideal condition is given as:

$$P_{m,ideal} = P_1 - P_4 = \frac{1}{2}\rho\left(A_1 u_1^{\,3} - A_4 u_4^{\,3}\right) = \frac{1}{2}\rho\left(\frac{8}{9}A_1 u_1^3\right) \tag{3.30}$$

Equation 3.30 can be rewritten in terms of the undistributed wind speed u_1 and the turbine blades swapping area A_2 as Equation 3.31.

$$P_{m,ideal} = \frac{1}{2}\rho\left(\frac{8}{9}\left(\frac{2}{3}A_2\right)u_1^3\right) = \frac{1}{2}\rho\left(\frac{16}{27}A_2 u_1^3\right) \tag{3.31}$$

It can be concluded that the maximum fraction of mechanical power extracted from the wind energy is 59.3%. In practice, this coefficient will be lower, because of mechanical imperfections, and it is replaced by a non-constant fraction C_p standing for the coefficient of performance, which varies with the tip speed ratio λ and blade pitch angle β. The tip speed ratio is defined as:

$$\lambda = \frac{\omega_R R}{v_w} \tag{3.32}$$

where R is the radius of blade; v_w is the wind speed in m/s; ω_R is the angular speed of turbine blades in rad/s.

If consider the affection of changing of the blade pitch angle β, the tip speed ratio λ is modified as [43]:

$$\lambda' = \frac{1}{\frac{1}{\lambda + 0.02\beta} - \frac{0.03}{\beta^3 + 1}} \tag{3.33}$$

and the power extraction fraction C_p is also given as:

$$C_p(\lambda, \beta) = 0.73\left(\frac{151}{\lambda'} - 0.58\beta - 0.002\beta^{2.14} - 13.2\right)e^{\frac{-18.4}{\lambda'}} \tag{3.34}$$

Figure 18 displayed the relationship between the wind power coefficient C_p and the pitch angles β. It shows that the wind power coefficient C_p depends on the blade pitch angle β. When the blade pitch angle is increased, the maximum power coefficient is increased. Since all the wind turbines are desired working under their maximum power generation conditions, most pitch angle controller is only applied to limit the wind power extraction when the induction generator reaches the rated power output. As in the standalone micro grid operation mode, the

pitch angle control is also applied in reducing the wind power extraction for avoiding the power over production in the microgrid.

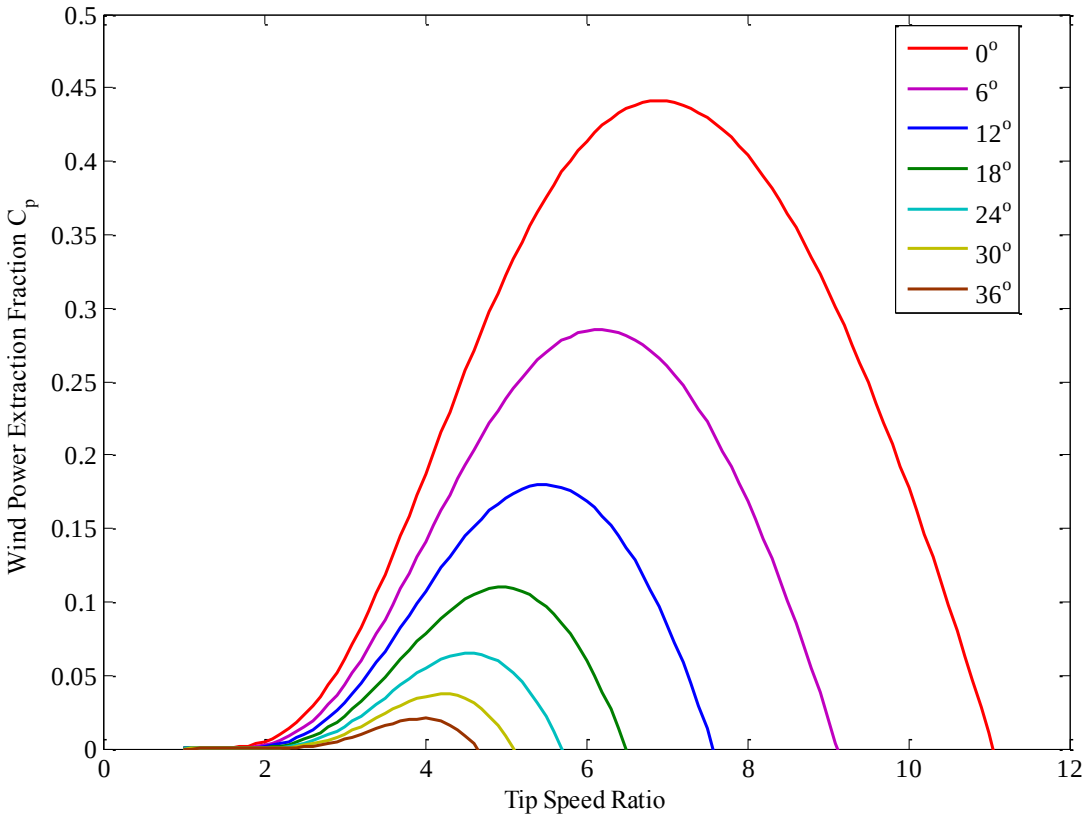

Figure 18. $C_P - \lambda$ curves for different pitch angles β .

If the pitch angle β is fixed, the maximum $C_{p,\max}$ is only decided by the optimal tip speed ratio λ_{opt}. When the wind speed v_w changes, wind turbine will tune the blade rotating speed ω_R to the optimal blade rotating speed $\omega_{R,opt}$, which is decided by the maximum tip speed ratio λ_{opt} as shown in Figure 19. The maximum wind power extracted from the wind yields:

$$P_{m,\max} = C_p\left(\lambda_{opt}, \beta\right)\left(\frac{1}{2}\rho A v_w{}^3\right) \tag{3.35}$$

And the optimal wind turbine angular speed at a given wind speed yields to:

$$\omega_{R,opt} = \frac{\lambda_{opt} v_w}{R} \tag{3.36}$$

The optimal tip speed ratio λ_{opt} is determined as:

when

$$\frac{dC_P}{d\lambda_i} = 0 \tag{3.37}$$

then

$$\lambda_{opt} = \lambda_i \tag{3.38}$$

where λ_i is the arbitrary tip speed ratio, which ranges from 0 to 8.

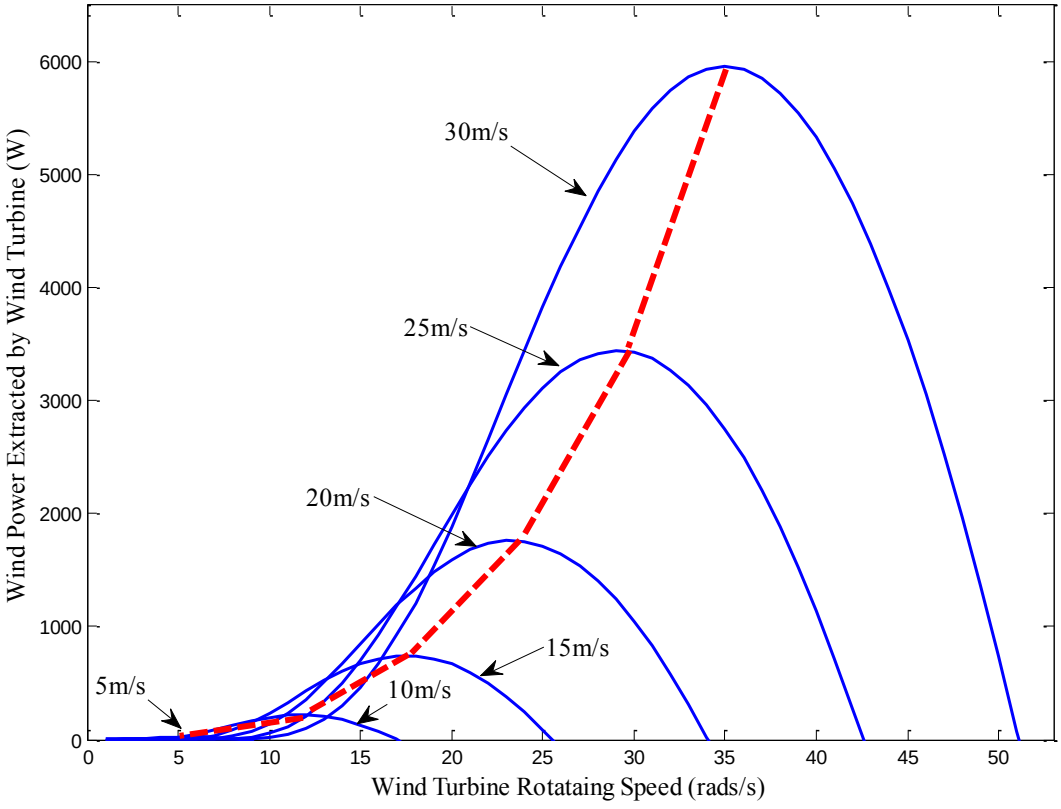

Figure 19. Wind turbine characteristic with the maximum power point tracking at fixed blade pitch angle $\beta = 0$.

3.3.2 Drive train modeling The fixed-speed wind turbine requires the detailed drive train model, like six mass drive train model, three mass drive train model, and two mass shaft model, to analyze the rotor rotational frequency oscillation caused by drive train self or mature damping. However, for a vary speed wind turbine with doubly fed induction generator (DFIG), the drive train properties have almost no effect on the grid side characteristics, because the decoupling effect of the power electronic converter [44]. Therefore, a one mass lumped model is applied in this study, as shown in Figure 20. In the one mass lumped model, the drive train components are lumped together as one rotating mass. The dynamic is given as:

$$\frac{d\omega_R}{dt} = \frac{T_{WT} - T_{EM}}{J_{RM}} \tag{3.39}$$

where ω_R is the rotor speed, T_{WT} is the input mechanical torque applied to the wind turbine, T_{EM} is the electromagnetic torque of the DFIG, and J_{RM} is the inertia of the rotating mass. Then the electromagnetic torque T_{EM} can be obtained by:

$$T_{EM} = T_{WT} - \frac{d\omega_R}{dt} J_{RM} \tag{3.40}$$

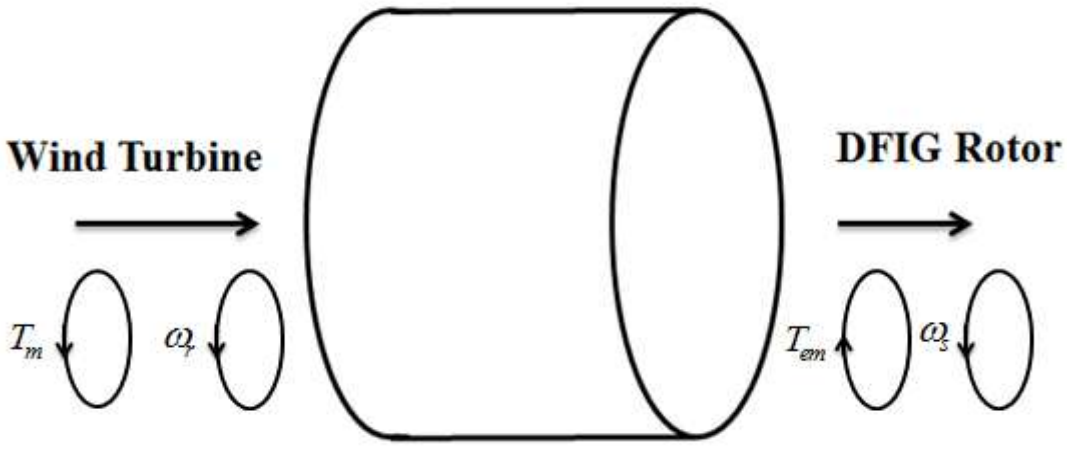

Figure 20. One-mass lumped mode of the drive train.

3.3.3 Doubly-fed induction generator (DFIG) modeling DFIG is the most widely-used induction generator for the variable speed wind energy conversion systems, as shown in Figure 21. The stator side is directly connected to the grid, and the rotor side is indirectly connected to the grid via a back to back converter, which consists of the rotor side converter and grid side converter. The rotor winding is fed by the rotor side converter to magnetize the induction generator, and the stator side converter is aim to maintain the constant DC-Link voltage.

Compared with other induction generator structures, DFIG has a larger acceptance of variable wind speeds. The back to back converter regulates a small percentage of the active power, which is able to reduce the power conversion loss.

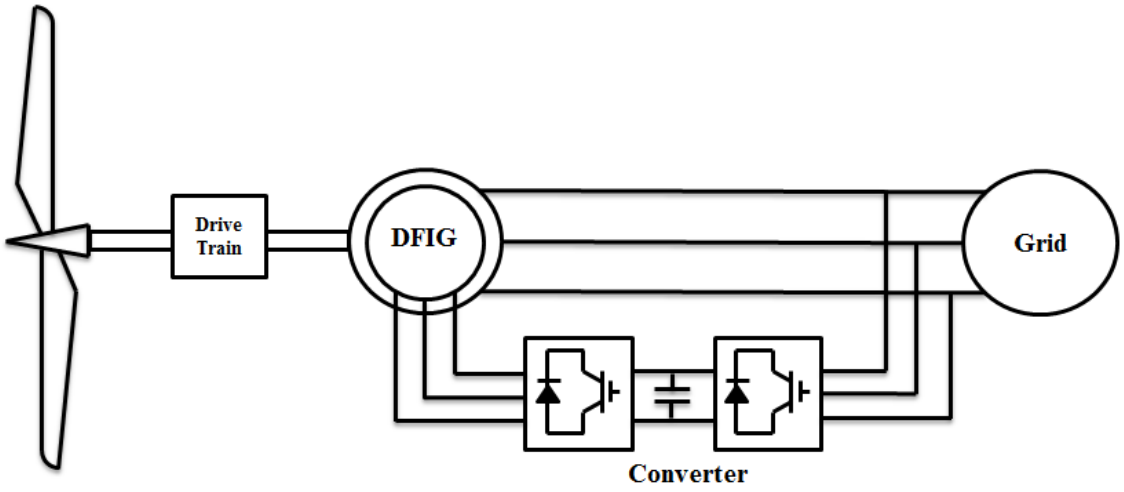

Figure 21. Diagram of variable speed wind turbine with DFIG.

3.3.3.1 Power flow in DFIG Compared with the conventional induction generator operation, the DFIG can produce the power when the slip ratio is positive (sub-synchronization operation), as shown in Figure 22. If ignore the stator and rotor resistances, the total active power contributed by DFIG is equal to the mechanical power extracted from the wind P_{mech}. The power P_{rotor} absorbed from the grid is use to offset the slip angular speed to make the DFIG work under equivalent synchronization condition.

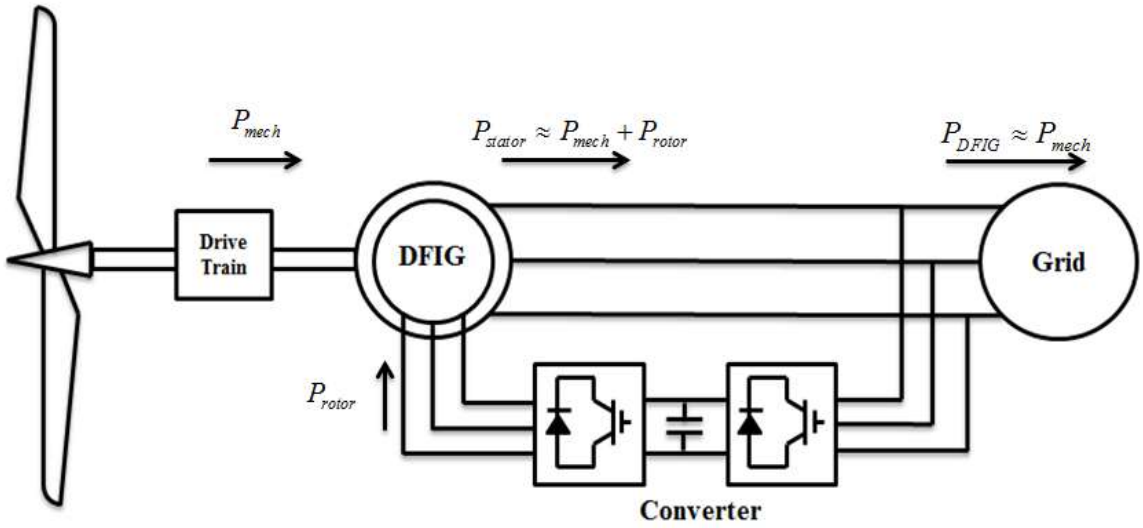

Figure 22. Power flow of DFIG under sub-synchronization operation.

Figure 23 displays the power flow of DFIG under super-synchronization condition. Because the rotor angular speed is higher than the synchronization speed, the direction of the rotor current will be changed from the rotor side to the grid side with the slip frequency for counteracting the exceeded rotor angular speed. As a result, the active power will delivered from the rotor side.

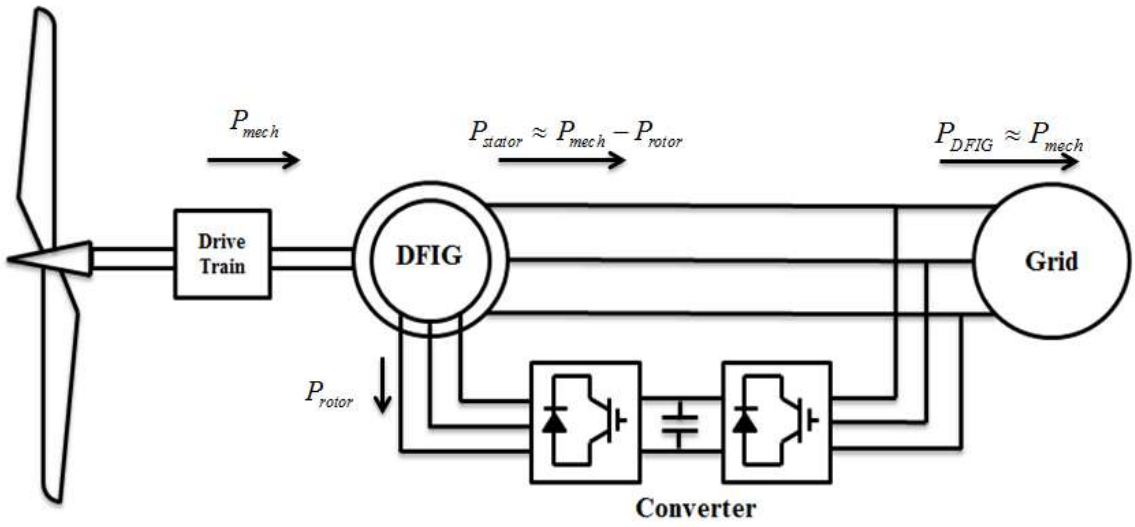

Figure 23. Power flow of DFIG under super-synchronization operation.

The total DFIG active power contribution is equal to the summation of the power from the rotor and stator. Under the steady state analysis, the power flow in DFIG can be described as following equations if ignore the stator and rotor resistances.

$$P_{mech} = P_{stator} - P_{rotor} \qquad \omega_r \le \omega_s \tag{3.41}$$

$$P_{mech} = P_{stator} + P_{rotor} \qquad \omega_r \ge \omega_s \tag{3.42}$$

where $P_{stator} = (1-s)\cdot P_{mech}$, $P_{rotor} = s \cdot P_{mech}$, and s is the slip ratio.

3.3.3.2 Dynamic DFIG modeling The dynamic DFIG model can be introduced from a wound rotor induction machine model [45-50]. The stator and rotor KVL equations can be written as:

$$v_{sabc} = R_s i_{sabc} + \frac{d\lambda_{sabc}}{dt} \tag{3.43}$$

$$v_{rabc} = R_r i_{sabc} + \frac{d\lambda_{rabc}}{dt} \tag{3.44}$$

where v_{rabc}, v_{sabc}, i_{sabc}, i_{rabc}, λ_{sabc}, λ_{rabc} are the three phase stator and rotor voltages, currents, and flux linkages, and R_s, R_r are the stator and rotor resistances, respectively. Applying the synchronously rotating reference frame transformation (from 3ϕ to the direct and quadrature axes) to Equations 3.43 and 3.44, the voltage equations become:

$$V_{ds} = \frac{d\lambda_{ds}}{dt} + R_s I_{ds} - \omega_s \lambda_{qs} \tag{3.45}$$

$$V_{qs} = \frac{d\lambda_{qs}}{dt} + R_s I_{qs} + \omega_s \lambda_{ds} \tag{3.46}$$

$$V_{dr} = \frac{d\lambda_{dr}}{dt} + R_r I_{dr} - (\omega_s - \omega_r)\lambda_{qr} \tag{3.47}$$

$$V_{qr} = \frac{d\lambda_{qr}}{dt} + R_r I_{qr} + \left(\omega_s - \omega_r\right)\lambda_{dr} \tag{3.48}$$

where ω_s is the rotational speed of the synchronous reference frame, ω_r is the rotor speed, and the stator and rotor flux linkages in the direct and quadrature axes are given by:

$$\lambda_{ds} = L_{ls} i_{ds} + L_m \left(i_{ds} + i_{dr}\right) = L_s i_{ds} + L_m i_{dr} \tag{3.49}$$

$$\lambda_{qs} = L_{ls} i_{qs} + L_m \left(i_{qs} + i_{qr}\right) = L_s i_{qs} + L_m i_{qr} \tag{3.50}$$

$$\lambda_{dr} = L_{lr} i_{dr} + L_m \left(i_{ds} + i_{dr}\right) = L_r i_{dr} + L_m i_{ds} \tag{3.51}$$

$$\lambda_{qr} = L_{lr} i_{qr} + L_m \left(i_{qs} + i_{qr}\right) = L_r i_{qr} + L_m i_{qs} \tag{3.52}$$

where $L_s = L_{ls} + L_m$, $L_r = L_{lr} + L_m$; L_{ls}, L_{lr} and L_m are the stator, rotor self-leakage, and mutual inductances, respectively.

The electromagnetic torque equation is given by:

$$T_e = -\frac{3}{4} P\left(\lambda_{ds} i_{qs} - \lambda_{qs} i_{ds}\right) \tag{3.53}$$

where P is number of pair of poles.

The stator active and reactive powers are given by:

$$P_s = \frac{3}{2}\left(v_{ds} i_{ds} + v_{qs} i_{qs}\right) \tag{3.54}$$

$$Q_s = \frac{3}{2}\left(v_{qs} i_{ds} - v_{ds} i_{qs}\right) \tag{3.55}$$

and the rotor active and reactive powers are given by:

$$P_r = \frac{3}{2}\left(v_{dr} i_{dr} + v_{qr} i_{qr}\right) \tag{3.56}$$

$$Q_r = \frac{3}{2}\left(v_{qr} i_{dr} - v_{dr} i_{qr}\right) \tag{3.57}$$

3.3.3.3 Stator flux oriented DFIG modeling Applying the stator flux oriented frame transformation, the direct axis of stationary frame is aligned with the stator flux linkage vector λ_s, or $\lambda_{ds} = \lambda_s$, and $\lambda_{qs} = 0$ [47, 49]. This transformation offers a convenience for modeling simplification by given the following relationships.

$$i_{qs} = -L_m i_{qr} / L_s \tag{3.58}$$

$$i_{ms} = \frac{V_{qs}}{\omega_s L_m} \tag{3.59}$$

$$i_{ds} = L_m (i_{ms} - i_{dr}) / L_s \tag{3.60}$$

$$P_s = -\frac{3}{2}\omega_s L_m^2 i_{ms} i_{qr} / L_s \tag{3.61}$$

$$Q_s = \frac{3}{2}\omega_s L_m^2 i_{ms}\left(i_{ms} - i_{dr}\right) / L_s \tag{3.62}$$

$$V_{dr} = R_r i_{dr} + \sigma L_r \frac{di_{dr}}{dt} - s\omega_s \sigma L_r i_{qr} \tag{3.63}$$

$$V_{qr} = R_r i_{qr} + \sigma L_r \frac{di_{qr}}{dt} + s\omega_s \left(\sigma L_r i_{dr} + L_m^2 i_{ms} / L_s\right) \tag{3.64}$$

where $\sigma = 1 - \frac{L_m^2}{L_s L_r}$ is defined as the leakage factor of the induction machine .

Therefore, Equations 3.61 and 3.62 state that the active and reactive powers of stator can be controlled independently by the rotor current in the direct and quadrature axes, i_{qr} and i_{dr}. The detailed derivation of Equations 3.61 and 3.62 can be found in [47]. The reference values of i_{qr} and i_{dr}, i_{qr}^* and i_{dr}^*, are introduced by the desired active power and reactive power demands.

Therefore it is possible to design the close loop error feedback PI controllers to make $i_{qr} \to i_{qr}^{*}$, and $i_{dr} \to i_{dr}^{*}$.

3.3.3.4 Rotor side converter control system design Let equations 3.63 and 3.64 become:

$$V_{dr} = V_{dr}^{'} - s\omega_s \sigma L_r i_{qr} \tag{3.65}$$

$$V_{qr} = V_{qr}^{'} + s\omega_s \left(\sigma L_r i_{dr} + L_m^2 i_{ms} / L_s\right) \tag{3.66}$$

where

$$V_{dr}^{'} = R_r i_{dr} + \sigma L_r \frac{di_{dr}}{dt} \tag{3.67}$$

$$V_{qr}^{'} = R_r i_{qr} + \sigma L_r \frac{di_{qr}}{dt} \tag{3.68}$$

Equations 3.67 and 3.68 indicate that i_{qr} and i_{dr} respond to $V_{qr}^{'}$ and $V_{dr}^{'}$ respectively. The errors between (i_{qr}^{*}, i_{qr}) and (i_{dr}^{*}, i_{dr}) are processed by the PI controller to give $V_{qr}^{'}$ and $V_{dr}^{'}$, respectively. As a result, the PI controllers for eliminating the rotor current errors are available. By using Equations 3.67 and 3.68, linear models (plants) for the rotor current control loops (a first order system) can be described by the transfer function listed below:

$$P(s) = \frac{i_{dr}(s)}{V_{dr}^{'}(s)} = \frac{i_{qr}(s)}{V_{qr}^{'}(s)} = \frac{1}{R_r + s\sigma L_r} \tag{3.69}$$

The integral action must be embedded in the controller design for eliminating the steady state error. It is therefore natural to use a PI controller, which can be formulated as:

$$C(s) = K_p + \frac{K_i}{s} \tag{3.70}$$

where K_p is the proportional gain and K_i is the integral gain. The open loop transfer functions of the systems are:

$$L(s) = P(s)C(s) = \frac{K_p s + K_i}{R_r s + s^2 \sigma L_r} \tag{3.71}$$

The transfer functions of the close loop systems from references i_{qr}^{*} and i_{dr}^{*} to outputs i_{qr} and i_{dr} are given by:

$$\frac{i_{dr}(s)}{i_{dr}^{*}(s)} = \frac{i_{qr}(s)}{i_{qr}^{*}(s)} = \frac{P(s)C(s)}{1 + P(s)C(s)} = \frac{K_p s + K_i}{s^2 \sigma L_r + (R_r + K_p)s + K_i} \tag{3.72}$$

and Equation 3.72 can be written as:

$$\frac{i_{dr}(s)}{i_{dr}^{*}(s)} = \frac{i_{qr}(s)}{i_{qr}^{*}(s)} = \frac{(K_p s + K_i)/\sigma L_r}{s^2 + (R_r + K_p)s/\sigma L_r + K_i/\sigma L_r} \tag{3.73}$$

The closed loop systems are of second order and their characteristic polynomials will be:

$$s^2 + (R_r + K_p)s/\sigma L_r + K_i/\sigma L_r \tag{3.74}$$

and Equation 3.74 can be re-parameterized as:

$$s^2 + 2\xi\omega s + \omega^2 \tag{3.75}$$

Instead of choosing controller parameters K_p and K_i, we now select ξ and ω. The parameter ω determines the speed of response and ξ determines the shape of response. If a model can be represented by a first order model, it is very convenient to have ξ and ω as controller parameters, also called the performance related parameters. Identifying the coefficients of the polynomials in Equation 3.74, the PI controller parameters are given by:

$$K_i = \omega^2 \sigma L_r \tag{3.76}$$

$$K_p = 2\xi\sigma\omega L_r \sqrt{L_r} - R_r \tag{3.77}$$

The system responses of system with different values of K_i and K_P are shown in Figure 24, which shows that parameter K_i essentially gives a time scaling, and the shape of the response is determined by K_P.

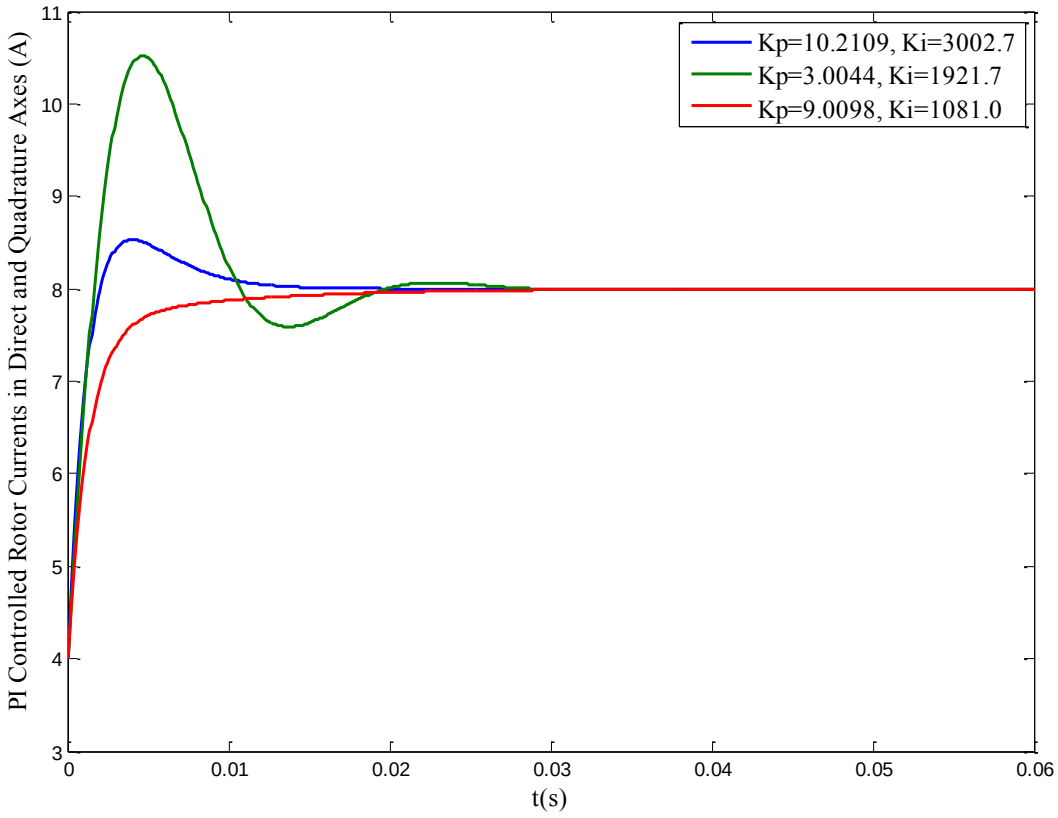

Figure 24. PI controlled rotor currents in direct and quadrature axes with different integral and proportional gains.

Based on the PI controllers developed above, Equations 3.63 and 3.64 can be revised as:

$$V_{dr}(t) = R_r i_{dr}(t) + \sigma L_r \frac{di_{dr}(t)}{dt} - s\omega_s \sigma L_r i_{qr}(t) \tag{3.78}$$

$$V_{qr}(t) = R_r i_{qr}(t) + \sigma L_r \frac{di_{qr}(t)}{dt} + s\omega_s \left(\sigma L_r i_{dr}(t) + L_m^2 i_{ms} / L_s\right) \tag{3.79}$$

where $i_{dr}(t)$ and $i_{qr}(t)$ is the step responses using the close loop PI control method; $V_{dr}(t)$ and $V_{qr}(t)$ is the reference signal for rotor side PWM converter. Figures 25 and 26 displayed the block diagrams of the rotor current close loop PI control systems.

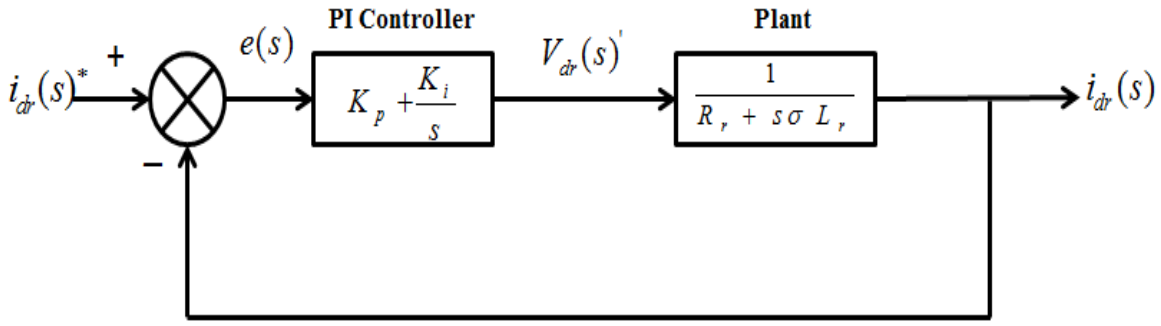

Figure 25. Close loop PI control scheme of rotor side current in direct axis.

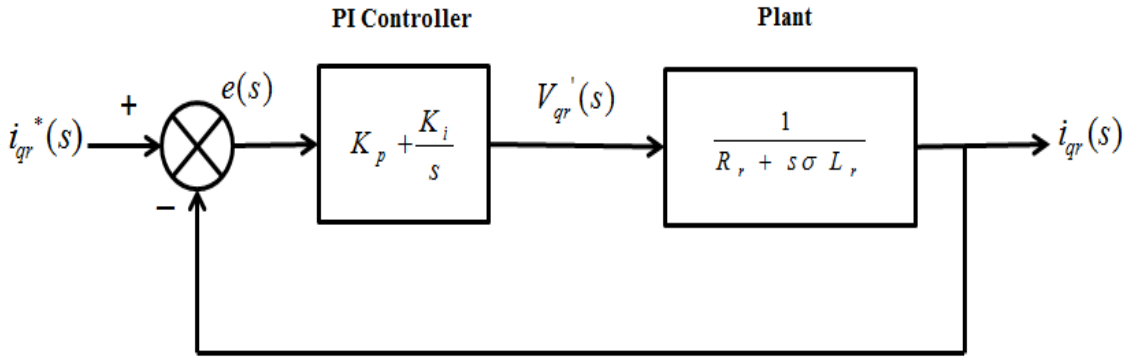

Figure 26. Close loop PI control scheme of rotor side current in quadrature axis.

3.3.3.5 Grid side converter control system design The grid side converter control scheme has two stages. The first stage is aim to regulate the grid side current components in the direct and quadrature axes, i_{dg} and i_{rg}, under the synchronous rotating frame. The second stage is to regulate the DC-link voltage and eliminate the reactive power exchanged between the grid side converter and the grid. The grid side circuit equation can be written as:

$$\frac{di_{abc}}{dt} = -\frac{R_g}{L_g} i_{abc} + \frac{1}{L_g}\left(V_{g,abc} - V_{s,abc}\right) \tag{3.80}$$

By applying the synchronously rotating frame transformation to Equation 3.80, with direct axis align to the grid voltage vector V_s ($V_{ds} = V_s$, $V_{qs} = 0$) [48], the converter side voltage components in the direct and quadrature axes, V_{dg} and V_{qg} can be obtained as:

$$V_{dg} = R_g i_{dg} + L_g \frac{di_{dg}}{dt} - \omega_s L_g i_{qg} + V_{ds} \tag{3.81}$$

$$V_{qg} = R_g i_{qg} + L_g \frac{di_{qg}}{dt} + \omega_s L_g i_{dg} \tag{3.82}$$

Following the similar procedure as Equations 3.65 to 3.68, V_{dg} and V_{qg} can be revised as:

$$V_{dg} = V_{dg}{}' - \omega_s L_g i_{qg} + V_{ds} \tag{3.83}$$

$$V_{qg} = V_{qg}{}' + \omega_s L_g i_{dg} \tag{3.84}$$

where

$$V_{dg}{}' = R_g i_{dg} + L_g \frac{di_{dg}}{dt} \tag{3.85}$$

$$V_{qg}{}' = R_g i_{qg} + L_g \frac{di_{qg}}{dt} \tag{3.86}$$

Equations 3.85 and 3.86 indicate that i_{qg} and i_{dg} respond to $V_{qg}{}'$ and $V_{dg}{}'$, respectively. The errors between ($i_{qg}{}^*$, i_{qg}) and ($i_{dg}{}^*$, i_{dg}) are processed by the PI controller to give $V_{qg}{}'$ and $V_{dg}{}'$, respectively. The reference grid current $i_{qg}{}^*$ in quadrature axis is determined directly based on the reactive power exchanged between the grid side converter and the grid and the reference grid current $i_{dg}{}^*$ in the direct axis determined based on the power balance of the DC link. PI controllers are designed for eliminate the grid current errors. Using Equations 3.85 and 3.86,

linear models (plants) for the grid current control loops (a first order system) can be described by the transfer function listed below:

$$P(s) = \frac{i_{dg}(s)}{V_{dg}^{'}(s)} = \frac{i_{qg}(s)}{V_{qg}^{'}(s)} = \frac{1}{R_g + sL_g} \tag{3.87}$$

The integral action must be embedded in the controller design for eliminating the steady state error. It is therefore natural to use PI controllers, which can be formulated as:

$$C(s) = K_p + \frac{K_i}{s} \tag{3.88}$$

where K_p is the proportional gain and K_i is the integral gain. The open loop transfer function of the system is:

$$L(s) = P(s)C(s) = \frac{K_p s + K_i}{R_g s + s^2 L_g} \tag{3.89}$$

The transfer functions of the closed systems from reference i_{qg}^{*} and i_{dg}^{*} to output i_{qg} and i_{dg} are given by:

$$\frac{i_{dg}(s)}{i_{dg}^{*}(s)} = \frac{i_{qg}(s)}{i_{qg}^{*}(s)} = \frac{P(s)C(s)}{1 + P(s)C(s)} = \frac{K_p s + K_i}{s^2 L_g + (R_g + K_p)s + K_i} \tag{3.90}$$

and Equation 3.90 can be written as:

$$\frac{i_{dg}(s)}{i_{dg}^{*}(s)} = \frac{i_{qg}(s)}{i_{qg}^{*}(s)} = \frac{(K_p s + K_i)/L_g}{s^2 + (R_g + K_p)s/L_g + K_i/L_g} \tag{3.91}$$

The closed loop systems are of second order and their characteristic polynomials will be:

$$s^2 + (R_g + K_p)s/L_g + K_i/L_g \tag{3.92}$$

and Equation 3.92 can be re-parameterized as:

$$s^2 + 2\xi\omega s + \omega^2 \tag{3.93}$$

Similarly applied the approach described in the last section, the PI controller parameters are obtained as:

$$K_i = L_g \omega^2 \tag{3.94}$$

$$K_p = 2\xi\omega L_g - R_g \tag{3.95}$$

Figures 27 and 28 displayed the block diagram of the grid current close loop PI control system in the direct and quadrature axes.

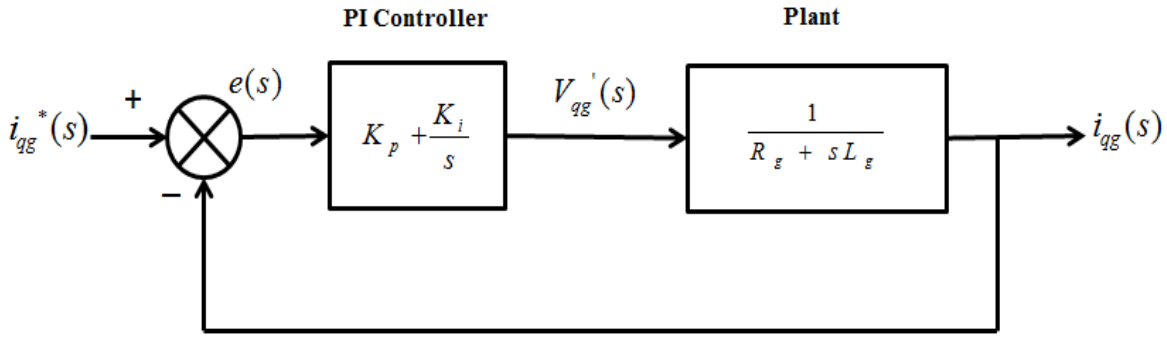

Figure 27. Close loop PI control scheme of grid side current in the quadrature axis.

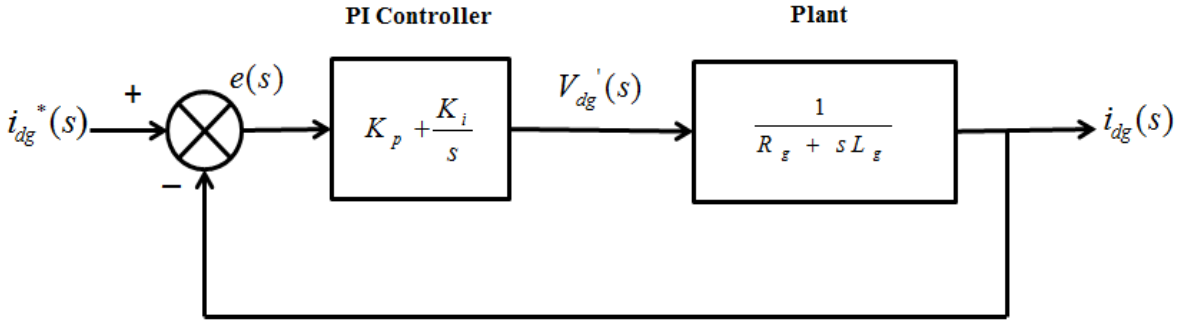

Figure 28. Close loop PI control scheme of grid side current in the direct axis.

If neglect the switching loss, the power balance equation of the DC link is written as:

$$P_r - P_g = 0 \tag{3.96}$$

since

$$P_g = \frac{3}{2} V_{ds} i_{dg} \tag{3.97}$$

then the reference value i_{dg}^{*} will be:

$$i_{dg}^{*} = \frac{2}{3} P_g / V_{ds} \tag{3.98}$$

since

$$Q_g = -\frac{3}{2} V_{ds} i_{qg} \tag{3.99}$$

then the reference value i_{qg}^{*} will be:

$$i_{qg}^{*} = -\frac{2}{3} Q_g / V_{ds} \tag{3.100}$$

3.3.3.6 Power electronic interface of the DFIG The highlight of DFIG is the back to back converter system. Most of the researches used the two voltage source converters to represent the bi-directional power converter system [49]. In this section, a dual channel back to back converter system realized the back to back converter as shown in Figure 29.

The three phase DC/AC inverter was discussed in section 3.2.3.2, and the three phase AC/DC converting is achieved by the three phase AC/DC full-wave bridge rectifier as shown in Figure 30. Only one diode in the top half will conduct at one time. It will have its anode connected to the highest phase to phase voltage at that instant. Only one diode in the bottom half will conduct at one time. It will have it cathode connected to the lowest phase to phase voltage at that instant. Because there are six combinations of phase to phase voltages, a transition of the highest phase to phase voltage will occur every 60^0. Figure 31(a) displayed the phase to neutral

voltage waveforms, and Figure 31(b) displayed phase to phase voltage waveforms and the output voltage waveform. The average voltage of the output voltage is:

$$V_o = \frac{1}{\pi/3}\int_{\frac{\pi}{3}}^{\frac{2\pi}{3}} V_{m,P-P}\sin(\omega t)d(\omega t) = \frac{3V_{m,P-P}}{\pi} \tag{3.101}$$

where $V_{m,P-P}$ is the peak line to line voltage, which is $\sqrt{2}V_{P-P,rms}$.

If the power extracted from the microgrid is P, we have

$$I_{s,rms} = \frac{P_{ac}}{\sqrt{3}V_{P-P,rms}} \tag{3.102}$$

then

$$I_o = I_{o,rms} = \sqrt{\frac{3}{2}}I_{s,rms} \tag{3.103}$$

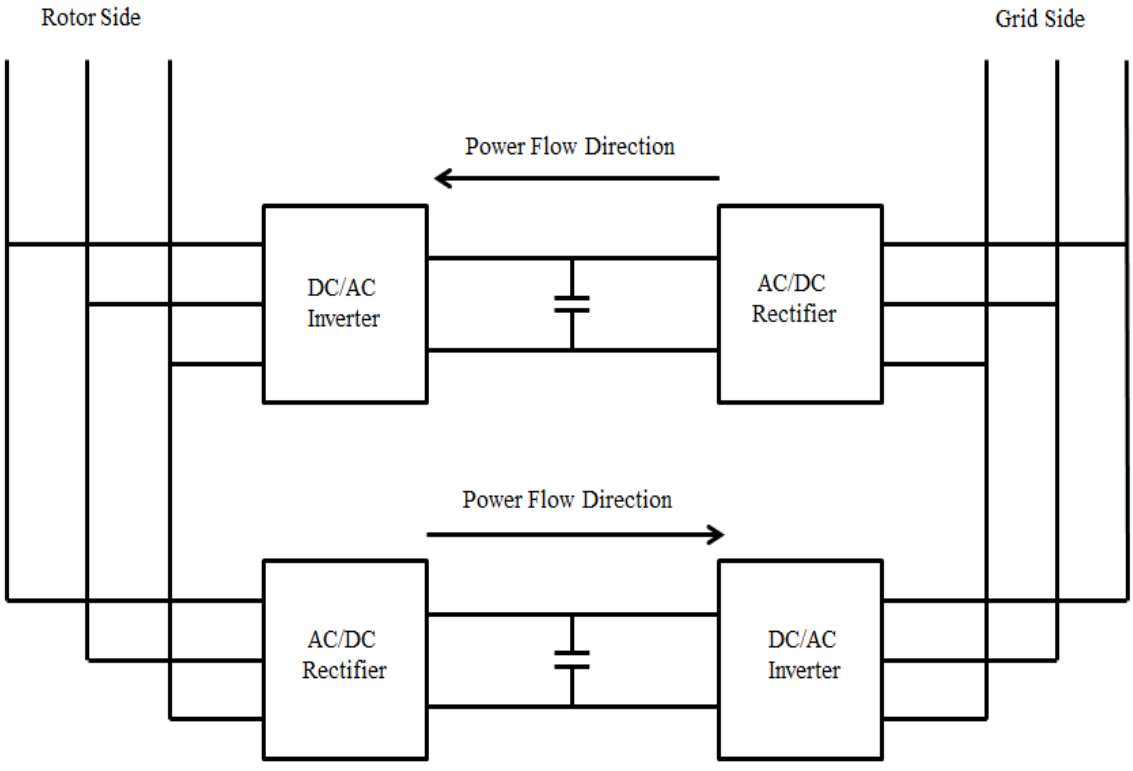

Figure 29. Dual channel back to back converter system.

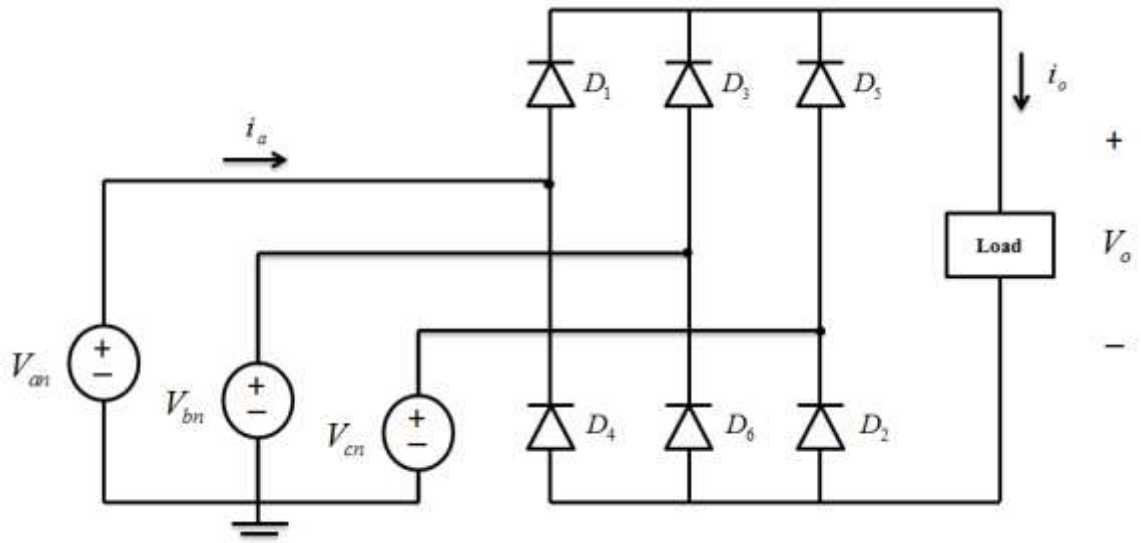

Figure 30. Three phase full bridge rectifier.

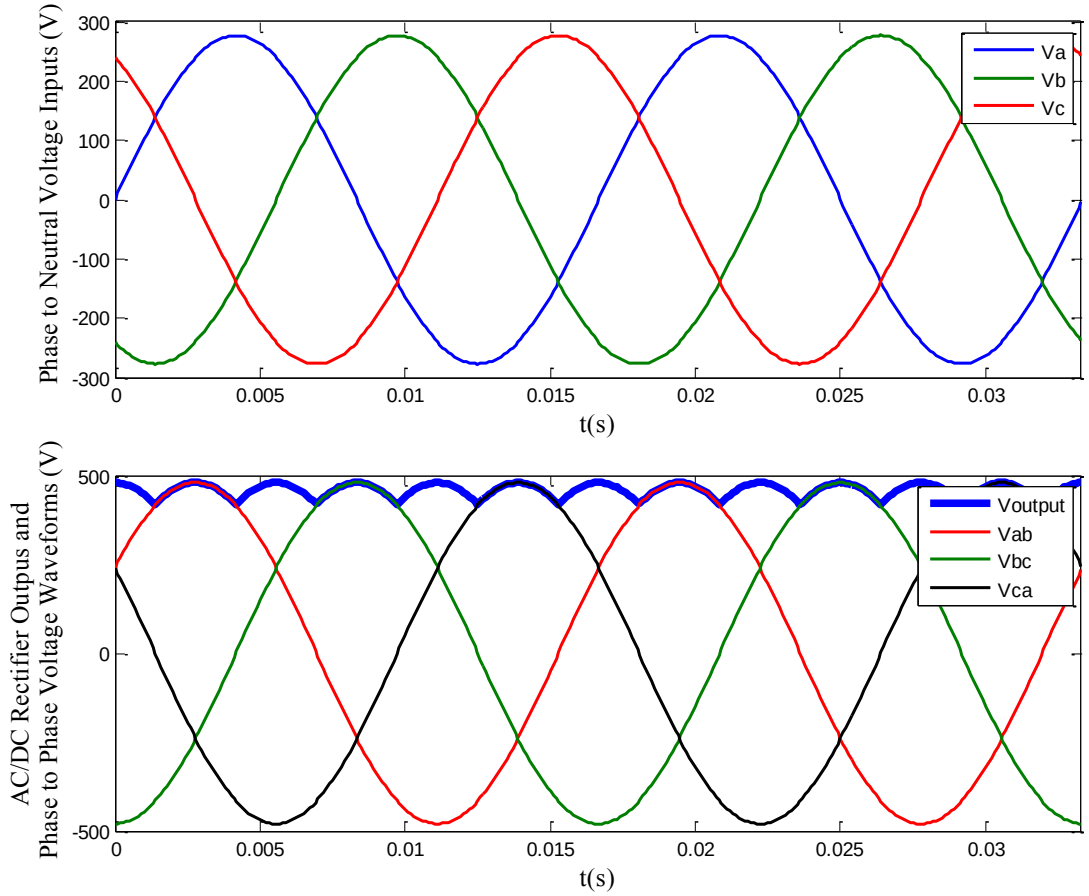

Figure 31. (a) Source voltages of a three phase full bridge rectifier. (b) rectifier voltage output and reference phase to phase voltage waveforms.

The DC power is given by:

$$P_{dc} = I_o \cdot V_o \tag{3.104}$$

Since $V_{m,P-P} = \sqrt{2}V_{P-P,rms}$, the efficiency of six pulse three phase AC/DC full-wave bridge rectifier is:

$$\eta_{ac\to dc} = \frac{P_{dc}}{P_{ac}} = \frac{3}{\pi} \approx 95.5\% \tag{3.105}$$

3.4 Distributed Energy Storage Modeling

3.4.1 Battery modeling The energy storage systems applied in the residential micro grid are commonly referred to the batteries. A widely used battery model is described by the following equation [51]:

$$E = E_0 + IR_{\text{int}} \tag{3.106}$$

where E is potential of a loaded battery (V), E_0 is standard potential of a battery (V), and R_{int} is the internal resistance of a battery (Ohm). This equation is assumed that the battery has a fixed open circuit potential and the loaded potential varies linearly with the applied current. As a result, limited energy is available from a battery and it also can not reflect the fact that the open circuit potential of a battery changes with the state of charge (SOC). According to these disadvantages, a developed model is presented in this research for avoiding the over simplification issues by using equation above.

Figure 32 displayed a simple RC model for a general battery, and the governing equation given by [51, 52]:

$$E = E_{eq} + IR_{\text{int}} \tag{3.107}$$

where E_{eq} is the open-circuit potential of a battery at a particular state of charge (V), which can be fitted in by the experimental data:

$$E_{eq} = f\left(SOC\right) \tag{3.108}$$

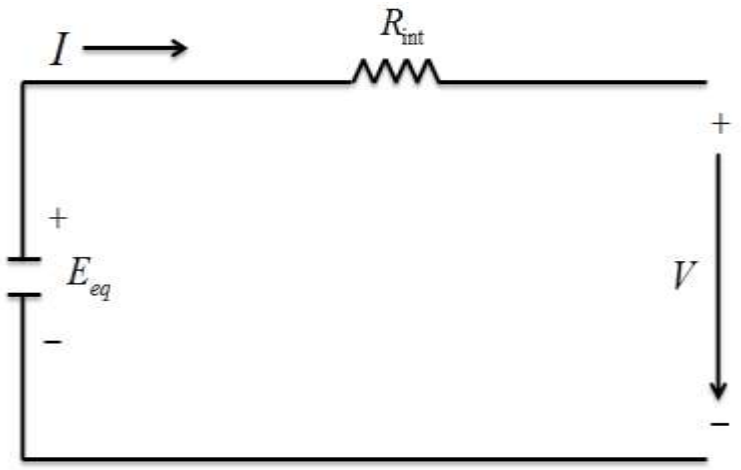

Figure 32. Equivalent RC model of a general battery.

If the following assumptions are valid: If the following assumptions are valid: the Nernst equation is a valid description of the equilibrium potential of the relevant electrochemical reactions; the main electrochemical reactions on positive and negative electrodes have fast kinetics; the capacity of the positive electrode roughly matches that of the negative electrode, the open-circuit potential of a battery at a particular state of charge will be [51, 52]:

$$E_{eq} = E_0 + \frac{RT}{nF}\ln\left(\frac{SOC}{1-SOC}\right) \tag{3.109}$$

where R is the ideal gas constant (8.3143 J/mole/K), T is the temperature in K, n is the electron transfer number of the whole battery electro-chemical reaction, E_0 is the standard potential of a battery (V), and F is the Faradic constant (98467 C/eq). Assuming that there are no side reactions, then the relationship between SOC and charge/discharge rate is as follow:

$$\frac{dSOC}{dt} = \frac{I}{3600C_{battery}} \tag{3.110}$$

where $C_{battery}$ is the capacity of the battery (Ah). If the battery is absorbing or contributing the power P from or to the grid, the DC current I and the terminal voltage V has the relationship as following:

$$P = V \cdot I \tag{3.111}$$

and

$$I = \frac{E_{eq} - V}{R_{\text{int}}} = \frac{E_0 + \frac{RT}{nF}\ln\left(\frac{SOC}{1-SOC}\right) - V}{R_{\text{int}}} \tag{3.112}$$

By solving the Equations 3.111 and 3.112, the terminal voltage V and the current I are obtained. By using Equation 3.110, the battery charging or discharging rate is able to be determined at a particular power output.

3.4.2 Distributed energy storage design The distributed energy storage is a key component in the proposed microgrid in this research. In the grid-tied operation, the distribution substation acts the swing bus for power flow balancing. However, when the microgrid is in autonomous operation mode, there is no connection to the distribution substation. As a result, it is mandatory to find the other bus to replace the role of the substation for balancing the power flow in the microgrid. According to the nature of renewable distributed generators, they are not qualified for this function. The only choice left is the distributed energy storage. It is necessary to properly design the electronic interface of the DES for realizing the desired function, which are required for delivering the power in bi-direction. When the energy storage is absorbing the power, an AC/DC/DC inverter system is needed. When the energy storage is contributing the power, a DC/DC/AC inverter system is needed. Figure 33 displays the proposed DES diagram.

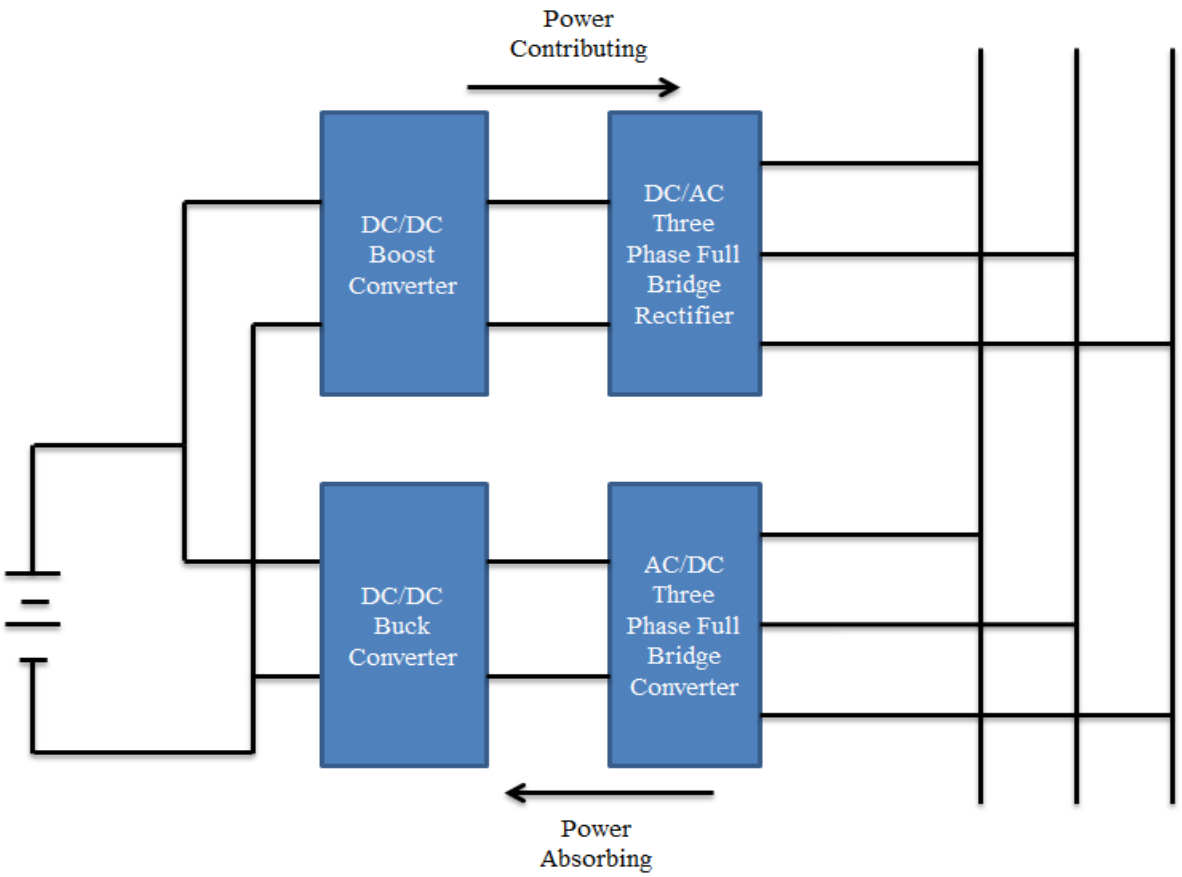

Figure 33. Proposed distributed energy storage system.

According to Figure 33, the power electronic interface of the distributed energy storage is consisting of two inverting channels, which is similar with the back to back converter. An AC/DC three phase full bridge rectifier is needed for inverting the bus voltage and current from sinuous waveform to DC waveform. An inductive DC/DC buck converter are added for stepping down the voltage level to the battery group terminal voltage level at the DC terminal of the AC/DC three phase full bridge converter. When the DES is absorbing the power from microgrid, an inductive DC/DC boost converter is required to step up the battery group terminal voltage to the DC terminal voltage level at the DC end of the three phase full bridge DC/AC inverter. The three phase full bridge DC/AC inverter transfers the DC waveform to the AC waveform, when the distributed energy storage is contributing the power to the microgrid.

By using the active and reactive power decoupling control, the AC voltage waveforms inverted by the DC/AC three phase full bridge rectifier are synchronized with the bus voltage waveforms. The angle between output voltage and current is under control, which allows the distributed energy storage generate the desired active power and reactive power.

The inductive DC/DC buck converter equivalent circuit is shown in Figure 34 (a). The operation mode consists two phases [40]:

1. The inductor charge phasing: The equivalent circuit for this phase is shown in Figure 34(b), which is achieved by opening switch 1 and closing switch 2 for a certain period t_{on}. During this phase, the inductor L is charge by the voltage source U_{high}, causing the inductor current $i_L(t)$ to increase from its minimum value $i_{L,\min}$ to its maximum value $i_{L,\max}$. The voltage cross the inductor is:

$$U_L = U_{high} - U_{low} = L\frac{di_L}{dt} \tag{3.113}$$

after rearranging,

$$\frac{di_L}{dt} = \frac{U_{high} - U_{low}}{L} \tag{3.114}$$

Since the derivative of the inductor current is a positive constant, the current increases linearly. The current change over the inductor while switch 2 is closed is given by:

$$\frac{di_L}{dt} = \frac{U_{high} - U_{low}}{L} = \frac{\Delta i_L}{\Delta t} = \frac{\Delta i_L}{DT} \tag{3.115}$$

$$\Delta i_{L,\varphi 1} = \left(\frac{U_{high} - U_{low}}{L}\right)DT \tag{3.116}$$

where T is the switch period; DT is the time when switch is closed.

2. The inductor discharging phase: The equivalent circuit for this phase is shown in Figure 34(c), which is achieved by opening switch 2 and closing switch 1 for a certain period t_{off} . The voltage cross the inductor is:

$$U_L = -U_{low} = L\frac{di_L}{dt} \tag{3.117}$$

after rearranging,

$$\frac{di_L}{dt} = \frac{-U_{low}}{L} \tag{3.118}$$

Since the derivative of the current is a negative constant, the current decreases linearly. The current change over the inductor while switch 2 is open is given by:

$$\frac{di_L}{dt} = \frac{-U_{low}}{L} = \frac{\Delta i_L}{\Delta t} = \frac{\Delta i_L}{(1-D)T} \tag{3.119}$$

$$\Delta i_{L,\varphi 2} = \left(\frac{-U_{low}}{L}\right)(1-D)T \tag{3.120}$$

The steady state operation requires the inductor current at the beginning of the switching cycle is equal to that at the end of the switching cycle. This requires:

$$\Delta i_{L,\varphi 1} = \Delta i_{L,\varphi 2} \tag{3.121}$$

Using Equations 3.116 and 3.120, we get:

$$\left(\frac{U_{high}-U_{low}}{L}\right)DT + \left(\frac{-U_{low}}{L}\right)(1-D)T = 0 \tag{3.122}$$

It yields:

$$U_{low} = U_{high}\cdot D \tag{3.123}$$

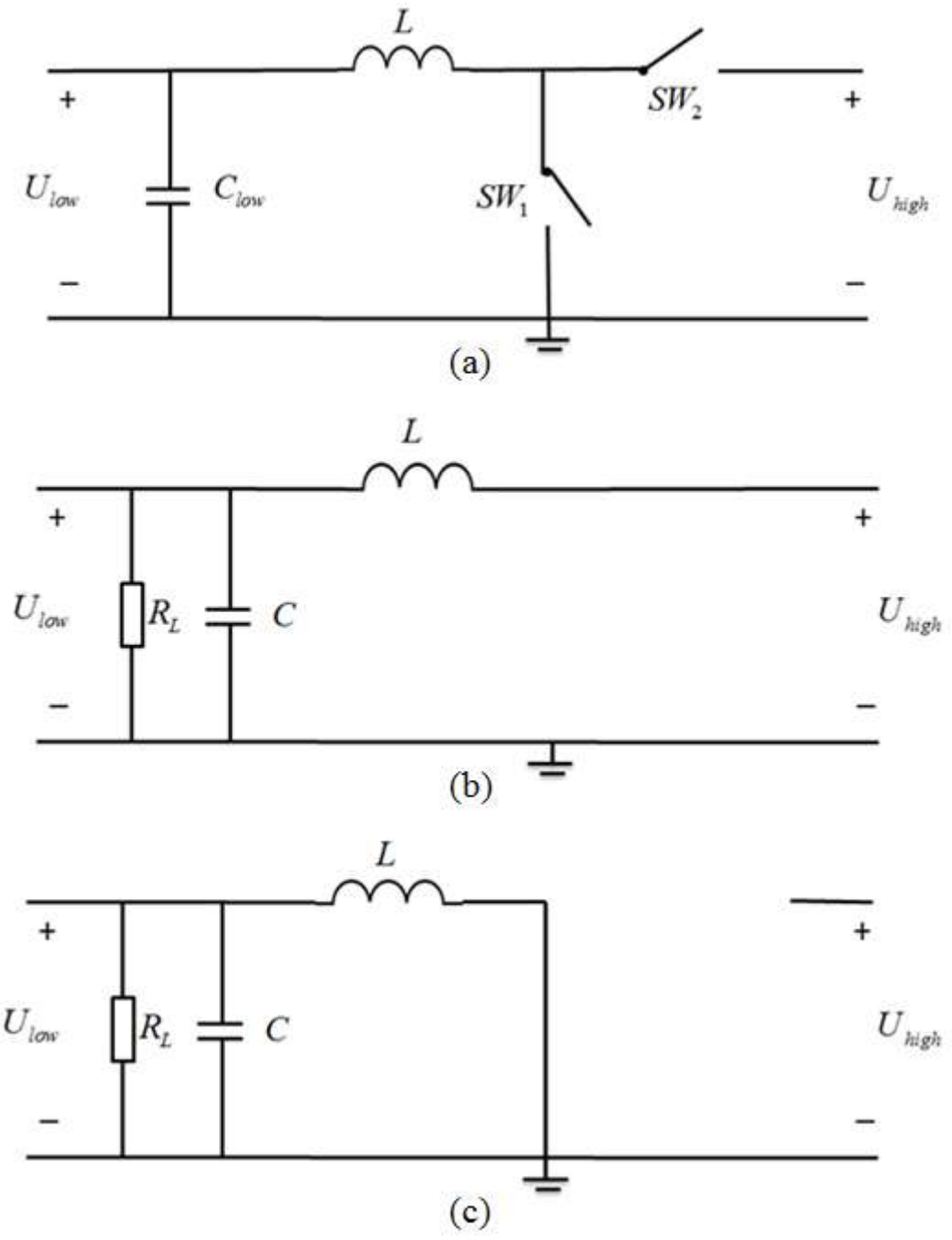

Figure 34. (a) Circuit of the DC/DC buck converter, (b) equivalent circuit of the inductor charge phase, and (c) equivalent circuit of the inductor discharge phase.

3.4.3 Distributed energy storage P, Q decoupling control system design The reference three phase voltage signals sent to the PWM of the three phase DC/AC full bridge rectifier can

also be controlled by using the active power and reactive power decoupling control. Figure 35 displays the equivalent circuit diagram when the converter connects to the microgrid. The subscript s denotes the system side, and c denotes the converter side. R and L are the connection resistance and reactance, and i_a is the phase a to ground current. The three phase Kirchhoff voltage law equations of the diagram are:

$$V_{ca} - V_{sa} = Ri_a + L\frac{di_a}{d_t} \tag{3.124}$$

$$V_{cb} - V_{sb} = Ri_b + L\frac{di_b}{d_t} \tag{3.125}$$

$$V_{cc} - V_{sc} = Ri_c + L\frac{di_c}{d_t} \tag{3.126}$$

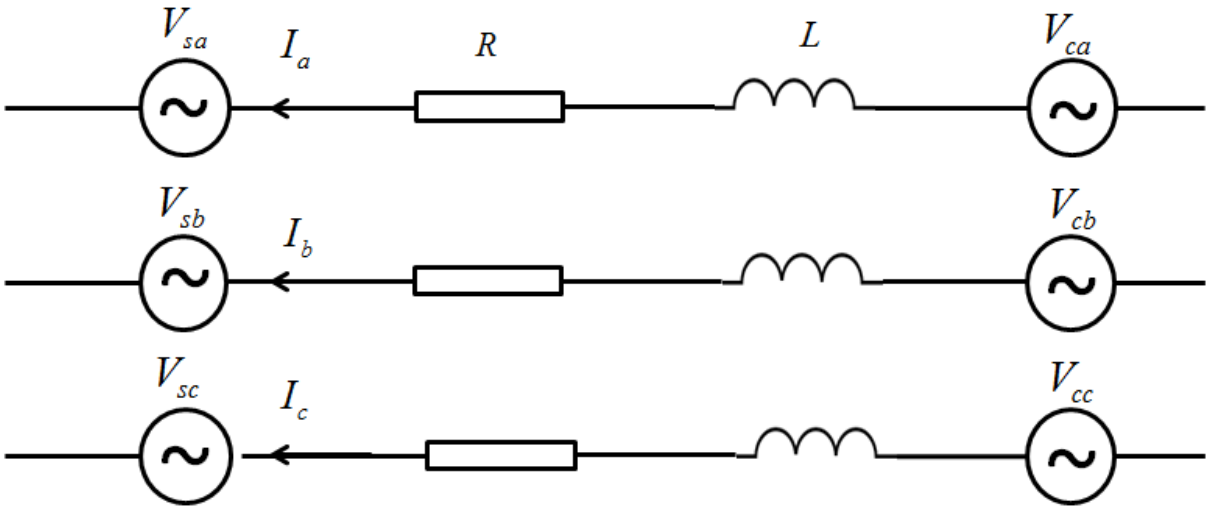

Figure 35. Equivalent circuit of the three phase DC/AC full bridge rectifier connected to the microgrid.

By using the Park transformation and align to the system voltage direct axis reference framework, the direct and quadrature axes KVL equations will be:

$$V_{cd} - V_{sd} = Ri_d + L\frac{di_d}{dt} - wLi_q \tag{3.127}$$

$$V_{cq} - V_{sq} = Ri_q + L\frac{di_q}{dt} + wLi_d \tag{3.128}$$

where w is the system frequency.

Since $V_{sd} = 0$, $V_{sq} = V_s$,

then

$$P = \frac{3}{2}V_{sq}I_q \tag{3.129}$$

$$Q = \frac{3}{2}V_{sq}I_d \tag{3.130}$$

The above equations state that active power and reactive power are controlled by I_q and I_d respectively. After adding the two compensation terms V_{cd}' and V_{cq}', Equations 3.127 and 3.128 can be rewritten as:

$$V_{cd} = V_{cd}^{'} - wLi_q + V_{sd} \tag{3.131}$$

$$V_{cq} = V_{cq}^{'} + wLi_d + V_{sq} \tag{3.132}$$

where $V_{cd}^{'} = RI_d + L\frac{dI_d}{dt}$ and $V_{cq}^{'} = RI_q + L\frac{dI_q}{dt}$. If we denote the I_q^* and I_d^* as the target values of the I_q and I_d, the required rectifier AC terminal voltages in the direct and quadrature axes will be obtained by applying two PI controllers. The entire feed forward decoupling control diagram based on Equations 3.133 and 3.134 is shown in Figure 36.

$$V_{cd} = \left(K_I + \frac{K_P}{s}\right)\left(i_d - i_d^*\right) - wLi_q + V_{sd} \tag{3.133}$$

$$V_{cq} = \left(K_I + \frac{K_P}{s} \right) \left(i_q - i_q^* \right) + wLi_d + V_{sq} \tag{3.134}$$

where K_p is the proportional gain and K_I is the integral gain.

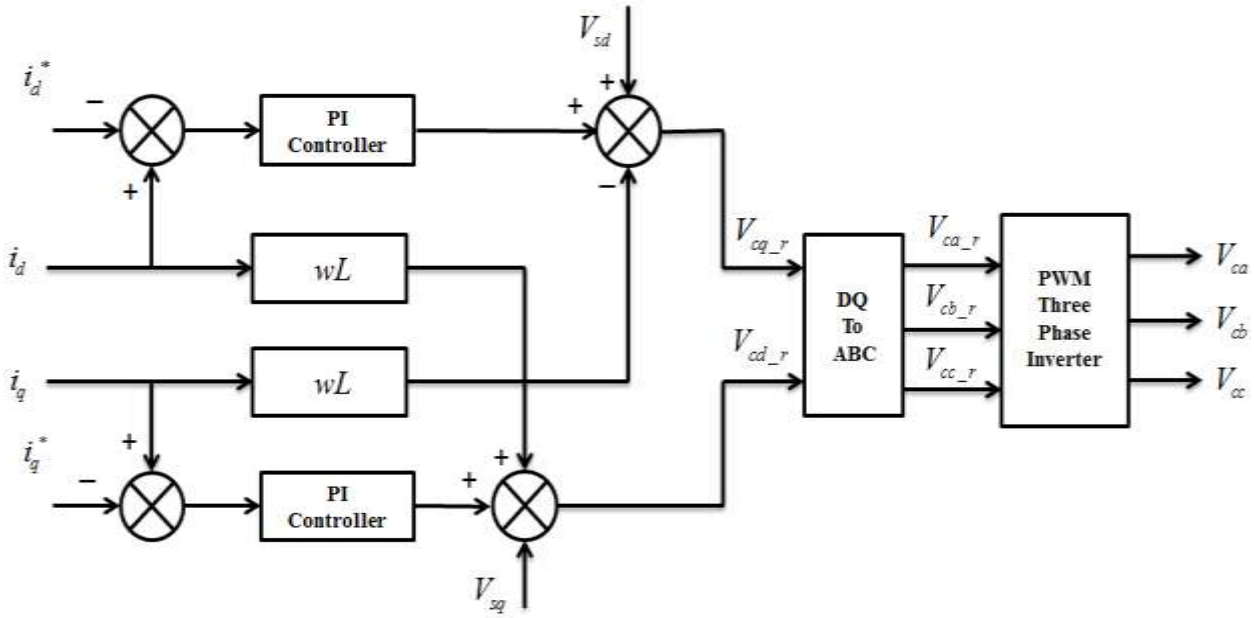

Figure 36. P, Q decoupling control diagram of the three phase full bridge DC/AC rectifier.

CHAPTER 4

Residential Microgrid Power Flow Analysis

4.1 Introduction

Power flow calculation is a cluster of numerical analysis methods to evaluate the steady or transient performance of the power flow in the AC power system. The classic approaches include the Gauss-Seidel Method, the Newton-Raphson method, and the fast decoupled method, which are capable of solving the nonlinear equations. In the power flow analysis, the bus in a grid can be divided into three classes, the generation bus (PV bus), the load bus (PQ bus), and the balance bus (the swing bus or the slack bus). Each type of the bus has four parameters, the voltage magnitude, the voltage phase angle, the active power injection, and the reactive power injection. According to the abbreviations in the brackets, each bus has two known parameters and two unknowns as listed in the following table, where P is the active power, Q is the reactive power, V is the line to ground voltage magnitude, and δ is the line to ground voltage phase angle.

Table 2

Bus Type Classification in the Power Flow Calculation

Bus Types	Knowns		Unknows	
PV	P	V	Q	δ
PQ	P	Q	V	δ
Swing	V	δ	P	Q

The purpose of the power flow calculation is to acquire the converged voltage vectors of the buses with the specified active power and reactive power injections [53]. The bus injection

current $\dot{I}_i$ in terms of the bus apparent power injection $\dot{S}_i$ and the bus voltage $\dot{V}_i$ in a n buses system can be described as:

$$\dot{I}_i = \frac{\overset{*}{S_i}}{\overset{*}{V_i}} = Y_{i1}\dot{V}_1 + Y_{i2}\dot{V}_2 + \cdots + Y_{in}\dot{V}_n \tag{4.1}$$

where Y_{in} is the admittance between the i_{th} bus and the n_{th} bus, and $*$ is the symbol of conjunction. Equation 4.1 can be rewritten as:

$$P_i - jQ_i = \overset{*}{V_i} \cdot \left(Y_{i1}\dot{V}_1 + Y_{i2}\dot{V}_2 + \cdots + Y_{in}\dot{V}_n \right) \tag{4.2}$$

If the real and the imaginary portions of Equation 4.2 are separated, two real number equations will be obtained for each bus as follows:

$$P_i = real\left[V_i^* \cdot \left(Y_{i1}\dot{V}_1 + Y_{i2}\dot{V}_2 + \cdots + Y_{in}\dot{V}_n \right) \right] \tag{4.3}$$

$$Q_i = -imag\left[V_i^* \cdot \left(Y_{i1}\dot{V}_1 + Y_{i2}\dot{V}_2 + \cdots + Y_{in}\dot{V}_n \right) \right] \tag{4.4}$$

With at least two known parameters, the other unknown parameters will be solved by using the power flow calculation methods. The Gauss-Seidel method is chosen to solve the power flow equations and will be introduced in the next section.

4.2 Research System Power Flow Analysis Using the Gauss-Seidel Method

The operation of a microgrid can be divided into two modes, the grid-tied mode and the grid-off mode. In the grid-tied mode, the load bus is connected to the bulk grid and the microgrid. Figure 37 displays the one-line diagram of the system in the grid-tied mode. Once the distributed energy storage is fully charged, the power flow from the distributed generators

will bypass the distributed energy storage and feed the residential load directly. If the power flow from the distributed generators is sufficient, the microgrid will deliver the extra energy back to the bulk grid. In this particular system topology, the bulk grid can be looked as an infinity bus, and the distribution substation will be considered as the slack bus. The power output from the distributed generators will be always at their maximums.

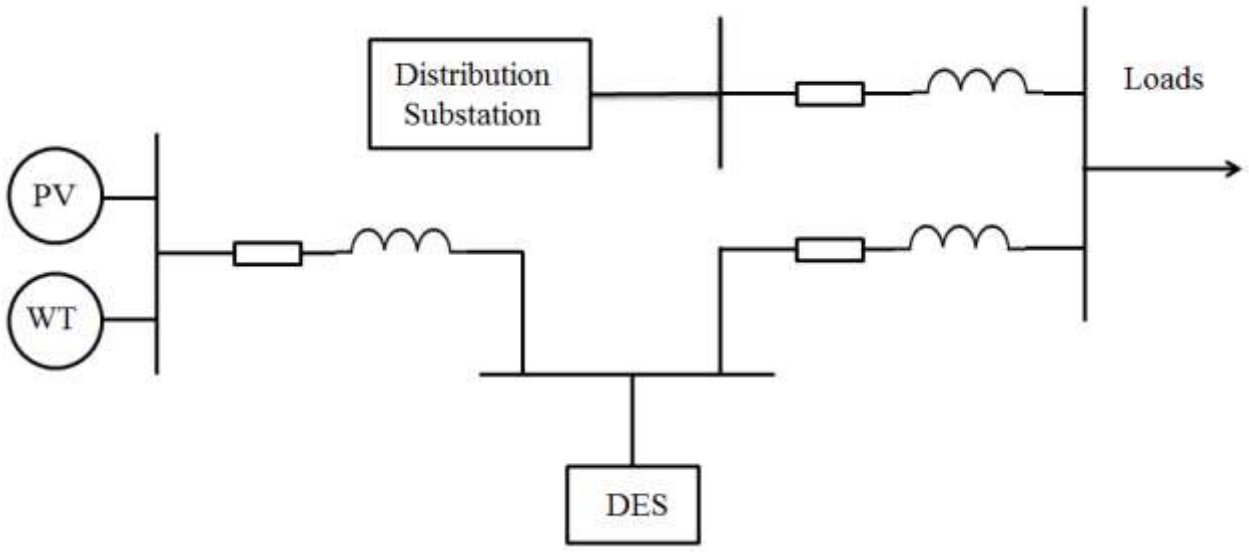

Figure 37. One-line diagram of the research system in grid-tied mode.

Once the faults happened in the bulk grid side or the microgrid is designed for the grid-off operation only, the grid-tied mode will transfer to the grid-off mode, which means the microgrid is disconnected to the bulk grid. Figure 38 shows the one-line diagram of the research system in the grid-off mode. The main issue for the microgrid in the grid-off mode is the lack of sufficient power resource, which is able to act as the slack bus for balancing the system power flow. In this research, the distributed energy storage system is designed for realizing the slack bus function. The PV bus is the generation bus, which summarizes the wind power energy systems and the solar energy systems. The PQ bus is the residential load bus.

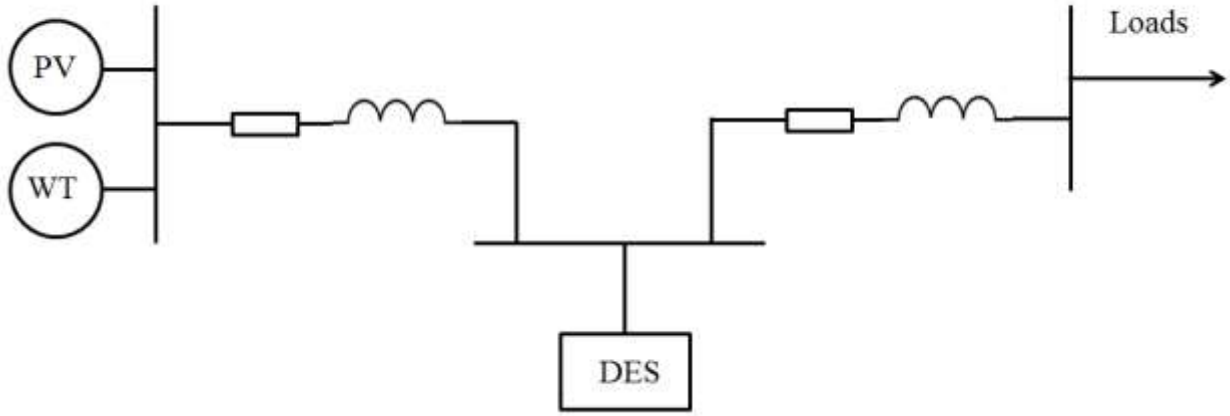

Figure 38. One-line diagram of the research system in grid-off mode.

If we denote the slack bus is bus 1, PQ bus is bus 2, and PV bus is bus 3, the admittance matrix will be:

$$Y = \begin{bmatrix} \frac{1}{z_{12}} + \frac{1}{z_{13}} & -\frac{1}{z_{12}} & -\frac{1}{z_{13}} \\ -\frac{1}{z_{12}} & \frac{1}{z_{12}} & 0 \\ -\frac{1}{z_{13}} & 0 & \frac{1}{z_{13}} \end{bmatrix} \tag{4.5}$$

Equation 4.2 can be rewritten as:

$$V_i = \frac{1}{Y_{ii}} \left[\frac{P_i - Q_i}{V_i^*} - Y_{i1}V_1 - Y_{i2}V_2 - \cdots - Y_{in}V_n \right] \tag{4.6}$$

By using the Gauss-Seidel method [53], the voltage vector of a PQ bus will be:

$$V_2^{(1)} = \frac{1}{Y_{22}} \left[\frac{P_2 - Q_2}{V_2^{*(0)}} - Y_{21}V_1^{(1)} - Y_{23}V_3^{(0)} \right] \tag{4.7}$$

Because the voltage magnitude and the active power injection of a PV bus are fixed, the voltage angle updating is based on the updating of the reactive power injection of that bus. Equation 4.4 will be revised as:

$$Q_3^{(1)} = -imag\left[V_3^{*(0)} \cdot \left(Y_{31}\dot{V}_1^{(1)} + Y_{32}\dot{V}_2^{(1)} + Y_{33}\dot{V}_3^{(0)}\right)\right] \tag{4.8}$$

The update voltage vector of a PV bus will be:

$$V_3^{(1)} = \frac{1}{Y_{33}}\left[\frac{P_3 - jQ_3^{(1)}}{V_3^{*(0)}} - Y_{31}V_1^{(1)} - Y_{32}V_2^{(1)}\right] \tag{4.9}$$

Sometimes Equation 4.9 will change the voltage magnitude of a PV bus, therefore the magnitude of a PV bus should be forced to the pre-specified value, which is accomplished by:

$$V_3^{(1)} = \left|V_{3,spec}\right| \cdot \frac{V_3^{(1)}}{\left|V_3^{(1)}\right|} \tag{4.10}$$

Keep updating the voltage vectors at each bus until Equations 4.11 and 4.12 are met.

$$\left|V_i^{(n)}\right| - \left|V_i^{(n-1)}\right| \le \varepsilon \tag{4.11}$$

$$\left|\delta_i^{(n)}\right| - \left|\delta_i^{(n-1)}\right| \le \varepsilon \tag{4.12}$$

Equations 4.11 and 4.12 are aim to check whether the voltage vector of each bus is converged both in magnitude and angle, and ε is a preset threshold, $\varepsilon \approx 0$. Once all the bus voltage vectors are converged, the updated power injection at each bus can be obtained by using Equations 4.3 and 4.4.

4.3 Autonomous Microgrid Topology Finalization and Operation Procedure

In Chapter 2, the optimal sizing of the distributed renewable generators is discussed. In this section, the selection of other microgrid parameters will be presented. All of these parameters and operation procedure are designed under the microgrid autonomous operation mode.

The first unknown parameter is the impedance or admittance of the transmission lines in the microgrid. When using the Gauss-Seidel method for calculating the power flows in the microgrid, it is possible that one or more bus voltage vectors are not converged. The reason is that the Gauss-Seidel method cannot find the voltage magnitudes or angles in the real number space. In practice, the causations is that the admittance of the conductor between the PV bus and PQ bus is lower than the minimum required admittance or the overall microgrid voltage level is lower than the minimum required voltage level that ensures the power transmission stability. To fix the non-convergence problem of the Gauss-Seidel method, the admittance between the PV bus and PQ bus will be increased, which means the length of the transmission line should be reduced or the conduct of transmission lines should be replaced by others with higher admittance. In this research, this is the only solution considered, because the microgrid is directly coupled with the residential distribution network. Increasing the overall microgrid voltage level may cost additional investments.

The second unknown parameter is the minimum size of the distributed energy storage. In some season, the wind and solar energy are in their annul valleys and the residential load still remains at a high level. If the capacity of the distributed energy storage is low, it cannot deliver sufficient power required from the end users. As a result, the reliability of power supplement will be critically threatened, and the end users will face the power outages frequently during that

season. The state of charge (SOC) represents the amount of energy saved in the distributed energy storage. If the SOC is less than 0, which means the energy saved in the battery bank is over drawn. The capacity of the battery system is not large enough to save the sufficient energy for compensating the power shortages. Another battery cell should connect to the distributed energy storage in parallel for increasing the capacity of the battery system. Keep increasing the capacity of the battery bank until the SOC remains positive during the planned project life time.

After the impedance of transmission lines and the minimum size of the distributed energy storage are determined, the residential microgrid topology is finalized.

The optimal sizes of the distributed generators are decided for supplying the maximum residential load at the month, when the solar and wind energy are at the annual valleys. In most scenarios, the power generated from the distributed generators is larger than the residential load. When the microgrid is operated in the grid-tied mode, the over-produced energy will be delivered to the bulk grid. However, when the microgrid is in the autonomous operation mode, the over-produced energy will begin to accumulate in the distributed energy storage, and if the overproduction lasts for a long period, the distributed energy storage will be overcharged and the SOC will exceed 1. The predicted SOC will be applied to check whether it is necessary to reduce the energy production from the generation bus. If the predicted SOC is larger than 1, the generation will be mandatorily decreased until the amount of energy absorbed by the distributed energy storage will not cause the over-charging problem. Firstly, the energy production from the wind turbines will be reduced. If necessary, the energy production from the solar panels will be reduced as well. Figure 39 displays a chart-flow for implementing the microgrid topology finalization and operation procedure in the autonomous mode. Once the microgrid topology is finalized, this chart-flow directs the operation procedure in time domain.

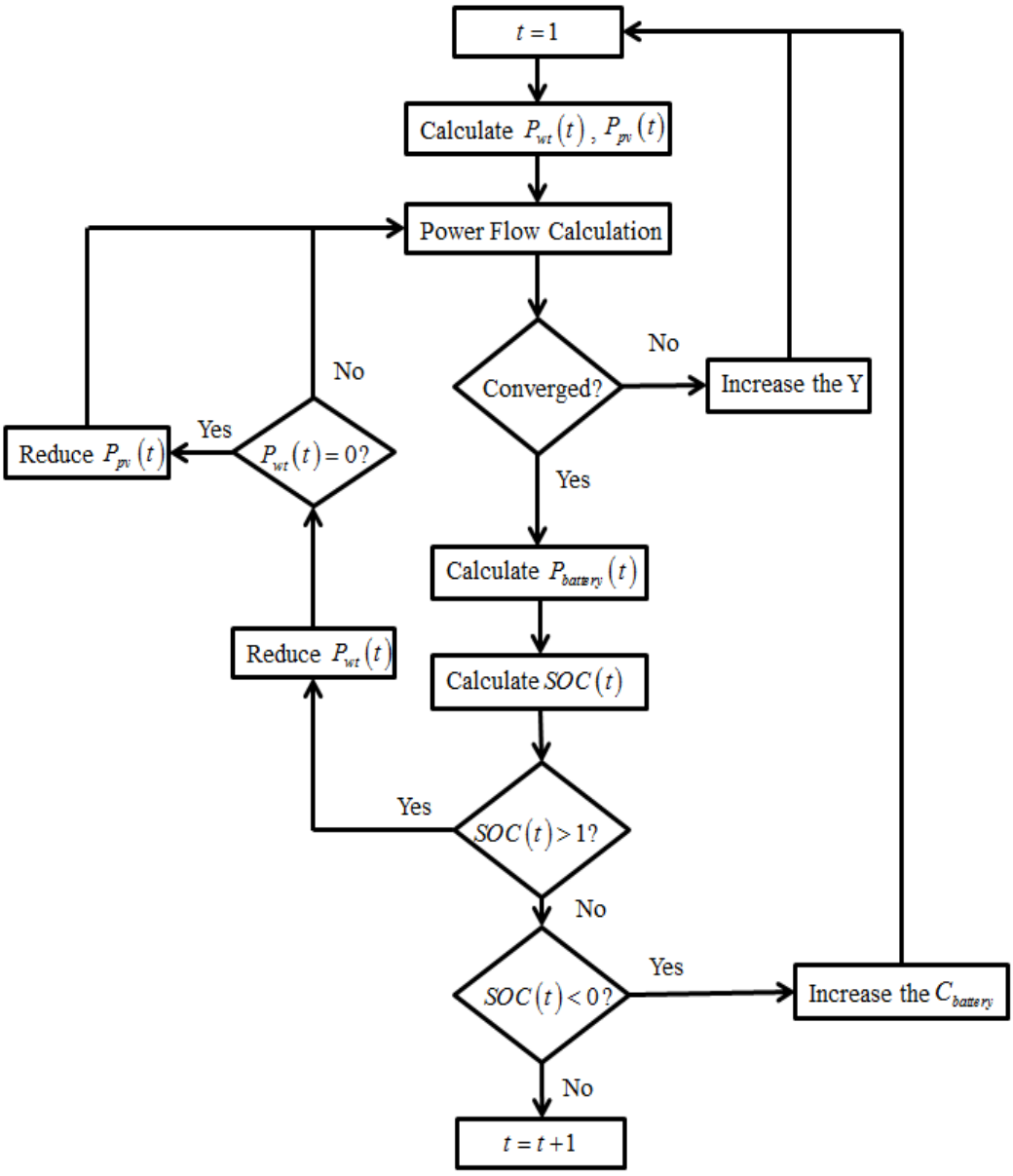

Figure 39. Microgrid topology finalization and autonomous operation scheme in time domain.

CHAPTER 5

Back Propagation Neural Network Based Energy Manager Design

5.1 Back-propagation Neural Network (BPN)

Paul Werbos established the back-propagation algorithm and proposed the concept of hidden layers in his dissertation [54]. This work did not collect the attention in 1970s, but it was revived in the late 1980s. In the mid-1980s, David Rumelhart presented his report about the development of back-propagation algorithm [55]. The proposed bi-directional artificial learning mechanism becomes the most popular learning algorithm for the multilayer perceptron network, and the generalized delta rule becomes the most widely used method to update the weights [56].

5.1.1 Back-propagation network structure BPN stands for the back propagation neural network, which is a type of multi-layer perceptron that applies the back-propagation algorithm for the network training. Figure 40 displays the network structure of a multi-layer perceptron network, which consists of the input layer, the hidden layer, and the output layer. Each layer has its own neurons, or called the process elements. The neurons in the hidden layer and the output layer are fully connected to the neurons in the previous layers. The features of an input sample are mapped into the neurons in the input layer. The outputs of the input neurons associated with the connection weights are activated in the hidden neurons, and yield to the outputs of the hidden neurons. The outputs of the hidden neurons associated with the connection weights are activated in the output neuron, and finally emerged to the output of the network. The number of the hidden neurons is determined based on the testing performances, which means the optimal number of the hidden neurons yields to the minimum testing error.

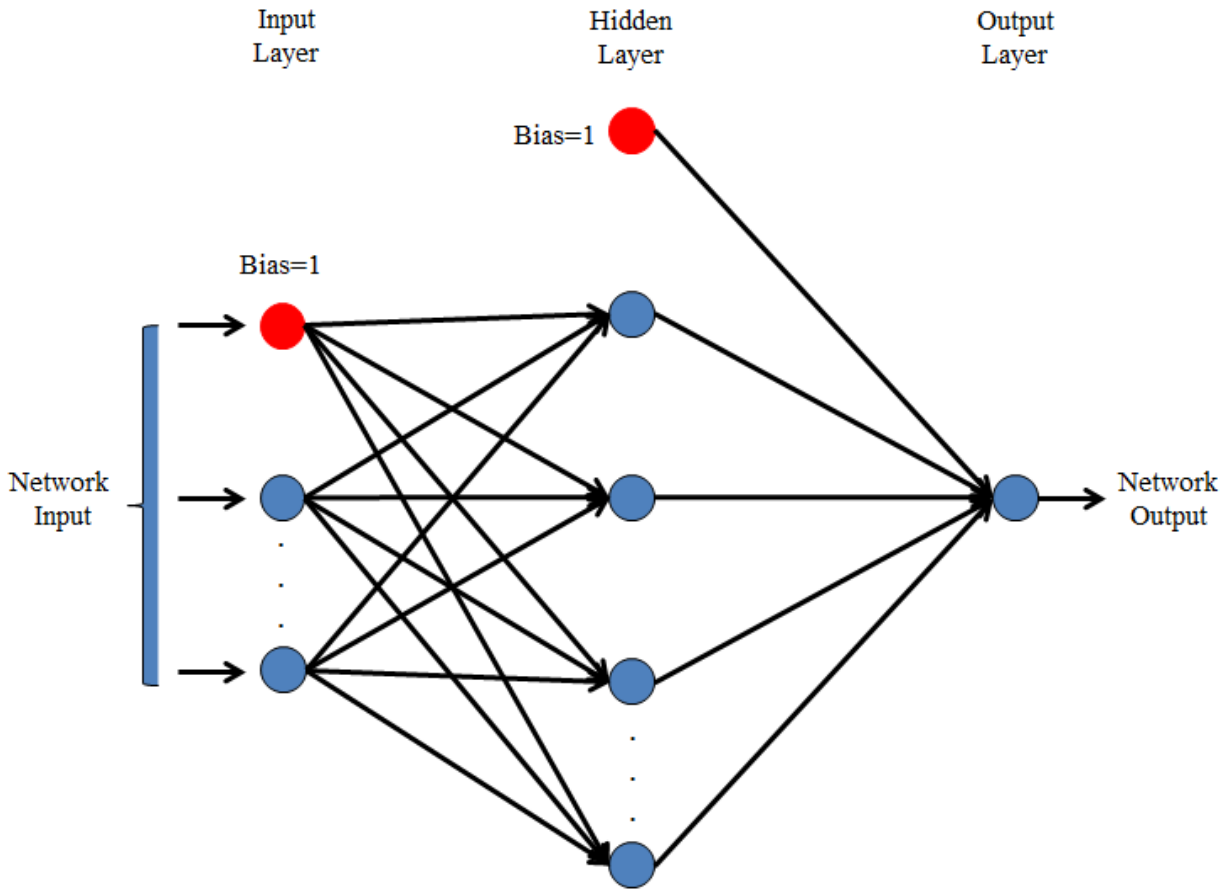

Figure 40. The network structure of a multi-layer perceptron with one hidden layer.

5.1.2 Back-propagation learning algorithm The back-propagation learning algorithm has the bi-directional signal flows, the function signal forward pass and the error signal reverse pass.

5.1.2.1 Function signal forward pass The function signal forward pass is that the input signal passes through the network and emerge to the output signal. For a one hidden layer and one output layer BPN, the n features of a sample are mapped into the input neurons. The output signal vector of the input neurons is:

$$X = [x_0, x_1, x_2, \cdots, x_n]^T \tag{5.1}$$

where x_0 is the bias, and $x_0 \equiv 1$.

The output signal vector X associated with the weight matrix W of the connections between the input layer and hidden layer becomes the input signal vector I of the hidden neurons.

$$W = \begin{bmatrix} w_{0,1} & w_{0,2} & \cdots & w_{0,m} \\ w_{1,1} & w_{1,2} & \cdots & w_{1,m} \\ \vdots & \vdots & \ddots & \vdots \\ w_{n,1} & w_{n,2} & \cdots & w_{n,m} \end{bmatrix} \tag{5.2}$$

where m is the number of hidden neurons.

$$I = W^T X = [I_1, I_2, \cdots I_m]^T \tag{5.3}$$

The input signal vector I of the hidden neurons passes through the hidden neurons via the activation function $T(I)$, and becomes the output signal vector H of the hidden layer.

$$H = T(I) = [h_1, h_2, \cdots h_m]^T \tag{5.4}$$

The graph of activation function $T(I)$ is "S-shaped", so it is also call the sigmoid function. In this research, the log-sigmoid transfer function is applied as the activation function:

$$T(I) = \frac{1}{1 + e^{-\alpha \cdot I}} \tag{5.5}$$

where α is the momentum, which decides the shape of the log-sigmoid transfer function. Figure 41 displays the graph of the log-sigmoid transfer function with $\alpha = 1$.

After add the hidden layer bias $h_0 \equiv 1$ into the hidden neuron output H, the signal vector H becomes:

$$H = [h_0, h_1, h_2, \cdots h_m]^T \tag{5.6}$$

The output signal vector H associated with the weight vector V of the connections between the hidden layer and the output layer becomes the input signal vector J of the output neuron.

$$V = [v_0, v_1, \cdots v_m]^T \tag{5.7}$$

$$J = V^T \cdot H \tag{5.8}$$

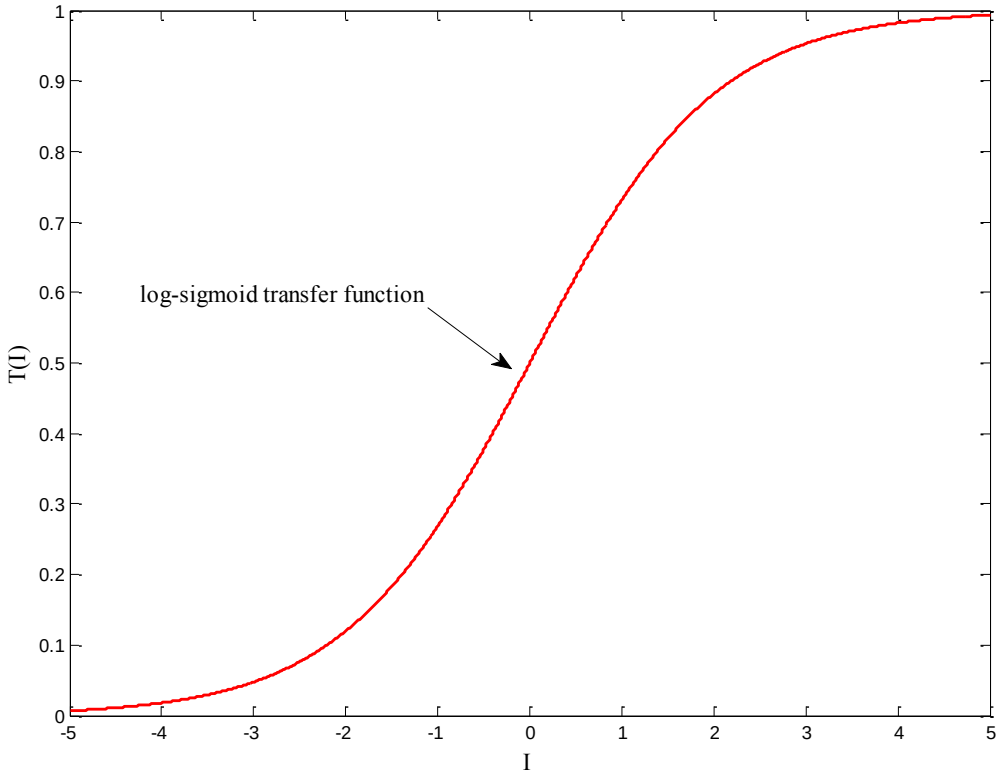

Figure 41. Graph of the log-sigmoid transfer function with $\alpha = 1$.

The input signal vector J of the output neuron passes through the output neuron via the activation function $T(J)$, and becomes the output signal $\hat{y}$ of the network.

$$\hat{y} = T(J) \tag{5.9}$$

5.1.2.2 Error signal reverse pass The network output $\hat{y}$ will compare with the desired output y_d and generate the error signal e as:

$$e = y_d - \hat{y} \tag{5.10}$$

The error signal e back-propagates through the network for adjusting the weight vector V and the weight matrix W.

The error signal energy is defined as:

$$\varepsilon = \frac{1}{2} \cdot e^2 \tag{5.11}$$

The partial derivative of error signal energy respect to the weight vector V is as follows [56]:

$$\frac{d\varepsilon}{dV} = \frac{d\varepsilon}{de} \cdot \frac{de}{d\hat{y}} \cdot \frac{dH}{dJ} \cdot \frac{dJ}{dV} \tag{5.12}$$

After cancel the same terms in the right side of Equation 5.12, the partial derivative of error signal energy respect to the weight vector V is:

$$\frac{d\varepsilon}{dV} = -e \cdot T'(J) \cdot H \tag{5.13}$$

The adjustment of the weight vector V will be:

$$\Delta V = -\beta \cdot \frac{d\varepsilon}{dV} = \beta \cdot \delta_o \cdot H \tag{5.14}$$

where β is the learning rate, which is a positive number and less than 1, and δ_o is called the local gradient of the output layer and defined by:

$$\delta_o = e \cdot T'(J) \tag{5.15}$$

then

$$V_{new} = V_{old} + \Delta V \tag{5.16}$$

To update the weight matrix W, the local gradient of the hidden layer δ_h is identified as:

$$\delta_h = \delta_o \cdot V \cdot T'(I) = \begin{bmatrix} \delta_o \cdot v_1 \cdot T'(I_1) \\ \delta_o \cdot v_2 \cdot T'(I_2) \\ \vdots \\ \delta_o \cdot v_m \cdot T'(I_m) \end{bmatrix} \tag{5.17}$$

The adjustment of the weight matrix W is:

$$\Delta W = \beta \cdot X \cdot \delta_h \tag{5.18}$$

then

$$W_{new} = W_{old} + \Delta W \tag{5.19}$$

5.1.3 Training stopping criteria The back-propagation algorithm was not guaranteed to be converged after the iterative training. To prevent the network over-learning, and improve the generalization ability, the training stopping criteria are formulated as follows:

1. The back-propagation algorithm is considered to have converged when the mean square error of network testing outputs per epoch is sufficiently small.
2. The back-propagation algorithm is considered to have converged when the maximum training epoch is reached.

5.2 Back-propagation Neural Network based Energy Manager Design

In the last chapter, the autonomous operation procedure of the residential microgrid is concluded. Once the system topology is finalized, the predicted state of charge of the distributed energy storage in time domain will be a variable, which depends on the current state of the wind speed, global solar radiation, air temperature, residential load, and the previous state of the state of charge, which can be summarized as:

$$SOC_{n+1} = f\left(V_{n+1}, G_{n+1}, T_{n+1}, SOC_n, P_{L,n+1}\right) \tag{5.20}$$

where V is the wind speed; G is the global solar radiation; T is the air temperature; P_L is the residential active power demand. The BPN structure based on Equation 5.20 is shown in Figure 42.

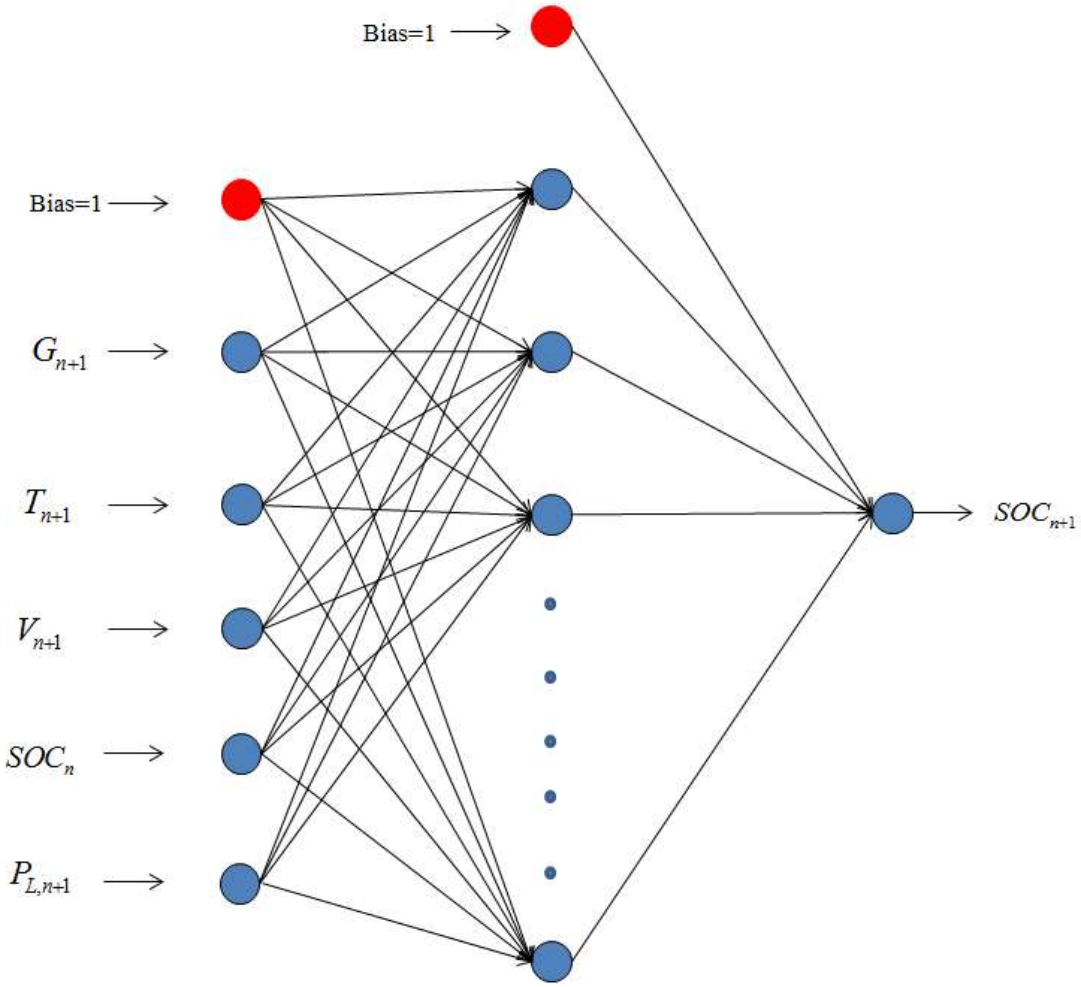

Figure 42. The BPN structure for the SOC prediction.

Before the samples are fed to the input layer, a normalization method is applied to scale the values of inputs and output from 0 to 1 by using Equation 5.21.

$$data_{i,normlized} = \frac{data_i - \min(data)}{\max(data) - \min(data)} \tag{5.21}$$

After the network is trained, the value of network output should be returned to its original scale by:

$$data_i = data_{i,normalized} \cdot \left(\max\left(data\right) - \min\left(data\right)\right) + \min\left(data\right) \tag{5.22}$$

In Figure 42, the number of hidden neurons is not specified. When the network is training, the different number of the hidden neurons will yield to the different network performances. The number of the hidden neurons is finalized according to the network which yields the best testing performance.

Once the predicted SOC is obtained, the distributed generation systems are expected to self-adapt to the predicted SOC by reducing the power output from the generators. The whole procedure is as followings and concluded in Figure 43 as well:

1. Use the wind speed, the globe solar radiation, the air temperature, the real power demand in the current state and the SOC of the energy storage in the previous state to predict the SOC in the current state.
2. Use the wind speed, the globe solar radiation, the air temperature in the current state to calculate the maximum power output at the PV bus.
3. Perform the power flow calculation based on the Gaussian-Seidel method, and obtain the power injection or ejection at the swing bus. Based on the power injection or ejection at the swing bus, the current state SOC is obtained.
4. If the current state SOC is larger than the BPN predicted SOC, the power output from the generation bus should be reduced. First, the power generated by the wind turbines will be reduced. If the power outputs of wind turbines are zero, the power outputs of the solar panels should be reduced as well.

5. Repeat the steps 3 and 4 until the difference of the calculated SOC and the predicted SOC in the current state is sufficiently small.
6. Record the adjusted wind turbines outputs and the solar panels power outputs, and calculate the blade pitch angle and the solar panel terminal voltage based on the adjust power outputs.

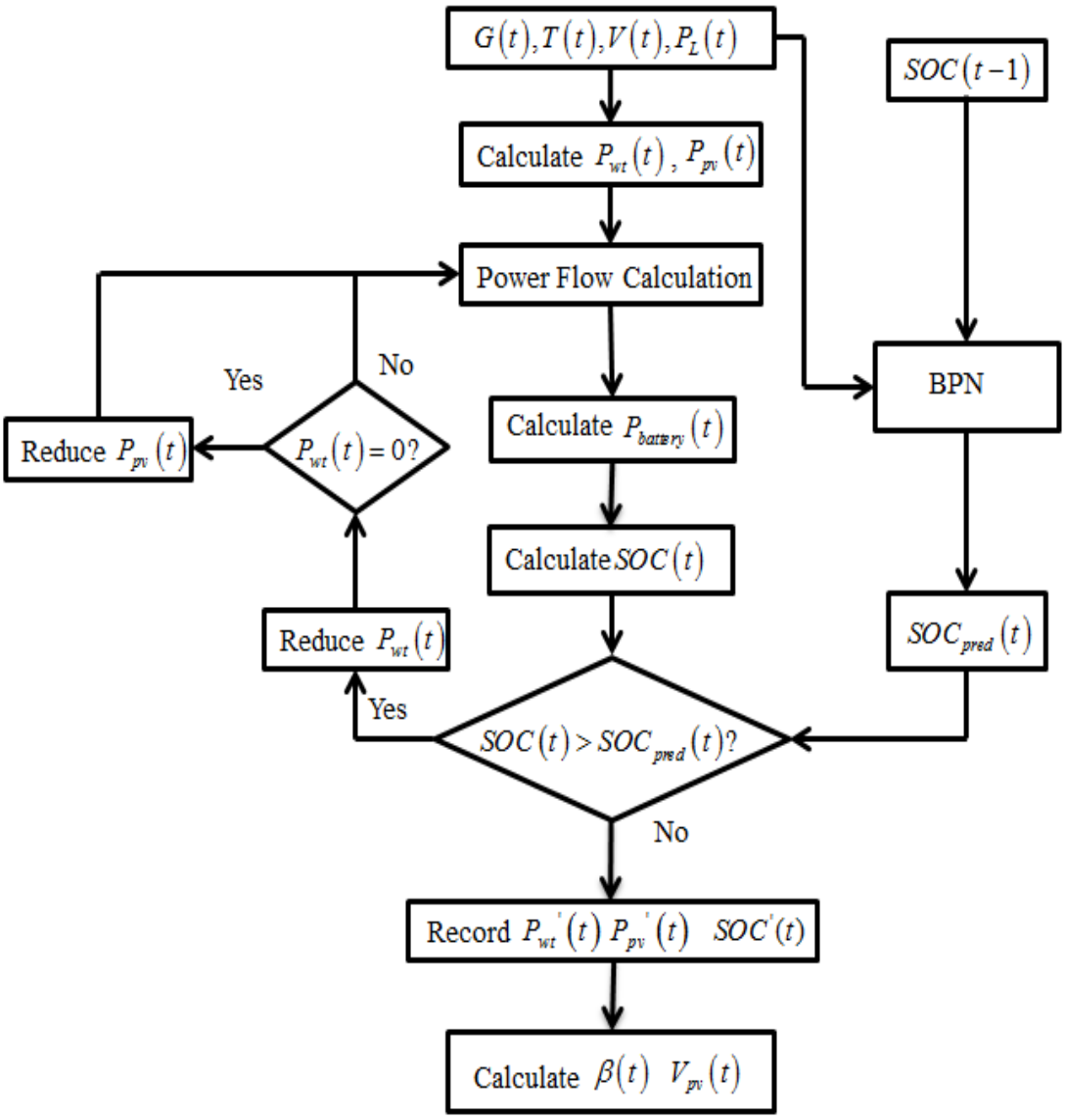

Figure 43. The BPN based energy manager operation scheme.

CHAPTER 6

Experimental Case Study

6.1 Introduction

The research residential microgrid is assumed to support 1000 households in the East Arizona. The original residential load data is the hourly load data in the far west area of Texas, which is downloaded from the Electric Reliability Council of Texas. The data ranges from April 20th 2011 to April 20th 2013 [57]. According to the records from the U.S. Energy Information Administration, the average hourly power demand for a household in Arizona is 1.486 kW in 2011 [58]. The load data will be rescaled to an average hourly load demand 1486 kW with a power factor 0.85 and the linear growth will be neglected. The climate data is downloaded from the measurement and instrumentation date center, National Renewable Energy Laboratory. The station is located in the southwest solar research park, Phoenix, Arizona, and the data set is composed of the hourly global solar radiation, the wind speed, and the air temperature, which range from April 20th 2011 to April 20th 2013 [59].

6.2 Optimal Sizing of Renewable Distributed Generators at Study Area

Figure 44 displays the average hourly wind speeds at 11 meter high in 12 months at the case study area by using the Weibull probability model. The measured hourly no-calm wind speed samples in 12 months are classified into 25 classes, and represented by the central value of each class. After calculate the cumulative probabilities of the different hourly non-calm wind speed classes in a month, the shape parameter c and the scale parameter k of the hourly wind speed Weibull probability model in a particular month are solved. Table 3 lists the shape parameter c and scale parameter k of the Weibull probability model of each month.

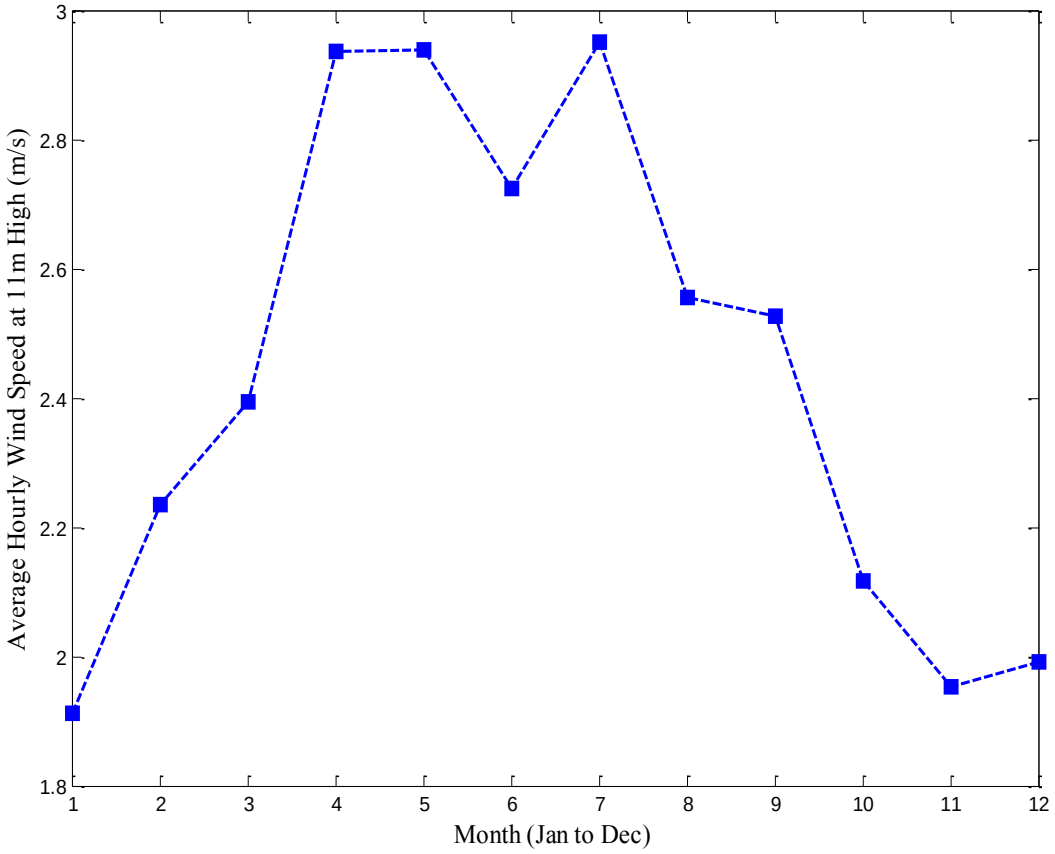

Figure 44. Average hourly wind speed at 11meter high in 12 months.

Table 3

Shape Parameter c and Scale Parameter k of the Weibull Probability Models in 12 Months

	Jan	Feb	Mar	Apr	May	Jun	Jul	Aug	Sep	Oct	Nov	Dec
c	2.1	2.5	2.65	3.31	3.31	3.05	3.31	2.86	2.82	2.31	2.13	2.19
k	1.92	1.85	1.94	1.93	2.12	2.27	2.37	2.47	2.21	1.95	1.84	1.93

Figure 45 displayed the average hourly wind power extracted from a wind turbine with 6.5 meter long blades. The air density ρ used in this research is a constant, which is equal to $1.2\,kg\cdot m^{-3}$. When the blade pitch angle β is fixed, an optimal tip speed ratio λ_{opt} will yield to the maximum wind power extraction fraction $C_{p,\max}$. When the blade pitch angle β is

increasing, the equivalent swept area A is decreasing. As a result, wind power extraction fraction C_p is decreasing. In Figure 45, the blade pitch angle $\beta = 0$ and the optimal tip speed ratio λ_{opt} is 7.05. The maximum power factor $C_{p,\max}$ is 0.4412. Because the maximum average hourly power extracted by a wind turbine is 1.8 kW, a rated 2 kW induction generator is capable of transferring the mechanical energy to the electrical energy.

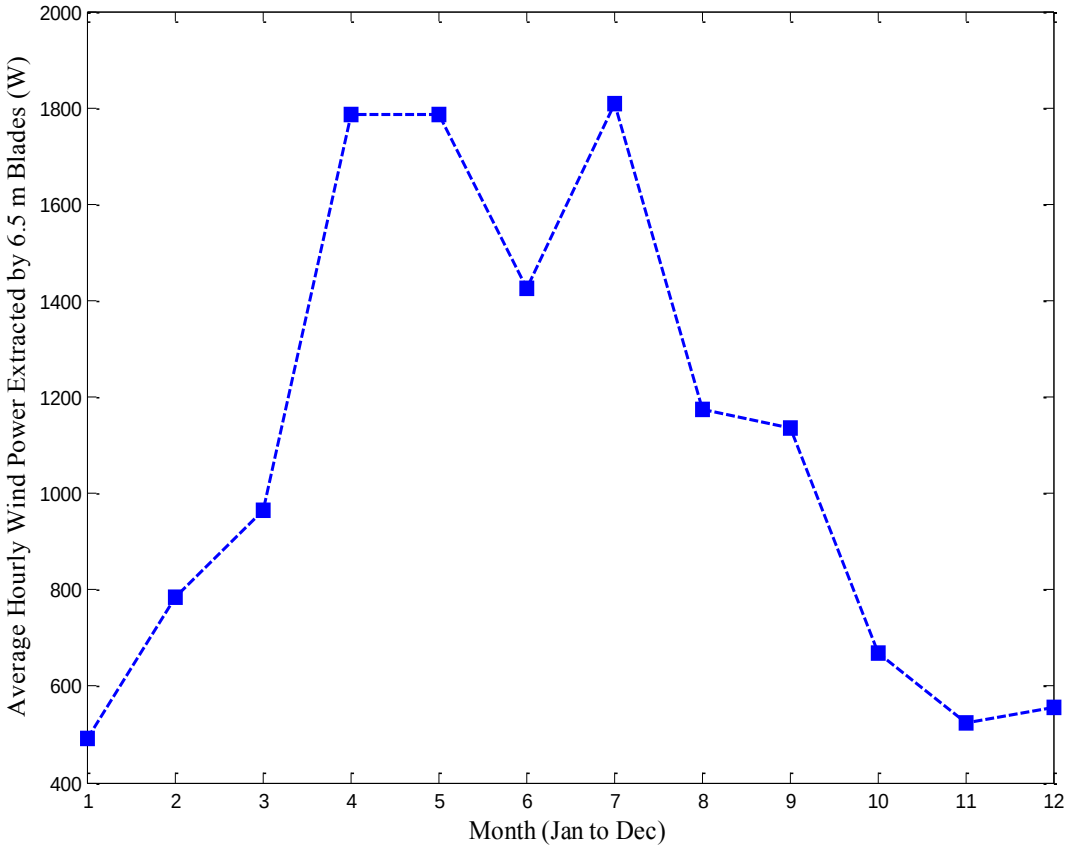

Figure 45. Average hourly wind power extracted by the wind turbine with 6.5 meter long blades in 12 months.

Figure 46 displayed the average hourly global solar radiation in twelve months. The measured hourly global solar radiation samples in 12 months are classified into 25 classes, and represented by the central value of each class. After calculate the probabilities of the different

hourly global solar radiation classes in a month, the expect value will represent the average hourly global solar radiation of that month.

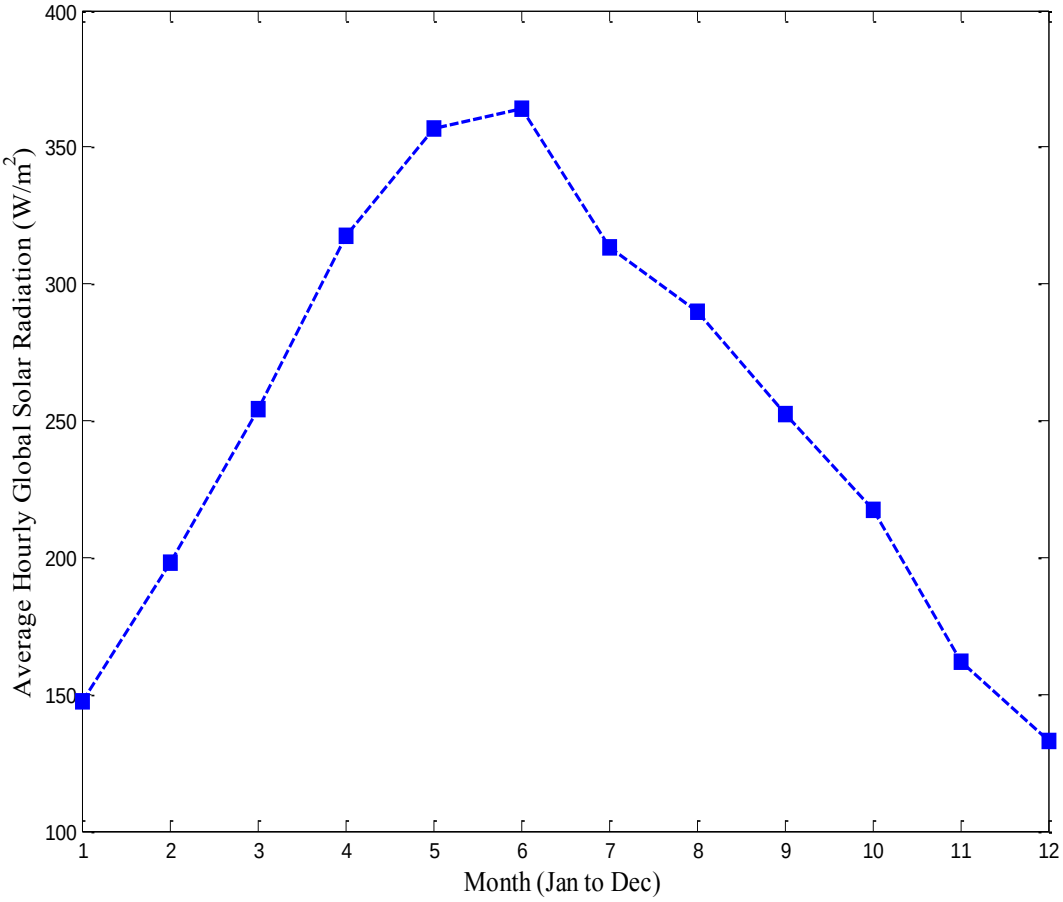

Figure 46. Average hourly global solar radiations in 12 months.

Figure 47 displayed the average hourly air temperature and the cell temperature in twelve months. The measured hourly air temperature samples in 12 months are classified into 25 classes, and represented by the central value of each class. After calculate the probabilities of the different hourly air temperature classes in a month, the expect value will represent the average hourly air temperature of that month. The average hourly cell temperatures in 12 months are calculated based on Equation 2.15. The Normal Operating Cell Temperature (NOCT) used in

this equation is 47.5 C^o, which is found in the manufacture data sheet of the rated 200W solar panel (KC200GT).

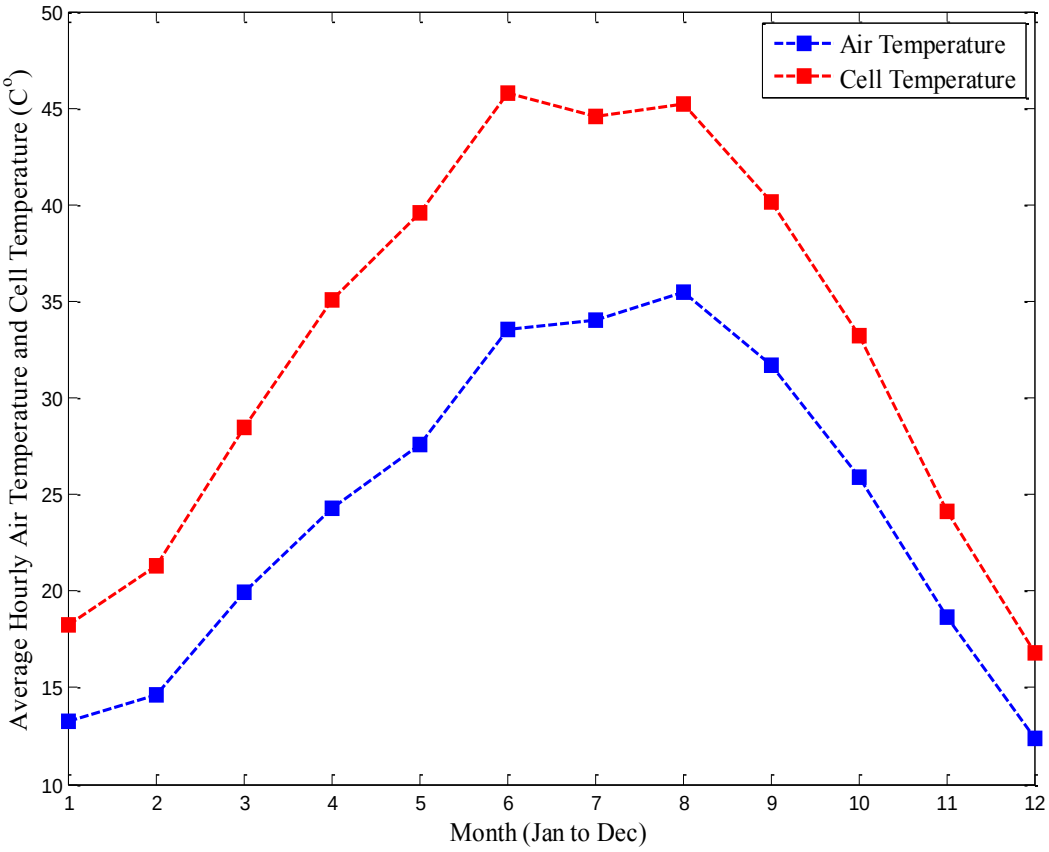

Figure 47. Average hourly air temperatures and cell temperatures in 12 months.

Figure 48 displayed the average hourly power converted by the rated 200W solar panel (KC200GT) in twelve months. The average hourly power converted by the solar panel is calculated by using Equation 2.17. The parameters can be found in the solar panel manufacture data sheet available in the Appendix. The seasonal features are obviously displayed in the figure. The power output from the solar panel reaches its annul peak in the summer, and the power output from the solar panel reaches its annul valley in the winter. This fact exactly describes the globe solar radiation changing in the northern hemisphere.

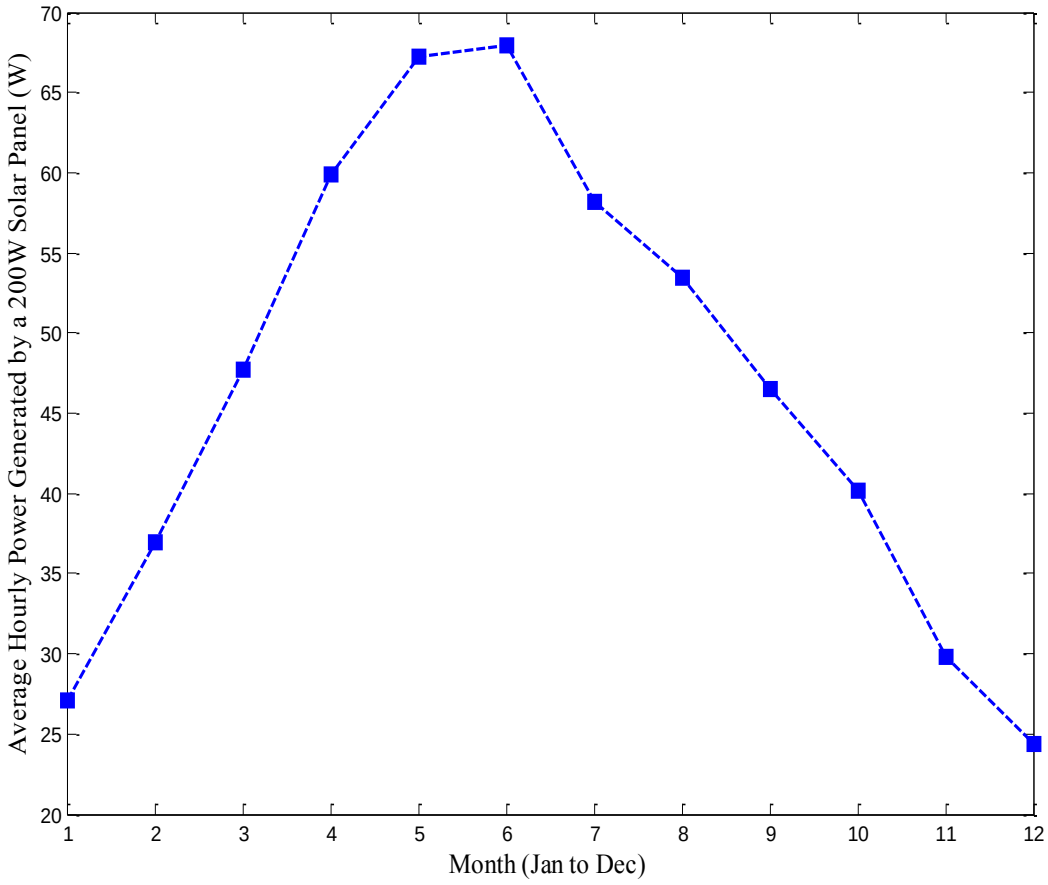

Figure 48. Average hourly power converted by a 200W solar panel (KC200GT).

Figure 49 displays the average hourly residential active power demand from April 2011 to April 2013. The recorded hourly load data is rescaled to meet the actual hourly 1000 household load demands in 2011 in the research area. Assume that the population in the area is fixed, and then the linear load growth component is extracted from the load model. It can be achieved by setting the coefficient of the linear growth equal to 1, $b_1 = 1$. The highest order of harmonic is the fourth harmonic, which is decided by whether the additional harmonics will improve the model performance significantly. Table 4 lists the coefficients of the residential load components. b_0 is the coefficient of the base load, b_1 is the linear growth rate, b_2 and b_3

are the coefficients of the fundamental components, b_4 and b_5 are the coefficients of the second order harmonic components, b_6 and b_7 are the coefficients of the third order harmonic components, and b_8 and b_9 are the coefficients of the fourth order harmonic components.

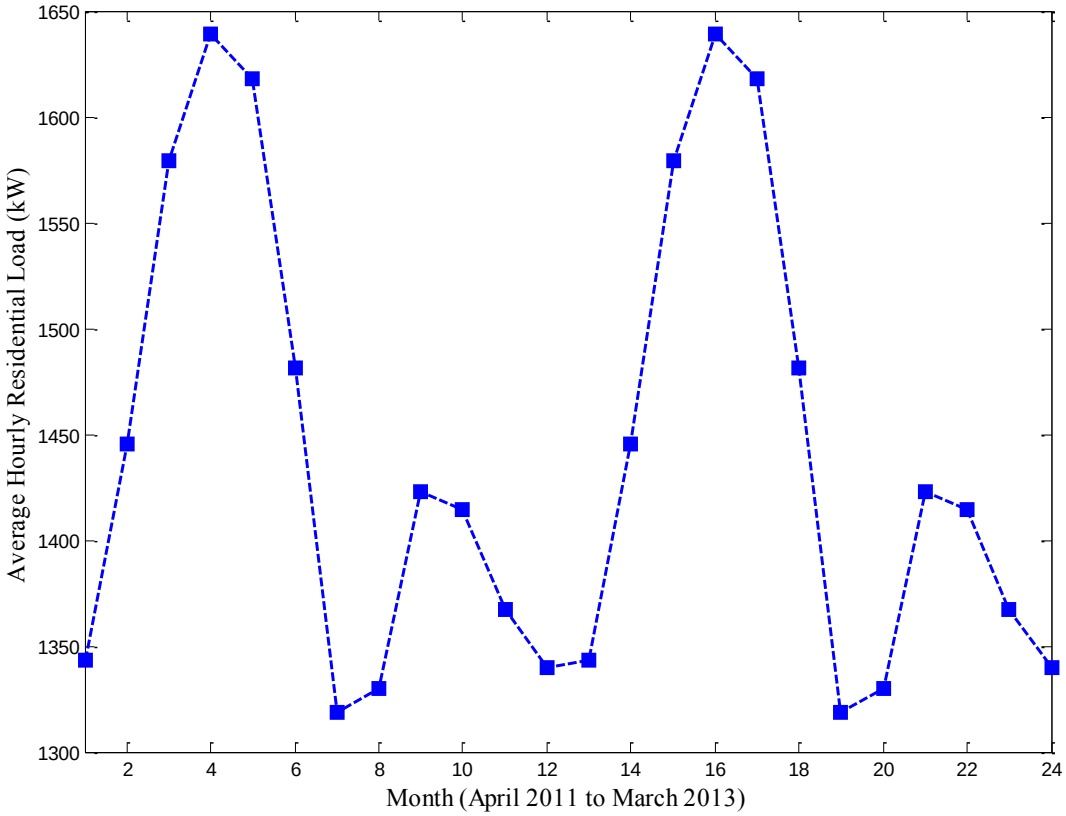

Figure 49. Average hourly residential load from April 2011 to April 2013.

Table 4

Coefficients of the Residential Load Components by using the Fourier Series Decomposition

b0	b1	b2	b3	b4	b5	b6	b7	b8	b9
1436.8	4.86	-65.38	98.1	-45.23	-86.75	-5.37	19.91	14.3	-6.46

After the average hourly wind speeds, the global solar radiations, the cell temperatures, and the residential active loads in 12 months are obtained, the non-uniform simulated annealing

is applied to find the optimal combination of the distributed renewable generators. The costs of each distributed generator are shown in Table 5 [58]. The optimal combination of the renewable distributed generators and the first year cost are shown in Table 6.

Table 5

Installation Cost, O&M Cost of Wind and Solar Power Conversion Systems

	Installation Cost ($/kW)	O&M ($/kW/Yr)
Wind	1938-3468	12-32
Solar	1750-2475	10-25

Table 6

Optimal Combination of Distributed Renewable Generators and the First Year Cost

# of 2kW Wind Power System	# of 200W Solar Panel System	First Year Cost
172	2355	$101,648

Figure 50 displays the cooling schedule of the non-uniform simulated annealing applied for the optimal sizing. At early stages, the high temperature excites the particles with the high energy states, and a worse solution has higher probability to be accepted. When the temperature is lower, the particles trend to cool down and transfer to the relatively frozen stages. Table 7 listed the parameters and the initial state of the non-uniform simulated annealing.

Table 7

Parameters and Initial States of the Non-uniform Simulated Annealing

Initial Temperature (K)	10^7
Temperature Cooling Down Factor	0.99
Maximum Number of Epochs	10000
Parameter of the Degree of Non-uniformity	1
Boltzmann Constant (J/K)	1.38×10^{-23}

When the temperature dropped to 7.857×10^{7} K, the algorithm accepted a worse solution, and the energy (cost) increased to 1.042×10^{5}. This fact represented the hill-climbing feature, which allow the global minimum searching avoid being trapped in the local minimum. When the temperature reached 5.472×10^{7} K, the maximum epoch number is reached and the iterative procedure stopped, which yields the minimum energy (cost) =$101,648.

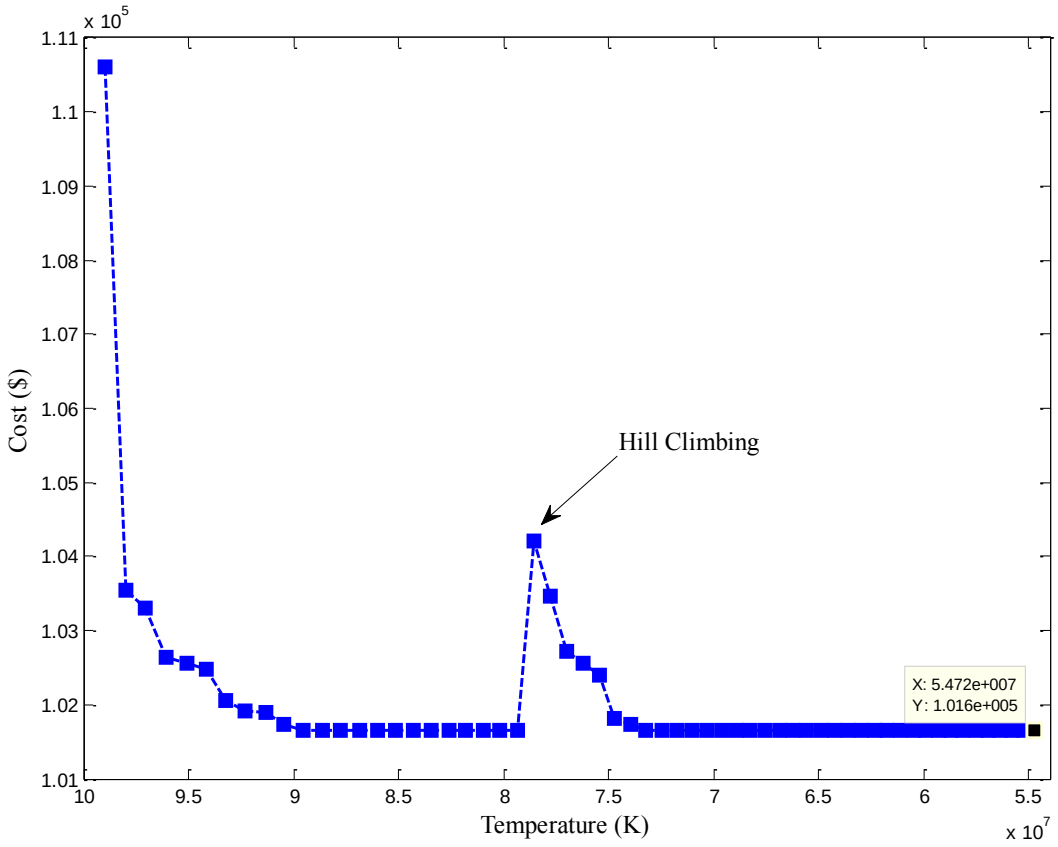

Figure 50. The cooling schedule of the non-uniform simulated annealing.

Figure 51 displays the distances between two adjacent solutions. The new solutions are uniform-randomly generated at the early stages and non-uniform-randomly generated at later stages. It is clear that the distances trend to decrease, which indicates the new solutions are generated near the previous solutions at the later stages. It is the advantage of using the non-

uniform mutation function to generate the new solutions, which denies the long jumps between two adjacent solutions at the later stages.

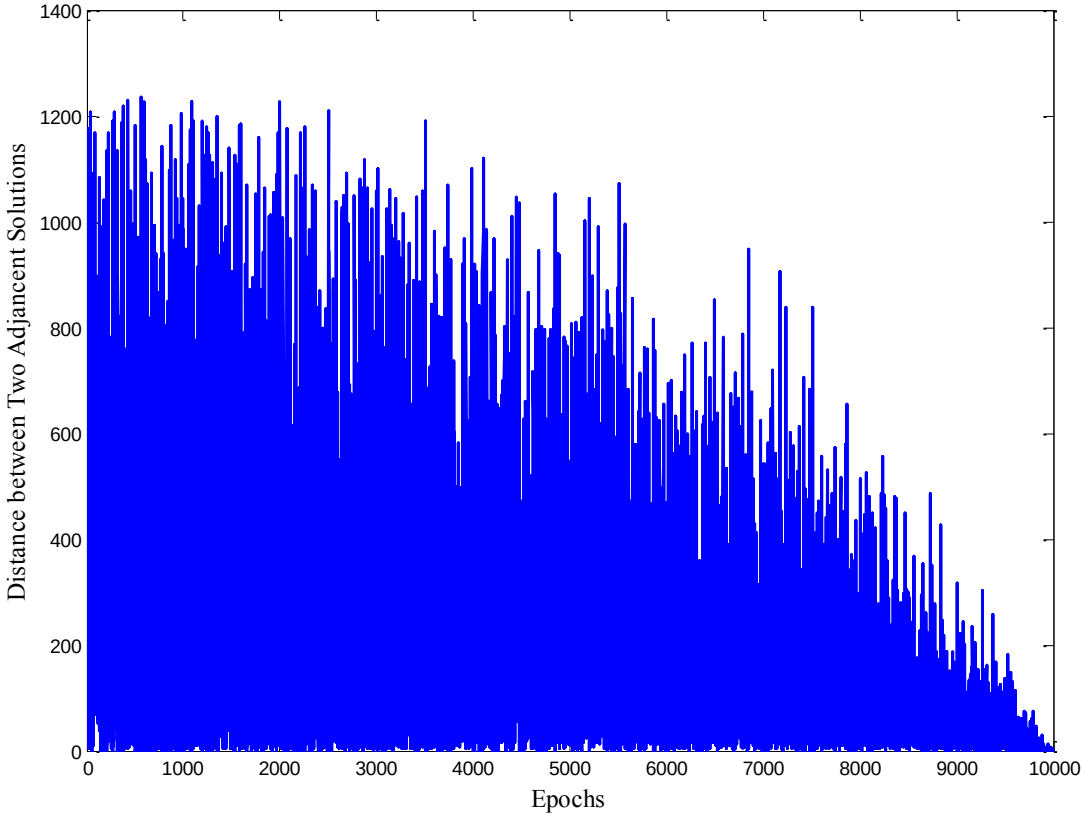

Figure 51. Distances between two adjacent solutions in the optimization process by using non-uniform simulated annealing.

6.3 Microgrid Finalization and BPN Based Energy Manager Operation in Grid-off Mode

6.3.1 Microgrid parameters finalization The optimal combination of distributed renewable generators obtained in the last section. The other two microgrid parameters will be finalized in this section. The first unknown parameter is the impedance of the transmission lines in the microgrid. In order to ensure the power flow converged under various microgrid operation conditions, it is mandatory to identify the maximum impedance of the transmission lines by

applying the procedure displayed in Figure 39. During the power flow calculation, if the voltage vector of any bus is not converged, it is required to reduce the impedance of the transmission line until the power flow calculation converges again. The second unknown parameter is the minimum size of the distributed energy storage. In some season, the wind and solar energy are in their annul valleys and the residential load remains high (winter). If the capacity of the distributed energy storage is low, it cannot deliver the sufficient power to the end users. As a result, the reliability of the power supplement will be critically threatened, and the end users will face the power outages frequently during that season. The state of charge (SOC) represents the amount of energy saved in the distributed energy storage. If the SOC is negative, which means the energy saved in the battery bank is over drawn. Another battery cell connected in parallel is needed to increase the capacity of the battery system. Keep increasing the capacity of the battery bank until the SOC returns to a positive value. Table 8 listed the initial impedance of transmission line, the initial capacity of distributed energy storage, the finalized impedance of transmission line, and the finalized capacity of distributed energy storage.

Table 8

Initial Impedance of Transmission Line, Initial Capacity of Distributed Energy Storage, Finalized Impedance of Transmission Line, and Finalized Capacity of Distributed Energy Storage

	Impedance of Transmission Line	Capacity of the Energy Storage
Initial Value	0.103+0.525j Ω	1562.5 Ah
Finalized Value	0.0103+0.0525jΩ	1250000 Ah

Once the microgrid topology is determined, the procedure listed in Figure 39 is able to implement without the system reset. The time series simulation of the microgrid in the

autonomous mode will be performed based on the meteorological data and the residential load, and the state of charge will be recorded.

Figure 52 displayed the average hourly state of charge of the distributed energy storage system in the weekly time domain. The State of Charge is always between 0 and 1, which means the energy storage system is never over charged or over drawn in the autonomous mode.

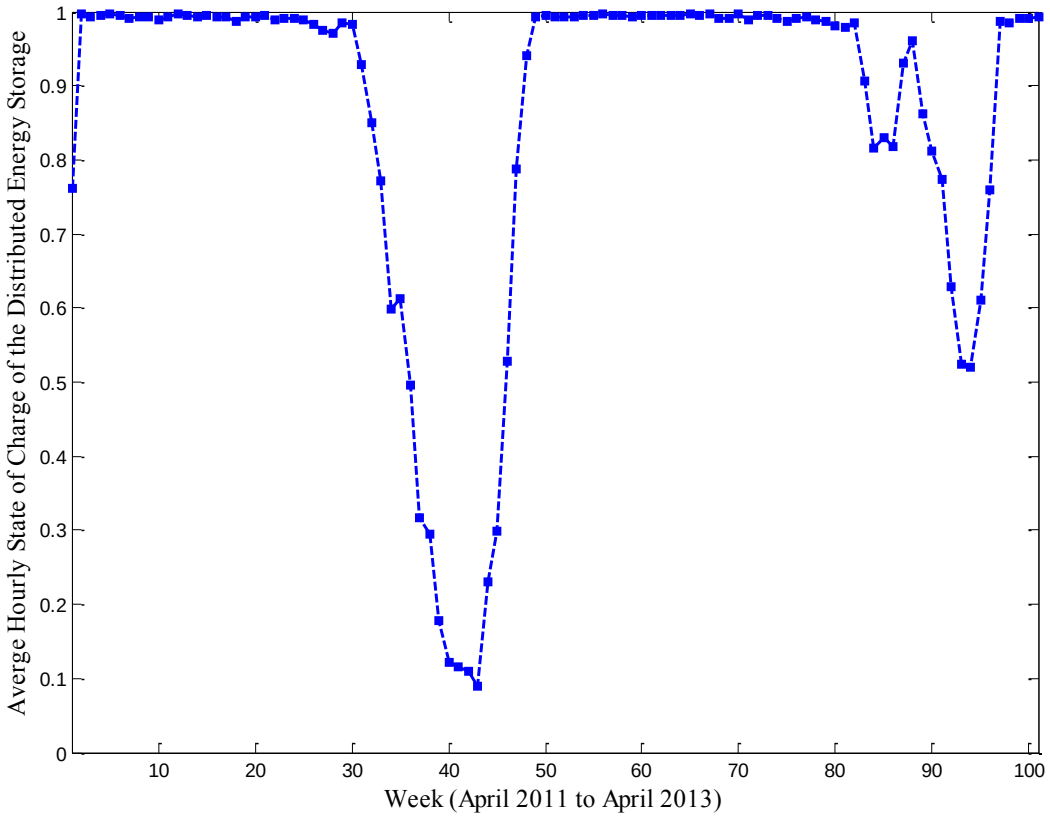

Figure 52. Average hourly state of charge of the distributed energy storage system in the weekly time domain from April 2011 to April 2013.

6.3.2 BPN based energy manager implementation in the autonomous mode The BPN based energy manager is constructed based on Equation 5.20. It is aim to learn the underlying relationship between the previous state of the SOC, the current state of the meteorological information, the current residential active load (inputs) and the current state of the SOC (output).

There are 17088 samples available from April 20th 2011 to April 20th 2013. The first 8327 samples are used to identify the BPN weights. First of all, these 8327 samples are randomized for avoiding the BPN learning the information related to the order of samples. Then the first 75% of the randomized samples are selected as the training samples and the rest 25% are selected as the testing samples.

After each training epoch, the testing samples pass through the network for checking the testing performance evaluated by the mean square error. If the testing mean square error is sufficient small, or the maximum number of the training epoch is reached, the BPN training procedure is finished. For verifying the best network structure, 10 networks with the different numbers of the hidden neurons are tested. Figure 53 displayed the testing performances of the different networks.

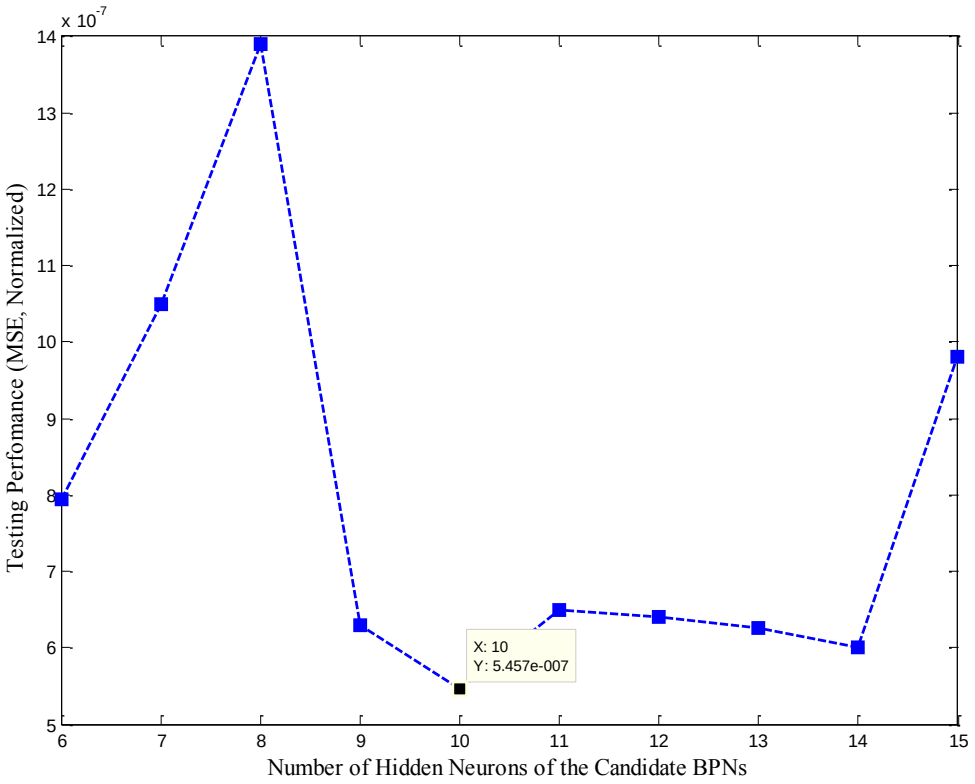

Figure 53. Testing performances of the BPNs with different number of hidden neurons.

The BPN with 10 hidden neurons returns the best testing performance, whose normalized testing mean square error is 5.457×10^{-7}. All the initial weights are randomly selected from 0 to 1, and the other BPN parameters are identical and listed in Table 9.

Table 9

BPN Parameters

Learning Rate	0.25
Maximum number of Epochs	1000
Activation Function	Log-sig

Figure 54 displays the testing elbow curve of the BPN with 10 hidden neurons, which is decreasing fast in the early stages of the iterative learning process.

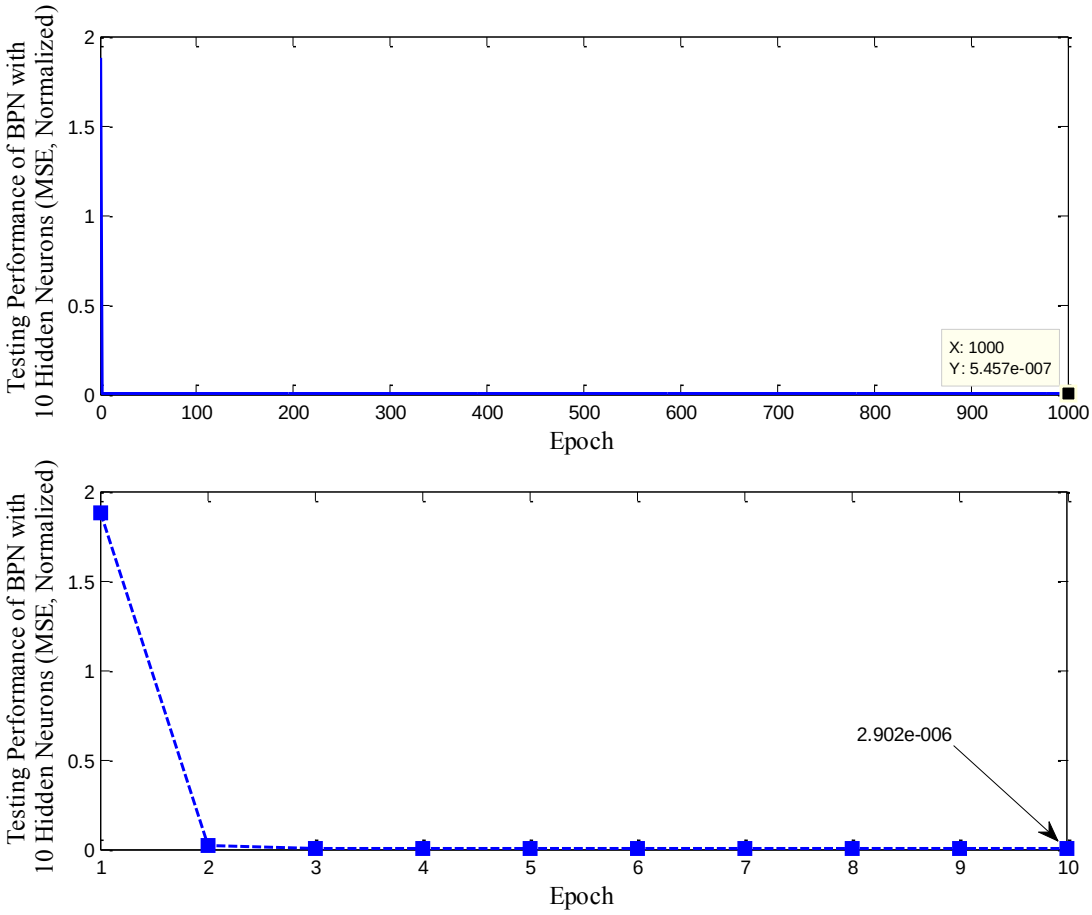

Figure 54. Testing elbow curve of the BPN with 10 hidden neurons.

The upper graph displays the elbow curve in 1000 epochs. The minimum normalized testing MSE occurs at the 1000th training epoch, which is equal to 5.457×10^{-7}. The lower graph displays the elbow curve in the first 10 epochs. At the 10th training epoch, the normalized testing mean square error has already dropped to 2.902×10^{-6}.

Figure 55 displayed the predicted and the desired state of charge of the energy storage system.

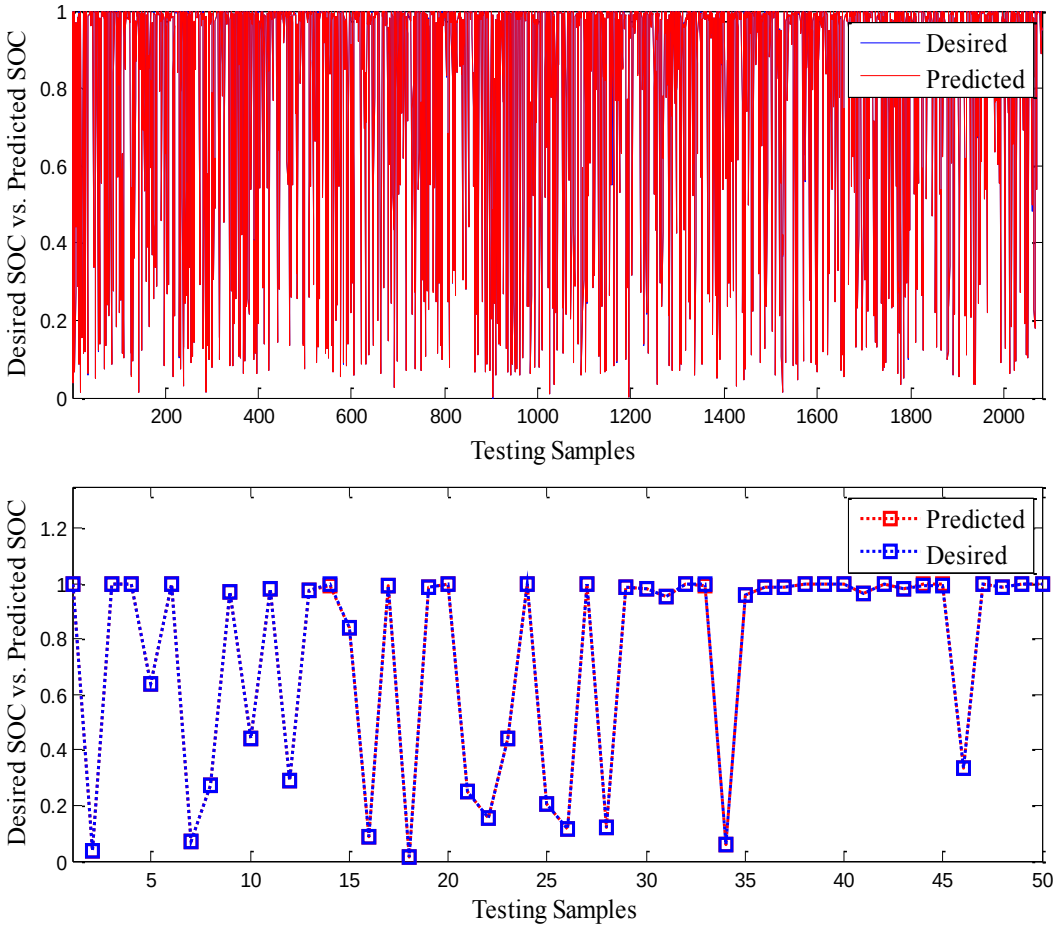

Figure 55. Predicted and desired state of charge of the energy storage system.

The upper graph shows the predicted and the desired hourly SOCs of all the testing samples, and the largest error occurs at the 2060th sample, which is equal to 0.0166. The lower graph shows the predicted and the desired SOCs of the first 50testing samples.

Figure 56 displays the prediction performance of the BPN with 10 hidden neurons. The red curve is the predicted values of the hourly SOC from the 8328th hour to the 17077th hour, the blue curve is the target values of the hourly SOC from the 8328th hour to the 17077th hour, and the black curve is the differences between the predicted values and the target values of the hourly SOC from the 8328th hour to the 17077th hour. The largest error occurs at the 14610th hour, which is equal to 0.0113. The MSE of the testing performance is 5.563×10^{-7}.

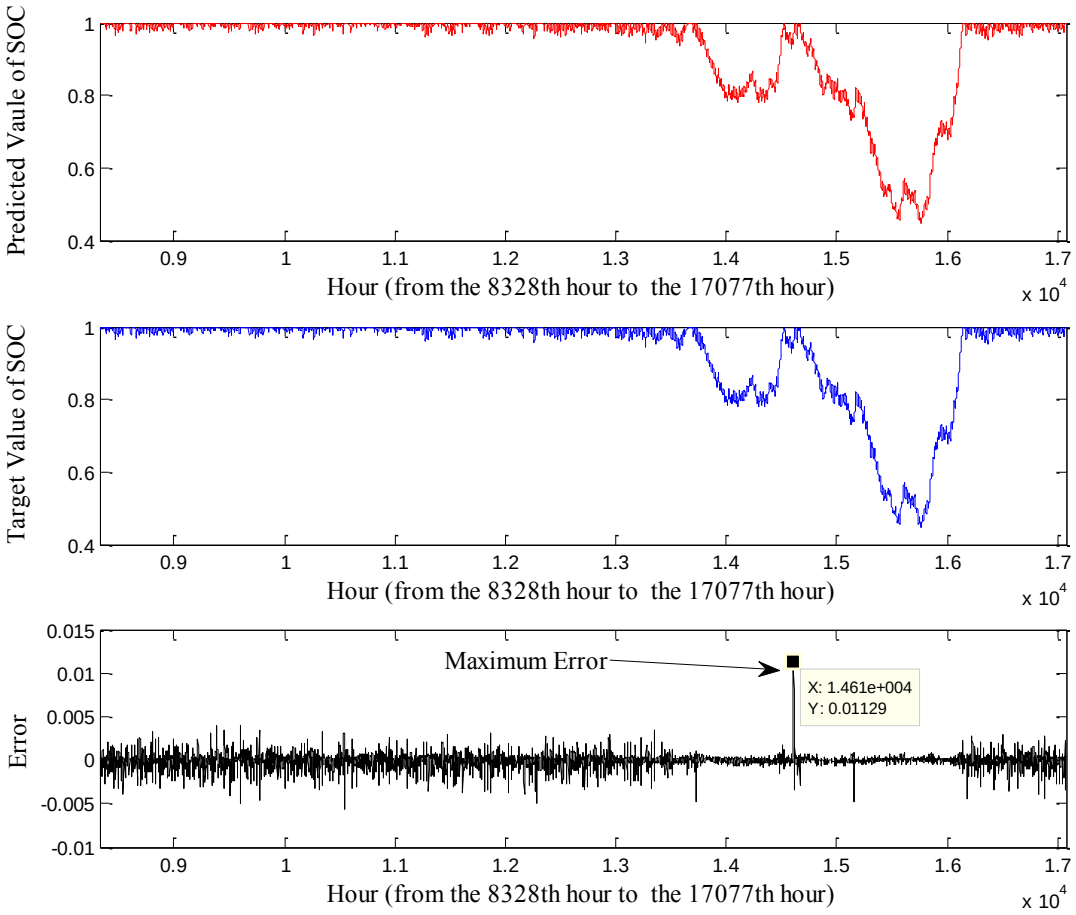

Figure 56. Next year SOC prediction performance of the BPN with 10 hidden neurons using 6245 training samples.

Figure 6.57 displays the testing performance of the BPN with 10 hidden neurons. Compared with the previous BPN with 10 hidden neurons, the new BPN with 10 hidden neurons used all of the first 8327 samples for network training, and other parameters remains. The red

curve is the predicted values of the hourly SOC from the 8328th hour to the 17077th hour, the blue curve is the target values of the hourly SOC from the 8328th hour to the 17077th hour, and the black curve is the differences between the predicted values and the target values of the hourly SOC from the 8328th hour to the 17077th hour. The largest error occurs at the 10550th hour, which is equal to 0.006815. The MSE of the testing performance is 4.882×10^{-7}. It is essentially that the online training scheme can effectively improve the BPN predicting performance.

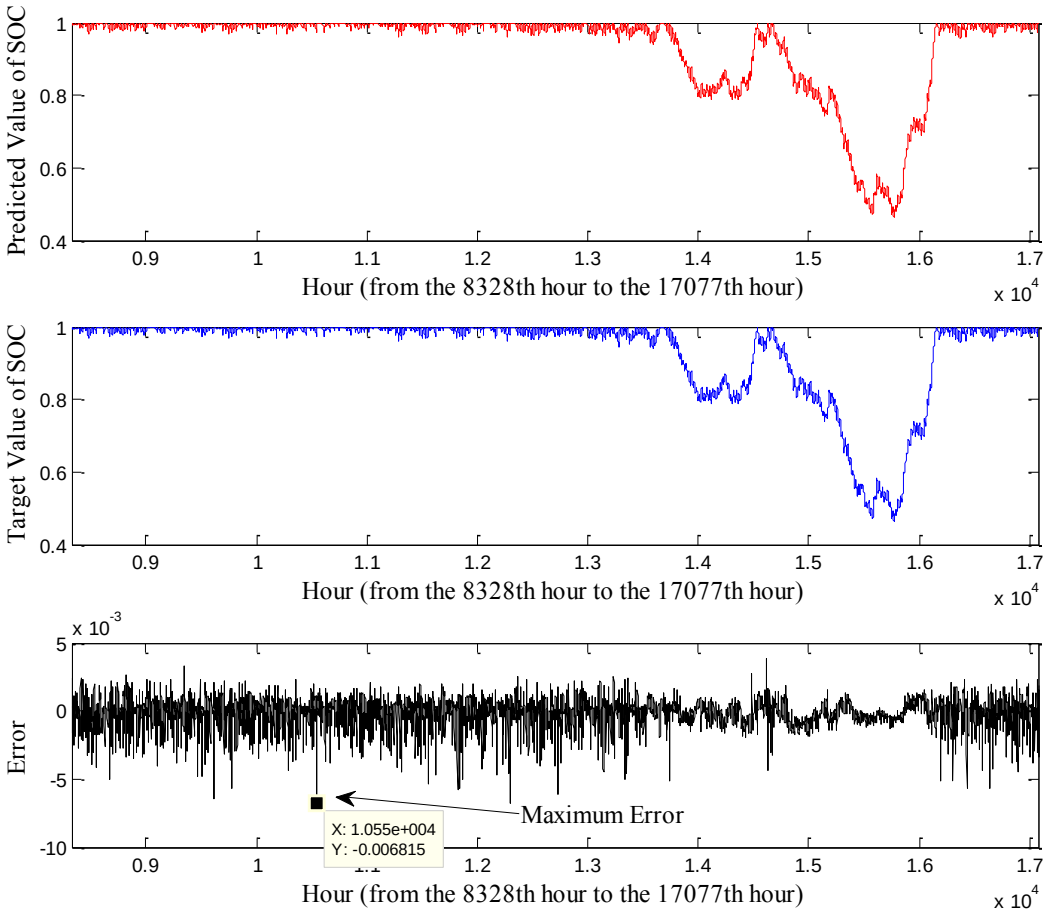

Figure 57. Next year SOC prediction performance of the BPN with 10 hidden neurons using 8327 training samples.

Figure 58 displays the response of the distributed energy storage, when the BPN based energy manager predicted the next stage of the SOC. Due to the system nature and the prediction error, the distributed energy storage did not response as same as the BPN based

energy manager predicted. Once the BPN based energy manager predicts the next stage SOC, the renewable distributed generators should self-adjust the power outputs to ensure the SOC of the energy storage will be leaded by the predicted SOC based on the procedure described in Figure 43. The maximum error occurs at the 11520^{th} hour, which is equal to 0.021. The mean square error of the energy manager predicted SOC is 7.65×10^{-6}.

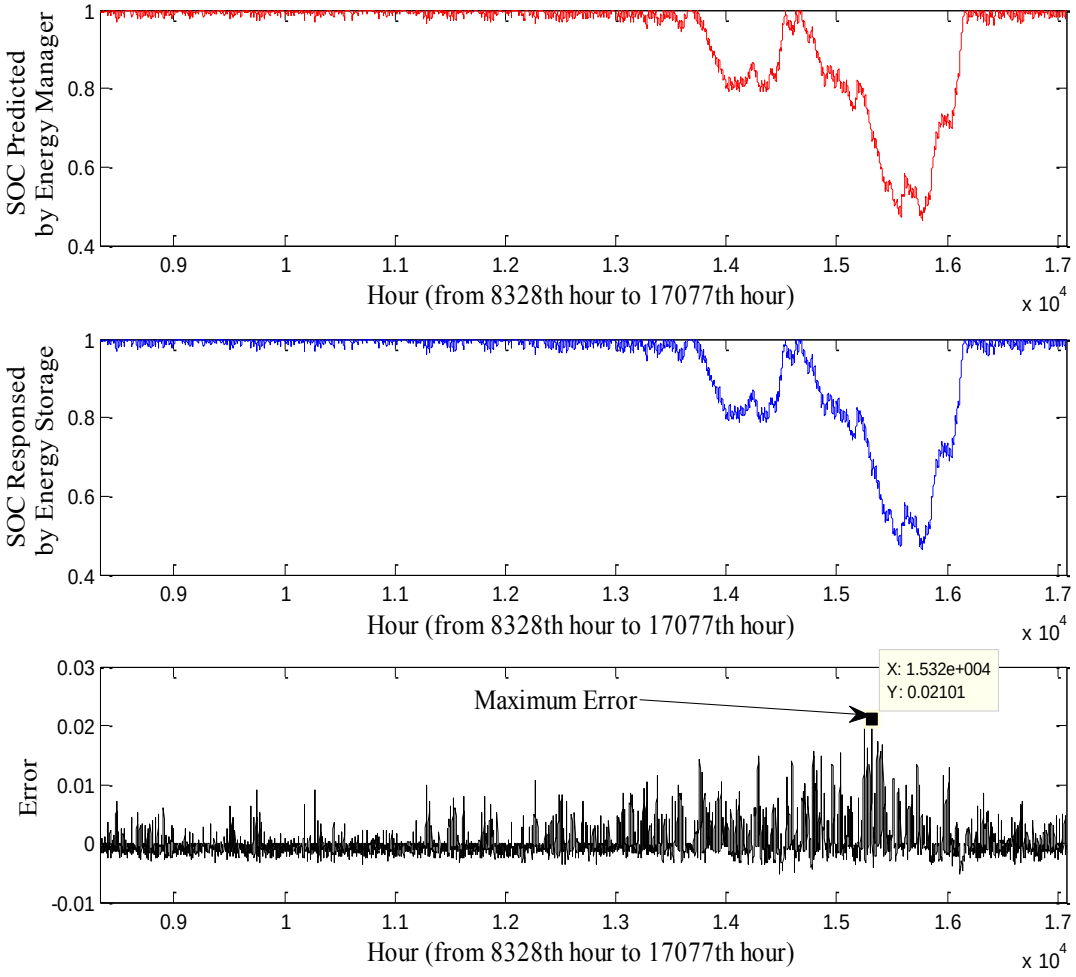

Figure 58. Real-time distributed energy storage SOC response.

Figure 59 displayed the power outputs from the solar panels. The blue curve is the maximum power outputs that the solar panels are able to generate under the real time metrological condition. The red curve is the adjusted power outputs that allow the real time SOC of the distributed energy storage follow the energy manager predicted SOC. There is a valley

occurred from the 13000th hour to the 16000th hour approximately, which is the winter season of the second year.

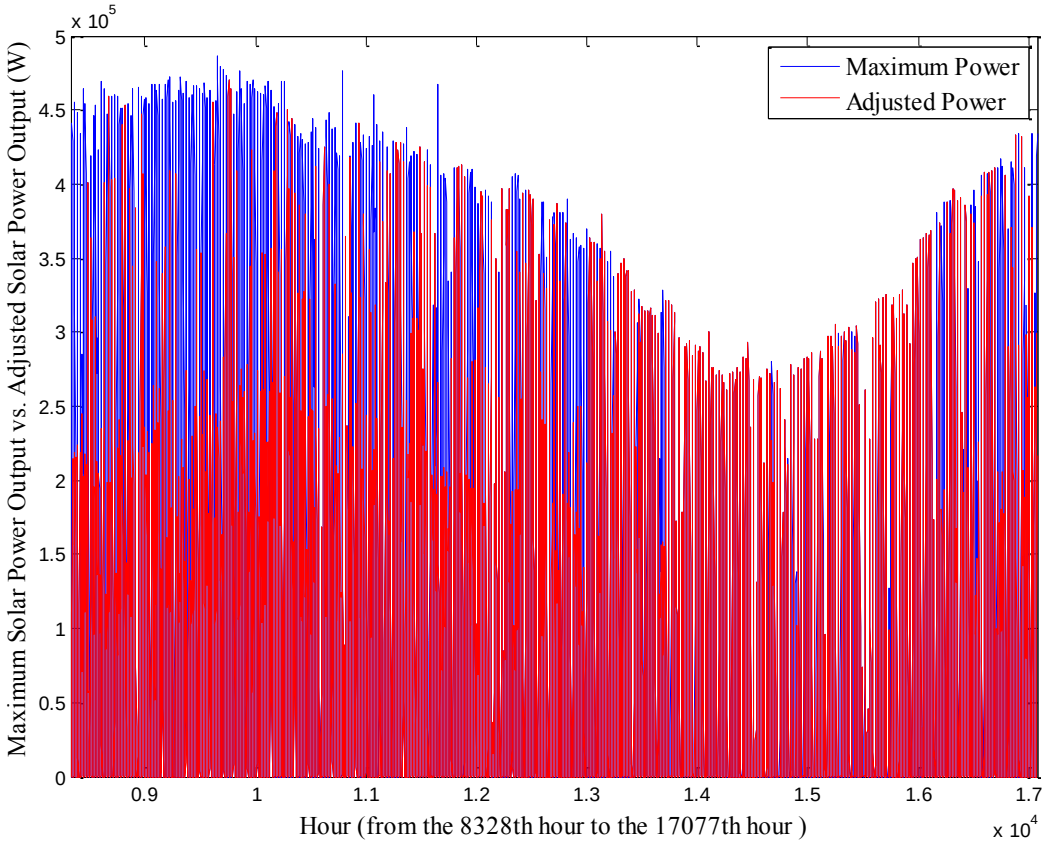

Figure 59. Real-time PV maximum power output and adjusted power output.

Figure 60 displays the terminal voltages applied to the 200W solar panels, which yields to the adjusted solar panel power outputs as shown in Figure 59. The upper sub figure displays the adjusted terminal voltages from the 8328th hour to the 17077th hour, and the lower sub figure is a snap shot of the upper figure, which is from the 8328th hour to the 8375th hour (48 hours, 2 days). In the night time, the terminal voltages drop to zero, because the global solar radiations are zero, and no photon current can be inspired in the solar cells. In the day time, the terminal voltages raise up with the increasing of the global solar radiation based on the desired adjusted power outputs.

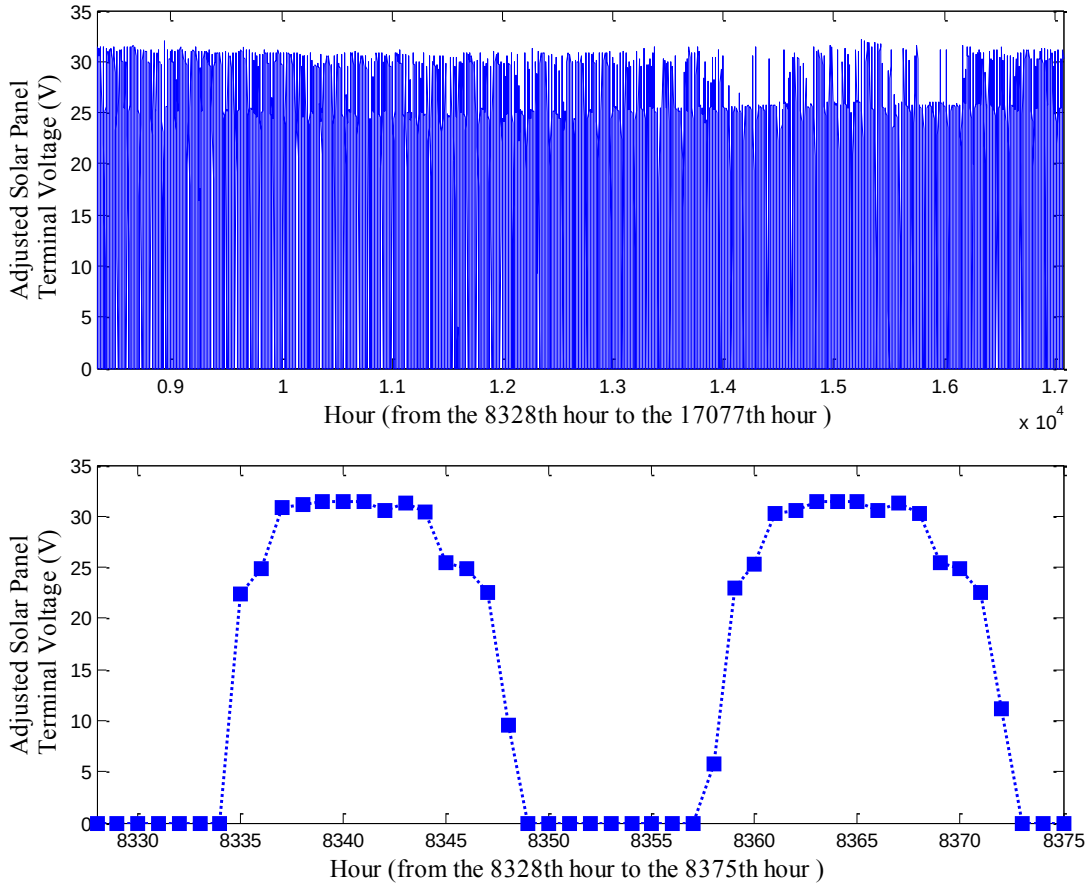

Figure 60. Real-time adjusted solar panel terminal voltages.

Similarly, the power outputs from the wind energy system will be adjusted to meet the revised power outputs, which yields to the SOC of the distributed energy storage following the SOC predicted by the BPN based energy manager.

Figure 61 displays the power outputs from the wind energy systems from the 8328th hour to the 17077th hour. The blue curve is the maximum power outputs that the wind power conversion systems are able to generate under the real time metrological conditions, and the red curve is the adjusted power outputs that allow the real time SOC of distributed energy storage follow the energy manager predicted SOC. In some hours, the values of blue curve are larger than that of the red curve, which avoids the distributed energy storage be overcharged by the power outputs from the generation bus.

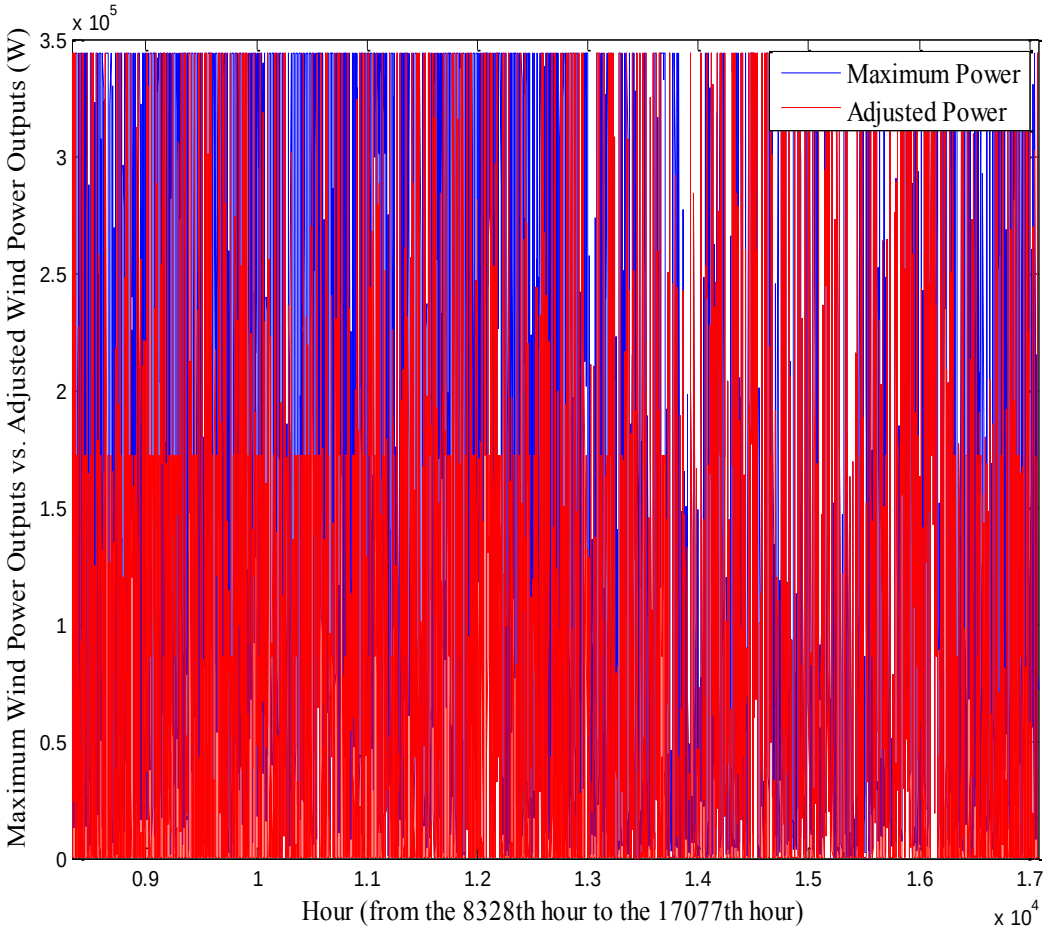

Figure 61. Real-time maximum wind power outputs and adjusted wind power outputs.

Figure 62 displays the blade pitch angles, the tip speed ratios, and the wind power efficiencies of the rated $2kW$ wind turbine with doubly-fed induction generator, which yields to the adjusted wind power outputs as shown in Figure 61. The upper sub figure displays the adjusted blade pitch angles β from the 8328^{th} hour to the 8735^{th} hour; the middle sub figure displays the adjusted tip speed ratios λ ; the lower sub figure displays the wind power extraction fractions based on the adjusted blade pitch angles β and the adjusted tip speed ratios λ by using Equations 3.33 and 3.34. Initially, the blade pitch angles β are set to zero for the maximum wind power extraction at a certain wind speed. However, the blade pitch angles are increased at

some hours. These changes reduced the wind power extraction fraction and resulted in lower wind power outputs.

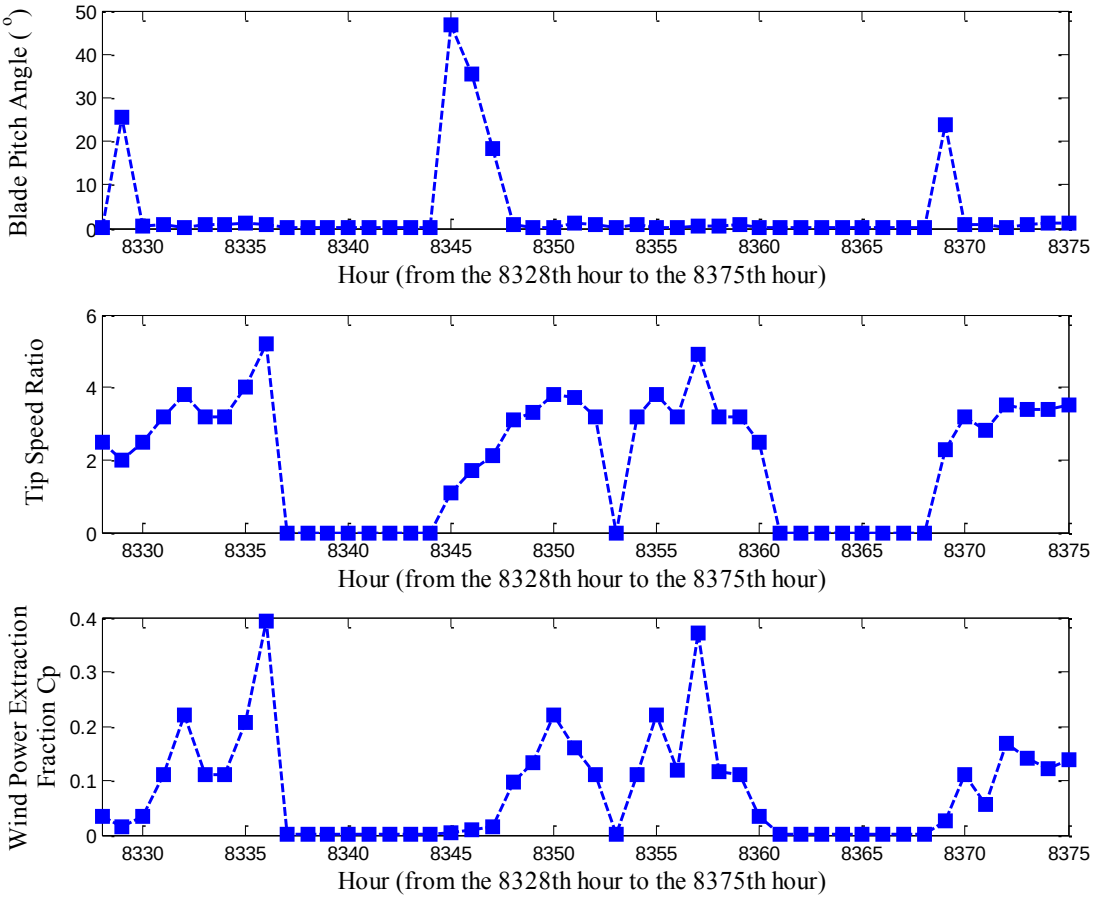

Figure 62. Real-time adjusted pitch angle, tip speed ratio and power efficiency.

6.4 Transient Performances of the DRGs and DES

In this section, the snapshots of the microgrid transient performance will be presented, including the wind power conversion system, the solar power conversion system, and the distributed energy storage.

6.4.1 Wind power conversion system transient performance analysis The initial values and the target values of the wind power systems for the transient performance analysis are shown in Table 10.

Table 10

Initial and Target Values of the Wind Power Systems for Transient Performance Analysis

	Initial Value	Target Value
Active Power (W)	500	1000
Reactive Power (Var)	-94.2733	-180.936
Pitch Angle (degree)	0.1	25.6
Tip Speed Ratio	2.5	2
Wind Speed (m/s)	4.4719	7.432

Figure 63 displays the changings of the wind speed and the rotor angular speed.

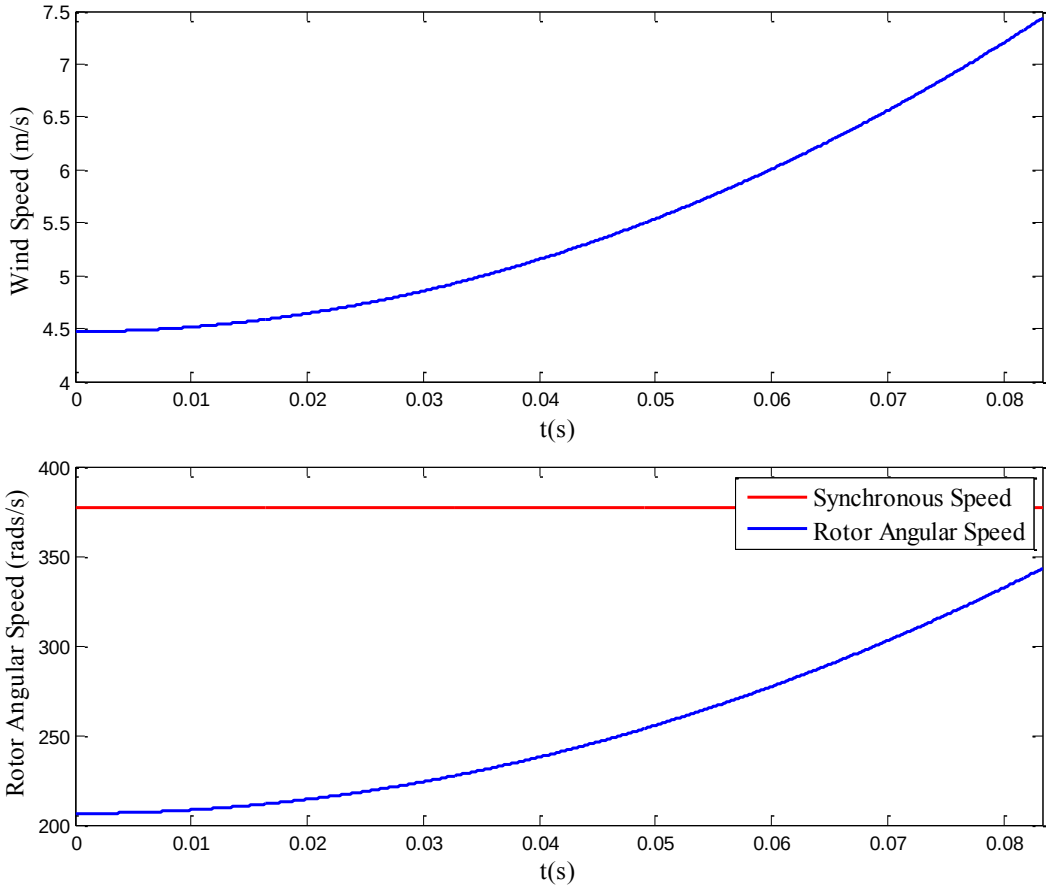

Figure 63. Wind speed and rotor angular speed acceleration.

The wind speed is increasing from 4.47 m/s to 7.43 m/s in 83.3 milliseconds. As a result, the rotor angular speed responses to the changings of the wind speed, and is increasing

from 206.39 $rads/s$ to 342.96 $rads/s$. However, it is still below the system synchronous speed 376.99 $rads/s$, and the doubly-fed induction generator will operate in the sub-synchronous mode.

Figure 64 displays the PI controlled rotor currents in the direct and quadrature axes. When the DFIG is in the sub-synchronous mode, the rotor absorbs the power from the grid, and the rotor side converter manipulates the voltage frequency for compositing the difference between the synchronous angular speed and the rotor rotating speed. The above procedure is accomplished by the rotor side converter and its PI controllers.

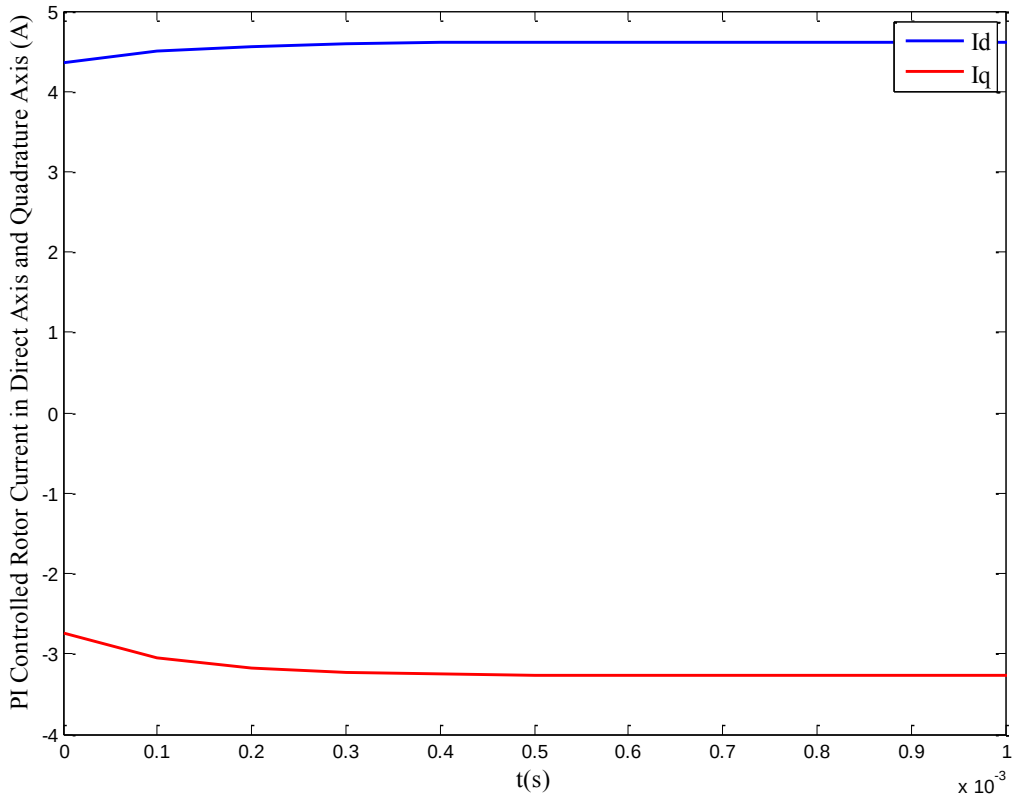

Figure 64. PI controlled rotor currents in direct and quadrature axes.

The stator active and reactive powers are only controlled by the rotor side currents in the direct and quadrature axes. The integral gain and the proportional gain of the PI controllers for

rotor side currents are $K_p = K_i = 100$. As shown in Figure 64, the rotor currents in the direct axis approached the target value in $0.4ms$, and the rotor currents in the quadrature axis approached the target value in $0.5ms$.

Figure 65 displays the rotor voltages in the direct and quadrature axes.

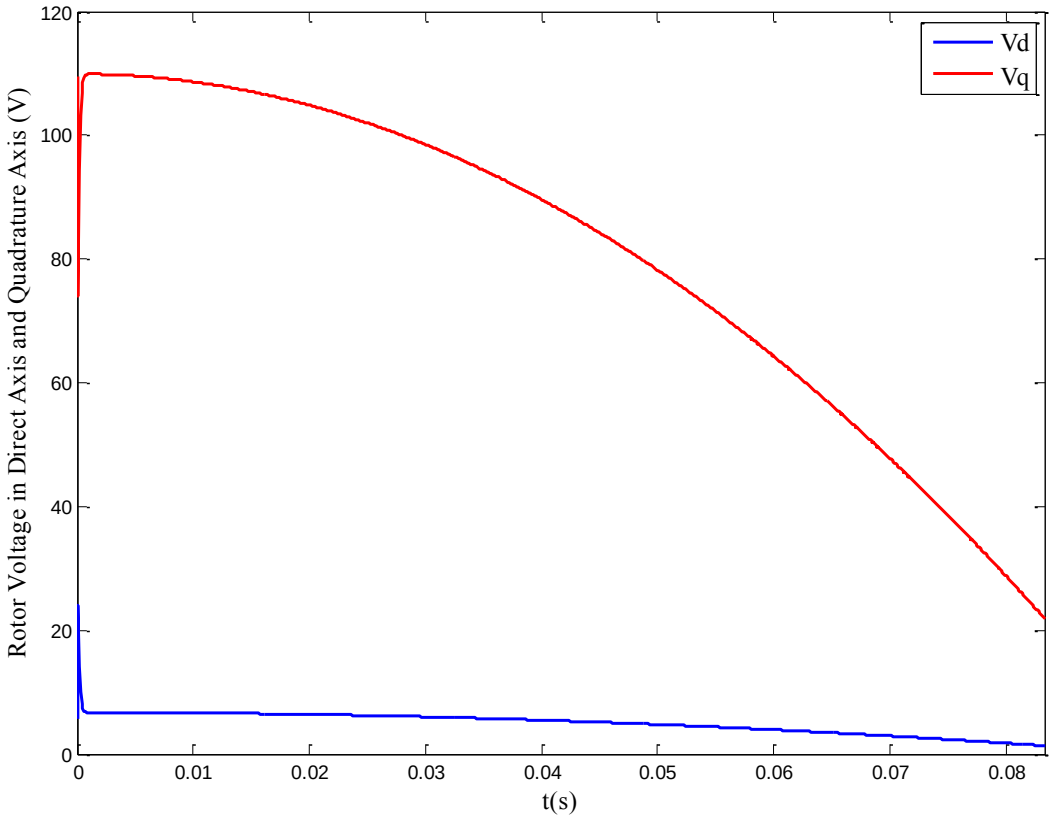

Figure 65. Rotor voltages in the direct and quadrature axes.

The rotor side voltages partially depend on the rotor currents in the direct and quadrature axes. The other parameter decides the rotor voltages is the slip frequency, which is equal to the difference between the synchronous speed and the rotor angular speed, $\omega_s - \omega_r$, as shown in Equations 3.65 and 3.66. The rotor currents in the direct and quadrature axes are settled down in

$0.5ms$, but the rotor voltages in the direct and quadrature axes are still changing, because the rotor rotating angular speed is keeping changing.

Figure 66 displays the Phase A rotor current and voltage. The rotor voltages in the direct and quadrature axes are the mathematical variables. In practice, they should return to the three phase forms as the reference signals for the converter switching control.

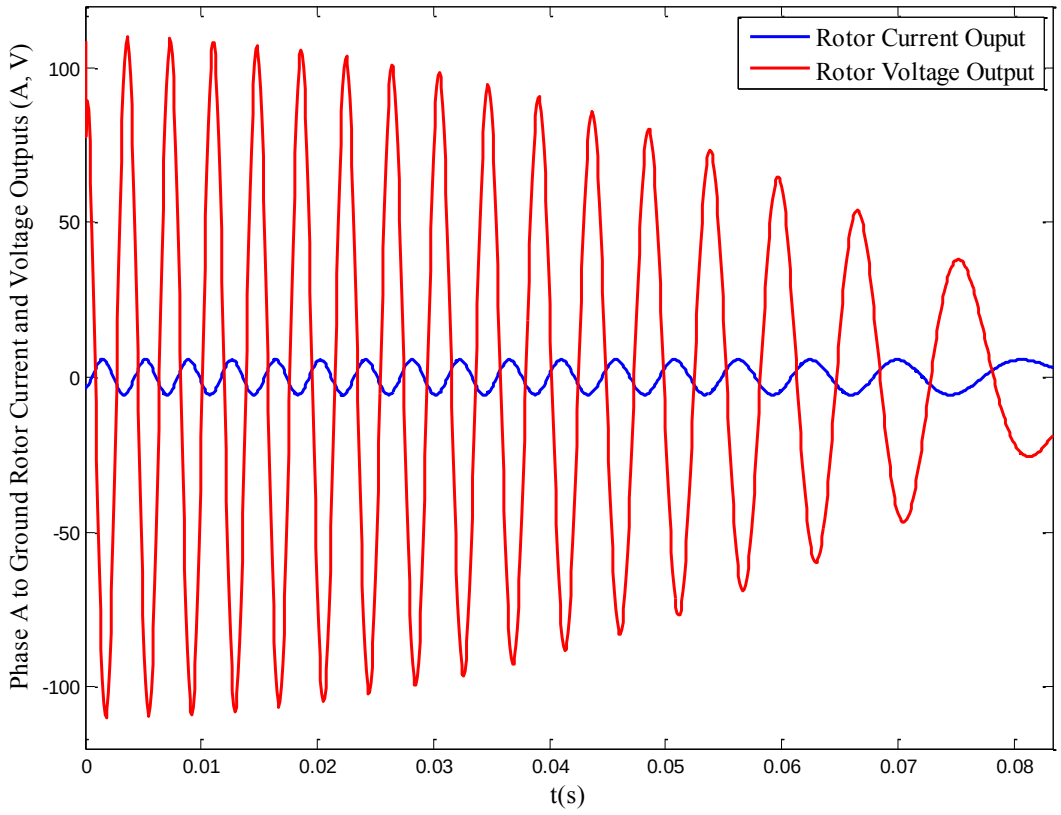

Figure 66. Rotor current phase A and voltage phase A.

As shown in Figure 66, the magnitude of the rotor voltage is decreasing and the magnitude of the rotor current changes slightly. Because the wind speed is increasing and more wind energy is extracted by the wind turbines, the rotor will absorb less power from the microgrid, which is the main reason that the rotor voltage magnitude drops. Because both the

wind speed and the rotor angular rotating speed are increasing, the slip frequency is reducing. As a result, the frequencies of the rotor voltage and the rotor current are dropping.

Figure 67 displays the rotor and stator side active and reactive power outputs.

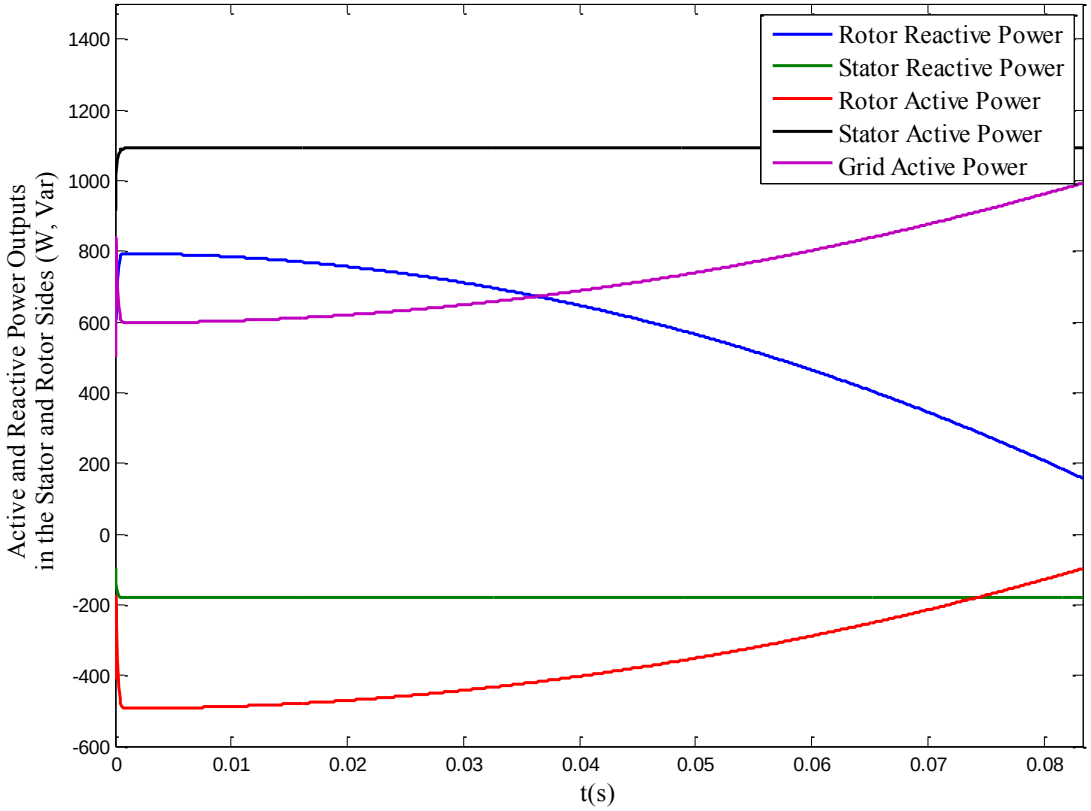

Figure 67. Rotor and stator active and reactive power.

Initially, the rotor side reactive power is used to establish the electromagnetic field, which bridges the stator side and the rotor side as an energy transfer channel. However, if the stator side voltage remains or approaches a high level. The rotor side reactive power only builds the potential on the rotor side leakage reactance, which introduces the leakage flux. In Figure 66, the magnitude of the rotor voltage is decreasing, so the rotor reactive power is decreasing as well. The stator side reactive power is decided by the rotor current in the direct axis only. When the rotor current in the direct axis approached to its target value, the stator reactive power will not

change anymore. The rotor side active power absorbed from the grid is decreasing due to more and more energy is extracted by the wind turbine and fed to the DFIG. The stator side active power is decided by the rotor current in the quadrature axis only. When the rotor current in the quadrature axis approached to its target value, the stator active power will not change anymore.

6.4.2 Solar power conversion system transient performance analysis The initial values and the target values of the solar power systems for the transient performance analysis are shown in Table 11.

Table 11

Initial and Target Values of the Solar Power Systems for Transient Performance Analysis

	Initial Value	Target Value
Active Power (W)	6.0563	42.4997
Terminal DC Voltage (V)	22.4	24.9
Global Solar Radiation (W/m2)	36.3008	227.2871
Air Temperature (C˚)	18.1448	18.3977

The upper graph in Figure 68 displays PI controlled DC/AC inverter currents in the direct and quadrature axes. The DC/AC inverter is the last electronic interface mounted at the terminal of the solar power conversion system, which is aim to transfer the DC power to AC power from the solar panel side to the generation bus. The above procedure is accomplished by the DC/AC inverter and its PI controllers. The integral gain and the proportional gain of the PI controllers are $K_p = K_i = 3$. As shown in Figure 68, the current in the quadrature axis approached the target value in $0.25ms$. The current in the direct axis is zero, because the solar power systems are not responsible for generating the reactive power. The lower graph in Figure 68 displays the currents in AC waveforms, and the waveform modulation is completed in $0.3ms$.

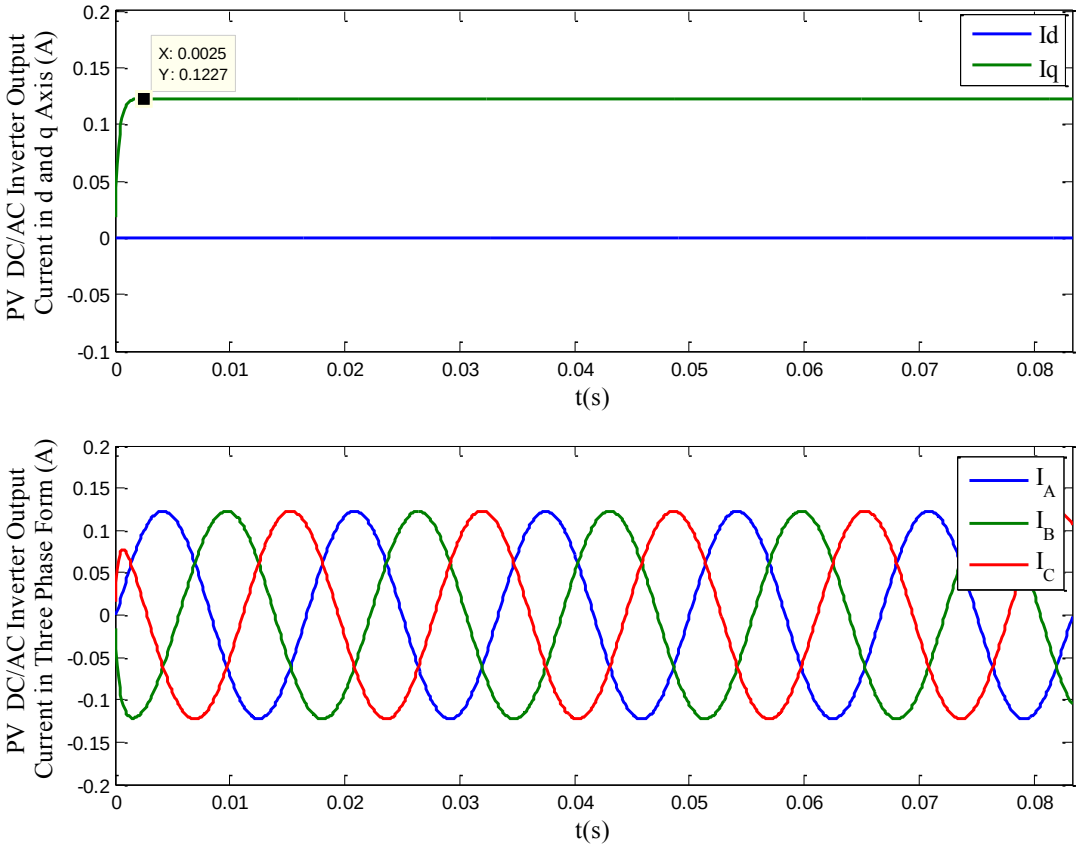

Figure 68. PV DC/AC inverter current output in direct and quadrature axes and three phase form.

The upper graph in Figure 69 displays the DC/AC inverter voltage in the direct axis. The middle graph in Figure 69 displays the DC/AC inverter voltage in the quadrature axis. The DC/AC inverter voltages in the direct and quadrature axes depend on the PI controlled currents in direct and quadrature axes. As shown in Figure 69, the voltage in direct axis approached the target value in $0.2ms$, and the voltage in quadrature axis approached the target value in $0.2ms$ as well. The reason that the voltage in the direct axis did not remain zero is that the voltage will drop through the impendence of connection conduct between the solar power conversion systems and the generation bus. The lower graph in Figure 69 displays the DC/AC inverter voltage in AC waveforms. Because of the changing of voltages in the direct and quadrature axes are small, the change of voltage in AC waveform is small as well.

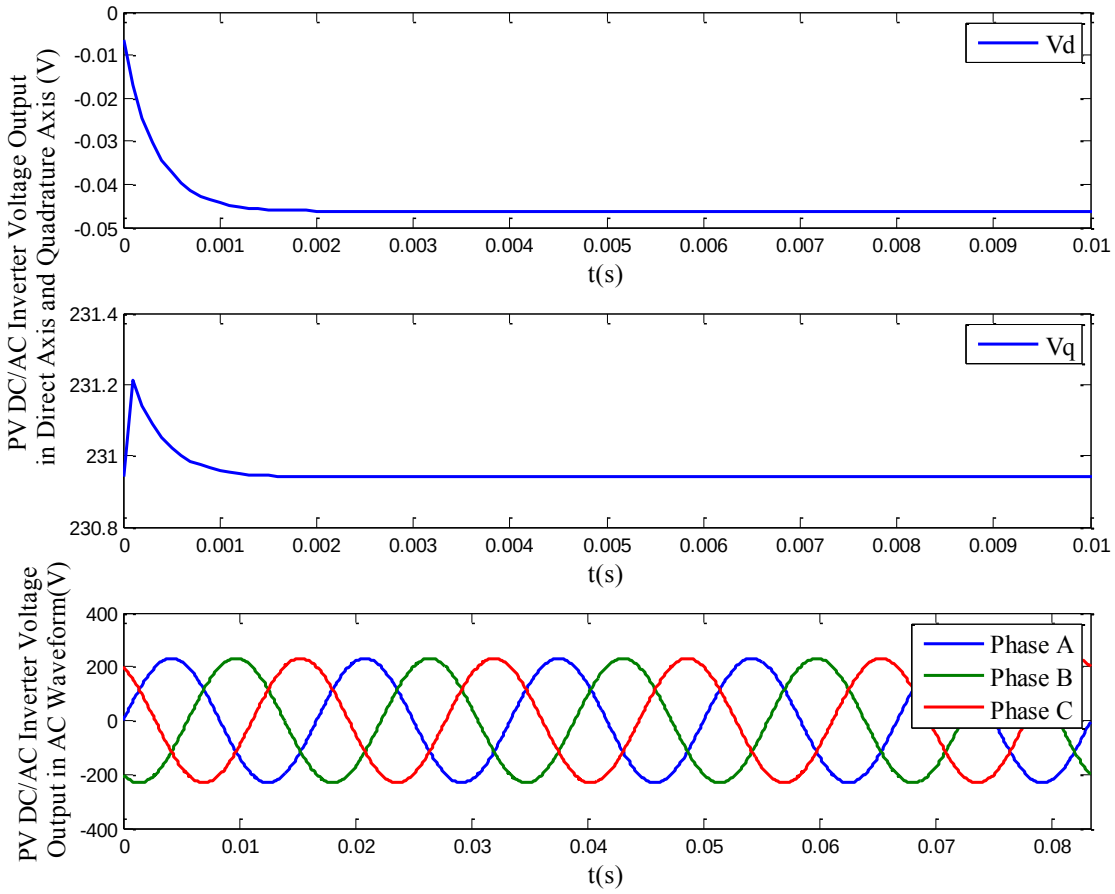

Figure 69. PV DC/AC inverter voltage output in direct and quadrature axes and three phase form.

Figure 70 displays the active power and the reactive power outputs from the DC/AC inverter. It is obviously that the initial active power output approaches the target value in $5ms$. The solar panel system is not proposed to generate the reactive power in the microgrid. Recall the upper graph in Figure 69, the small amount decrement in the direct axis is the voltage drop over the conduct, which connects the DC/AC inverter to the generation bus. In the viewpoint of the generation bus, there is no reactive power delivered from the solar power conversion. The reactive power output displayed in Figure 70 also demonstrates this fact.

6.4.3 Distributed energy storage transient performance analysis The initial, the intermediate, and the final active and reactive power injections or ejections of the distributed energy storage for the transient performance analysis are shown in Table 12.

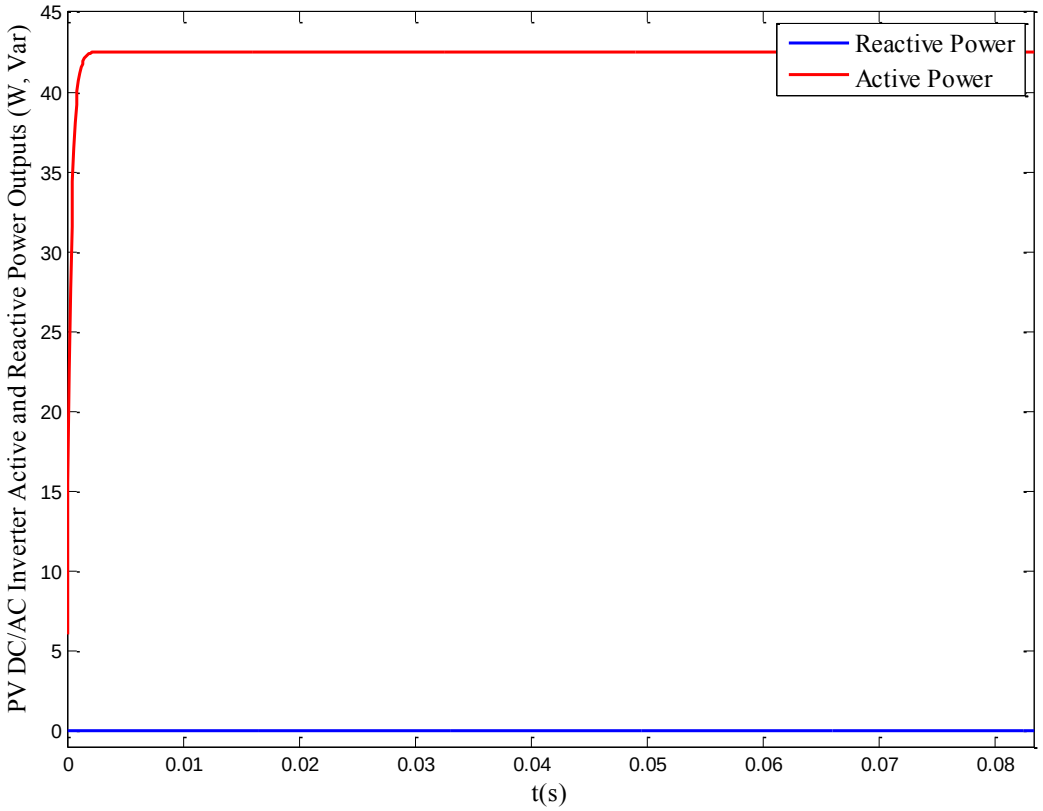

Figure 70. Active and reactive power outputs from the DC/AC inverter at the terminal of the solar power system.

The upper graph in Figure 71 displays PI controlled DC/AC inverter currents in the direct and quadrature axes. The DC/AC inverter is the last electronic interface mounted on the distributed energy storage, which is aim to transfer the DC power to the AC power required for balancing the power flow in the microgrid, and synchronize the output voltage vector to the swing bus voltage vector. The above procedure is accomplished by the DC/AC inverter and its PI controllers. The integral gain and the proportional gain of the PI controllers for the currents in the direct and quadrature axes are $K_p = K_i = 100$. The lower graph in Figure 71 displays the currents in AC forms, and the phase angles of the phase to ground currents are shifted twice in 0.25 second.

Table 12

Initial, Intermediate and Final Values of Active and Reactive Power Outputs from the Distributed Energy Storage for Transient Performance Analysis

	Initial State	Intermediate State	Final State
Active Power (W)	-2000	2000	-2000
Reactive Power (Var)	-5000	-5000	5000

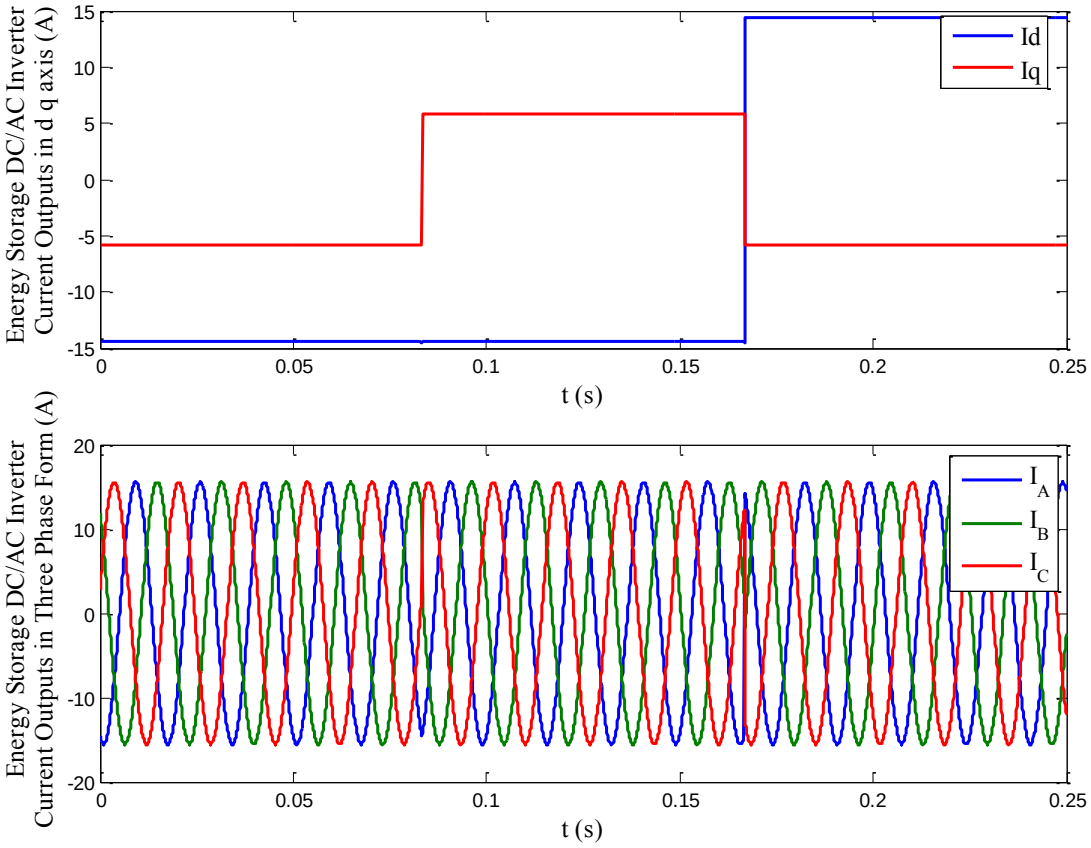

Figure 71. PI controlled ES DC/AC inverter current output in d, q axes and three phase form.

The upper graph in Figure 72 displays the DC/AC inverter voltages in the direct and quadrature axes. The lower graph in Figure 72 displays the DC/AC inverter voltage outputs in the AC waveforms. The DC/AC inverter voltages in the direct and quadrature axes depend on the PI controlled currents in direct and quadrature axes. As shown in Figure 72, the voltages in

the direct and quadrature axes approached the target value instantly. The reason that the voltage ripples occur is that the voltages are proportion to the derivations of the currents. If the currents in the direct and quadrature axes change a large amount rapidly, the voltage pulses occur. The lower graph displays the DC/AC inverter voltages in the AC waveform. Because of the reactive power output is increasing, the magnitudes of the voltages are increasing as well.

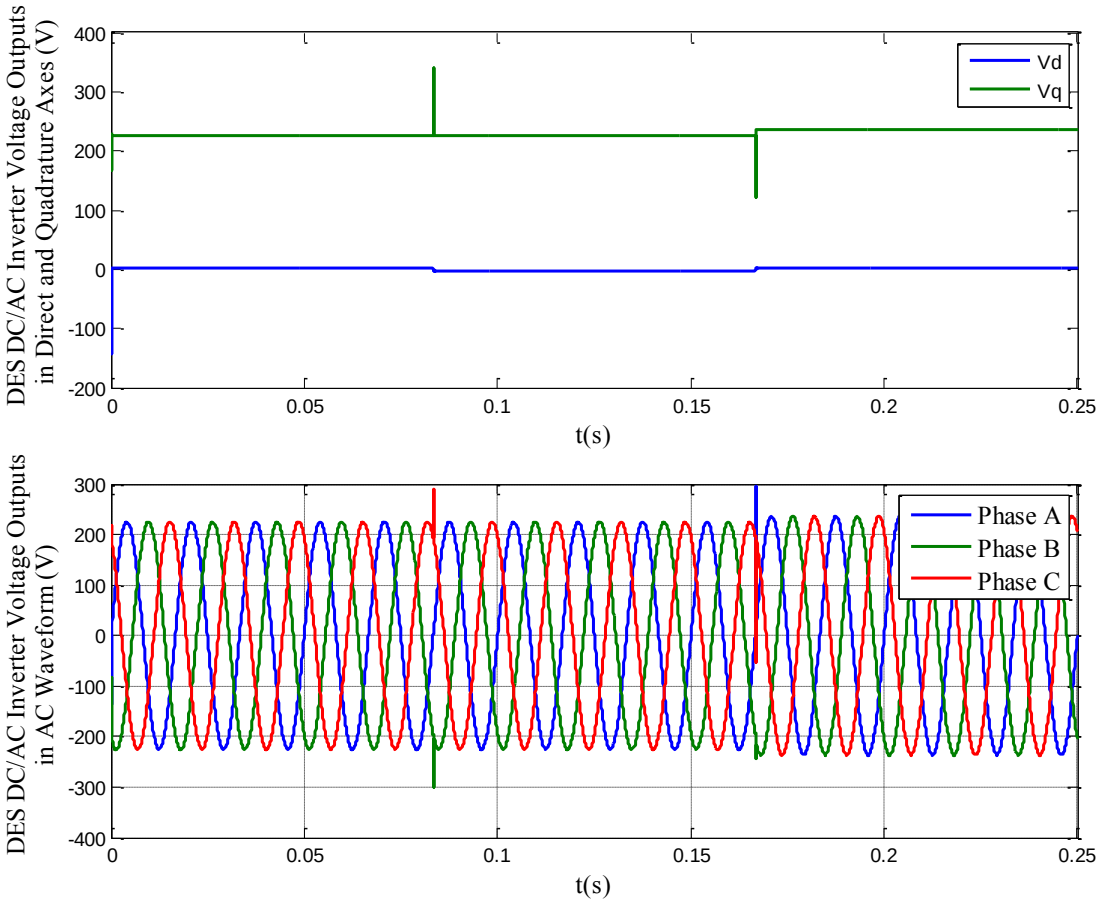

*Figure 72. D*ES DC/AC inverter voltage output in direct and quadrature axes and in three phase form.

Figure 73 displayed the active power and the reactive power outputs from the DC/AC inverter. It is obviously that the transitions between different states are instant. The distributed energy storage responded to the required active and reactive power from the swing bus fast and accurately.

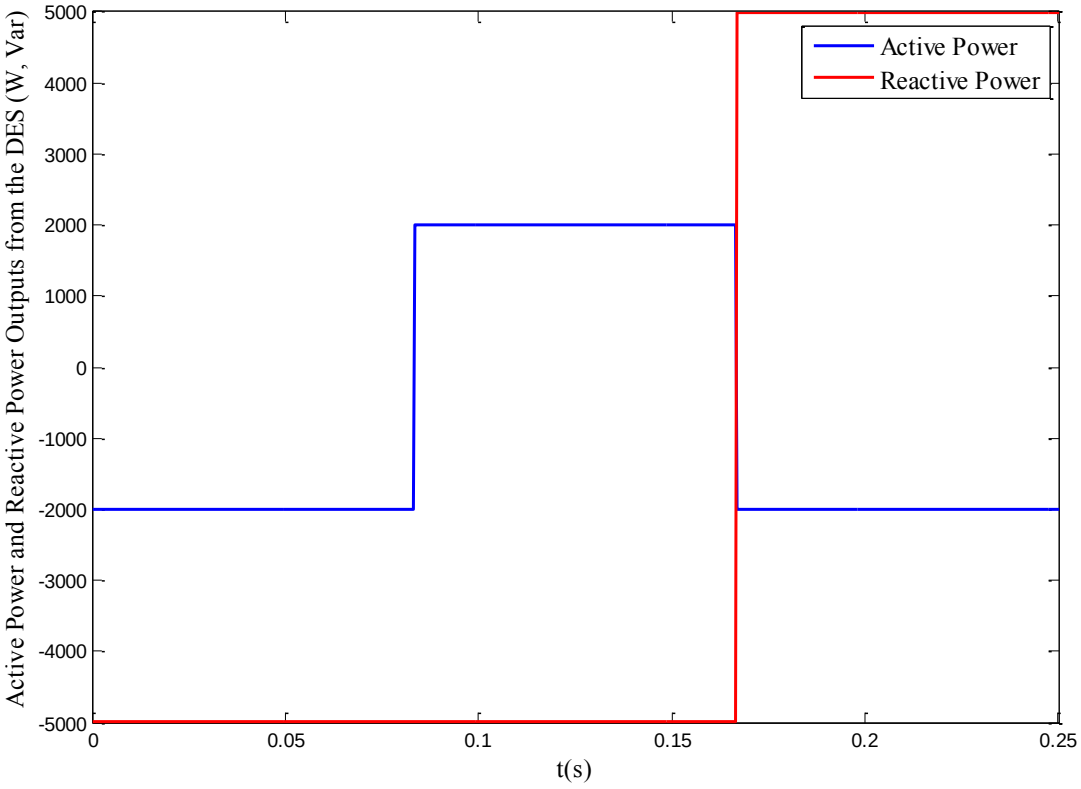

Figure 73. Active power and reactive power outputs from the distributed energy storage.

6.5 Comparison with Other Energy Storage State of Charge Estimation Method

The core of the energy manager is the method applied to predict the state of charge of the distributed energy storage.

In 2005, Bhangu et al. proposed an extended Kalman filter (EFK) based technique for the real time prediction of state of charge of the lead-acid cells [60]. They stated their EKF based method consistently provides estimates of the measured values within 2% average error in their 1300 second battery discharging simulation.

In 2012, Mishra et al. presented their smart charge study on energy storage state of charge prediction by using the support vector machine technology after they experimented with different linear regression models, including the least squares method and different regularized

models: LASSO, Elastic-Net, and Ridge Regression [61]. Table 13 listed the performances of these models for predicting the hourly SOC over 40days.

Table 13

Average Prediction Error (%) over 40 Days Sample Period for SVM with Different Kernel Functions, and the Best Linear Regression Model Elastic-Net

Prediction Model	Average Error
Elastic-Net	37%
SVM-Linear	29.50%
SVM-RBF	42.51%
SVM-Polynomial	5.75%

Compared with their results [61], the average testing predicted error (%) by using the BPN based energy manager in this research over 365 days sample period for the hourly state of charge of the distributed energy storage is 0.0704%, which is much better than the results presented in [61].

CHAPTER 7

Conclusion and Future Work

7.1 Conclusion and Contribution

This research proposed a biologically inspired method to design the energy manager, which is able to coordinate the standalone operation of the hybrid renewable residential microgrid.

In the first phase of this dissertation, a novel optimization procedure is presented to minimize the overall cost of the different types of renewable distribution generators based on the metrological features of the given location and its residential load profile. The non-uniform simulated annealing algorithm applied is capable of searching the space uniformly at the early stages and locally at the later stages, which improves the efficiency of optimal solution searching.

In the second phase of this research, the dynamic microgrid modeling allows the system performance analysis both in the steady and the transient states. The wind turbine with DFIG can operate in either the sub synchronization or the super synchronization model, which allows it generate energy in a wide range of the wind speeds. The dual channel converter system, which is mounted at the terminal end of the battery bank, allows the distributed energy storage sending or absorbing the real power and the reactive power from or to the microgrid bi-directionally. This advantage makes the distributed energy storage system be capable of balancing the power flows in the microgrid as a swing bus. The P, Q decoupling control based PI controllers adjust the current components in the direct and quadrature axes to the target values fast and accurately, which yields to the reliable reference signals sending to the power electronic interfaces.

In the third phase of this research, the energy management strategy is proposed and learnt by the back propagation neural network perfectly. According to the qualitative comparison with

other linear regression models and the support vector machine models with different kernel functions [61], the BPN based energy manager prediction performance is much better than those mentioned above. The BPN based energy manager predicts the state of charge (SOC) of the distributed energy storage system, and it yields to the reference values of the control variables of the power electronic interfaces. The system responds the desired operation conditions rapidly with the acceptable error. This result presents a fact that the biologically inspired energy manager can implement the proposed energy management strategy after the self-learning procedure, which will effectively promote the microgrid to the end users who are lack of the essential knowledge of the power system engineering.

7.2 Future Work

In this research, the micro grid is designed for the residential end users. It is interesting to apply the proposed methodologies to other types of the demands, such as military base in the remote area, outer space center, and other fields, which are out of the range of the conventional power systems.

The following technical topics are also suggested for future studies:

1. Impact of unbalanced load on the control and behavior of the microgrid in the autonomous mode.
2. The effective strategy development of the energy storage system in the grid-connected mode.
3. Impact of shadow on the surface of the PV panels on the control and behavior of the microgrid.
4. Impact of voltage dip on the stator of the DFIG.
5. End user load control and battery size optimization in the grid autonomous mode.

6. The generalization ability for the bio-inspired energy manager for the multiple microgrids coupling.

References

[1] Eto J., Lasseter R., Schenkman B., Stevens J., Volkommer H., Klapp D., Linton E., Hurtado H., Roy J. and Lewis N., "CERTS Microgrid Laboratory Test Bed," Consortium for Electric Reliability Technology Solutions (CERTS), 2008.

[2] Bae I. and Kim J., "Reliability Evaluation of Customers in a Microgrid," IEEE Trans. on Power Systems, pp. 1416-1422, 2008.

[3] Jayawarna N., Jenkins N., Barnes M., Lorentzou M., Papthanassiou S. and Hatziagyriou N., "Safety Analysis of a Microgrid Amsterdam," in *International Conf. on Future Power Systems*, Amsterdam, 2005.

[4] King D. and Morgan M., "Customer-Focused Assessment of Electric Power Microgrids," *Journal of Energy Engineering*, pp. 150-164, 2007.

[5] Barker P. and De Mello R., "Determining the Impact of Distributed Generation on Power Systems. I. Radial Distribution Systems," *Power Engineering Society Summer Meeting, IEEE*, pp. 1645-1656, 2000.

[6] Soman S., Zareipour H., Malik O. and Mandal P., "A Review of Wind Power and Wind Speed Forecasting Methods with Different Time Horizons," *North American Power Symposium (NAPS)*, pp. 1-8, 2010.

[7] Corotis R., Sigl A. and Klein J., "Probability Models of Wind Velocity Magnitude and Persistence," *Solar Energy*, pp. 483-493, 1978.

[8] Skidmore E. and Tatarko J., "Stochastic Wind Simulation for Erosion Modeling," *Transactions of the ASAE 33.6*, pp. 1893-1899, 1990.

[9] Takle E. and Brown J., "Note on the Use of Weibull Statistics to Characterize Wind Speed

Data," *J. Appl. Meteor,* pp. 556-559, 1978.

[10] Van Donk S., Wagner L., Skidmore E. and Tatarko J., "Comparison of the Weibull Model with Measured Wind Speed Distributions for Stochastic Wind Generation," *Transactions of the ASAE,* pp. 503-510, 2005.

[11] Al-Fawzan M., "Methods for Estimating the Parameters of the Weibull Distribution," King Abdulaziz City for Science and Technology, Riyadh, 2000.

[12] Nakanishi F., Ikegami T., Ebihara K., Kuriyama S. and Shiota Y., "Modeling and Operation of a 10 kW Photovoltaic Power Generator Using Equivalent Electric Circuit Method," in *Photovoltaic Specialists Conference,* Anchorage, 2000.

[13] Assuncao H., Escobedo J. and Oliveira A., "Modelling Frequency Distributions of 5 Minute-Averaged Solar Radiation Indexes using Beta Probability Functions," *Theoretical and Applied Climatology,* pp. 213-224, 2003.

[14] Yaramoglu M., Brinsfield R. and Muller E., "Estimation of Solar Radiation using Stochastically Generated Cloud Cover Data," *Energy in Agriculture,* pp. 227-242, 1985.

[15] Skoplaki E. and Palyvos J., "Operating Temperature of Photovoltaic Modules: A Survey of Pertinent Correlations," *Renewable Energy,* pp. 23-29, 2009.

[16] Agalgaonkar A., Dobariya C., Kanabar M., Khaparde S. and Kulkarni S., "Optimal Sizing of Distributed Generators in MicroGrid," in *Power India Conference,* New Delhi, 2006.

[17] C. Wang, M. Liu and L. Guo, "Cooperative Operation and Optimal Design for Islanded Microgrid," *Innovative Smart Grid Technologies (ISGT), IEEE,* pp. 1-8, 2012.

[18] Aarts E. and Van Laarhoven P., "Statistical Cooling: A General Approach to Combinatorial Optimization Problems," *Philips Journal of Research,* pp. 193-226, 1985.

[19] Faigle U. and Kern W., "Note on the Convergence of Simulated Annealing Algorithms," *SIAM Journal on Control and Optimization,* pp. 153-159, 1991.

[20] Gidas B., "Nonstationary Markov Chains and Convergence of the Annealing Algorithm," *Journal of Statistical Physics,* pp. 73-131, 1985.

[21] Granville V., Kriv ánek M. and Rasson J., "Simulated Annealing: A Proof of Convergence," *Pattern Analysis and Machine Intelligence, IEEE Transactions on* , pp. 652-656, 1994.

[22] Johnson A. and Jacobson S., "A Class of Convergent Generalized Hill Climbing Algorithms," *Applied Mathematics and Computation,* pp. 359-373, 2002.

[23] Lundy M. and Mees A., "Convergence of an Annealing Algorithm," *Mathematical Programming* , pp. 111-124, 1986.

[24] Mitra D., Romeo F. and Sangiovanni-Vincentelli A., "Convergence and Finite Time Behavior of Simulated Annealing," *Advances in Applied Probability,* pp. 747-771, 1986.

[25] Rossier Y., Troyon M. and Liebling T., "Probabilistic Exchange Algorithms and Euclidean Traveling Salesman Problems," *Operations-Research-Spektrum,* pp. 151-164, 1986.

[26] Michalewicz Z., Genetic Algorithms+ Data Structures= Evolution Programs, Springer, 1998.

[27] Zhao X., "Simulated Annealing Algorithm with Adaptive Neighborhood," *Applied Soft Computing,* pp. 1827-1836, 2011.

[28] Zhao X., Gao X. and Hu Z., "Evolutionary Programming Based on Non-uniform Mutation," *Applied Mathematics and Computation,* pp. 1-11, 2007.

[29] Yao X. and Liu Y., "Fast Evolution Strategies," *In Evolutionary Programming VI,* pp. 149-161, 1997.

[30] Yao X., Liu Y. and Lin G., "Evolutionary Programming Made Faster," *Evolutionary Computation, IEEE Transactions on*, pp. 82-102, 1999.

[31] Romeo F. and Sangiovanni-Vincentelli A., "A Theoretical Framework for Simulated Annealing," *Algorithmica*, pp. 302-345, 1991.

[32] Villalva M., Gazoli J. and Filho E., "Comprehensive Approach to Modeling and Simulation of Photovoltaic Arrays," *Power Electronics, IEEE Transactions on*, pp. 1198-1208, 2009.

[33] Deshmukh M. and Deshmukh S., "Modeling of Hybrid Renewable Energy Systems," *Renewable and Sustainable Energy Reviews*, pp. 235-249, 2008.

[34] Skoplaki E. and Palyvos J., "On the Temperature Dependence of Photovoltaic Module Electrical Performance: A Review of Efficiency/Power Correlations," *Solar Energy*, pp. 614-624, 2009.

[35] Crispim J., Micael C. and Rui C., "Validation of Photovoltaic Electrical Models Against Manufacturers Data and Experimental Results," in *Power Engineering, Energy and Electrical Drives, 2007. POWERENG 2007. International Conference on*, Setubal, 2007.

[36] De Soto W., Klein S. and Beckman W., "Improvement and Validation of a Model for Photovoltaic Array Performance," *Solar Energy*, pp. 78-88, 2006.

[37] Hussein K., Muta I., Hoshino T. and Osakada M., "Maximum Photovoltaic Power Tracking: an Algorithm for Rapidly Changing Atmospheric Conditions," *In Generation, Transmission and Distribution, IEE Proceedings-*, pp. 59-64, 1995.

[38] Kou Q., Klein S. and Beckman W., "A Method for Estimating the Long-Term Performance of Direct-Coupled PV Pumping Systems," *Solar Energy*, pp. 33-40, 1998.

[39] Ventre J., Photovoltaic Systems Engineering, CRC PressI Llc, 2004.

[40] Wens M. and Steyaert M., Design and Implementation of Fully-Integrated Inductive DC-DC Converters in Standard CMOS, Springer, 2011.

[41] Rashid M., Power Electronics: Circuits, Devices, and Applications, Pearson/Prentice Hall, 2004.

[42] Johnson G., Wind Energy Systems, Prentice Hal, 1985.

[43] Slootweg J., De Haan S., Polinder H. and Kling W., "General Model for Representing Variable Speed Wind Turbines in Power System Dynamics Simulations," *Power Systems, IEEE Transactions on*, pp. 144-151, 2003.

[44] Muyeen S., Tamura J. and Murata T., Stability Augmentation of a Grid-Connected Wind Farm, Springer, 2009.

[45] Barambones O., "Sliding Mode Control Strategy for Wind Turbine Power Maximization," *Energies*, pp. 2310-2330, 2012.

[46] Hofmann W. and Okafor F., "Optimal Control of Doubly-Fed Full-Controlled Induction Wind Generator with High Efficiency," in *In Industrial Electronics Society, 2001. IECON'01. The 27th Annual Conference of the IEEE*, 2001.

[47] Hopfensperger B., Atkinson D. and Lakin R., "Stator-Flux-Oriented Control of a Doubly-Fed Induction Machine with and without Position Encoder," *In Electric Power Applications, IEE Proceedings-*, pp. 241-250, 2000.

[48] Krause P., Wasynzuk O. and Sudhoff S., Analysis of Electric Machinary and Drive Systems, 2nd Edition, IEEE Wiley-IEEE Press, 2002.

[49] Qiao W., "Dynamic Modeling and Control of Doubly Fed Induction Generators Driven by Wind Turbines," *In Power Systems Conference and Exposition, 2009. PSCE'09. IEEE/PES*,

pp. 1-8, 2009.

[50] Tapia A., Tapia G., Ostolaza J. and Saenz J., "Modeling and Control of a Wind Turbine Driven Doubly Fed Induction Generator," *Energy Conversion, IEEE Transactions on,* pp. 194-204, 2003.

[51] Wu B., Dougal R. and White R., "Resistive Companion Battery Modeling for Electric Circuit Simulations," *Journal of Power Sources* , pp. 186-200, 2001.

[52] Chakraborty A., Musunuri S., Srivastava A. and Kondabathini A., "Integrating STATCOM and Battery Energy Storage System for Power System Transient Stability: A Review and Application," *Advances in Power Electronics,* pp. 1-12, 2012.

[53] Grainger J. and Stevenson W., Power System Analysis, New York: McGraw-Hil, 1994.

[54] Werbos P., "Beyond Regression: New Tools for Prediction and Analysis in the Behavioral Science," *PhD Thesis, Committee on Applied Mathematics, Harvard University,* 1974.

[55] Rumelhart D., Hinton G. and Williams R., "Learning Representations by Back-Propagating Errors," *Nature,* pp. 533-536, 1986.

[56] Haykin S., Neural Network: A Comprehensive (2nd Edition), Prentice Hall, 1998.

[57] EROCT, "Hourly Load Data Archives," 2013. [Online]. Available: http://www.ercot.com/gridinfo/load/load_hist/.

[58] USEIA, "Electricity Data Information," 2011. [Online]. Available: http://www.eia.gov/electricity/data.cfm.

[59] NREL, "Solar Resource & Meteorological Assessment Project," 2013. [Online]. Available: http://www.nrel.gov/midc/ssrp/.

[60] Bhangu B., Bentley P., Stone D. and Bingham C., "Nonlinear Observers for Predicting

State-of-Charge and State-of-Health Prediction of Lead-Acid Batteries for Hybrid Electric Vehicles," *Vehicular Technology, IEEE Transactions on* , pp. 783 - 794, 2005.

[61] Mishra A., Irwin D., Shenoy P., Kurose J. and Zhu T., "Smart Charge: Cutting the Electricity Bill in Smart Homes with Energy Storage," in *In Proceedings of the 3rd International Conference on Future Energy Systems: Where Energy, Computing and Communication Meet*, Madrid, 2012.

Appendix

Table A-1

Manufacture Data Sheet of KC200GT Solar Cell

I_{mp} (A)	76.1
V_{mp} (V)	26.3
$P_{\max}$ (W)	200.0863
I_{sc} (A)	8.21
V_{oc} (V)	32.9
$I_{o,n}$ (A)	9.8254×10^{-8}
I_{pv} (A)	8.2117
A	1.3
R_p (Ω)	1165.6
R_s (Ω)	0.2382
NOCT (C^o)	47.5

Table A-2

Parameters of Wind Turbine with Rate 2kW Doubly Fed Induction Generator

Blade Length (m)	6.5
Moment of Inertia of One Mass Drive Train ($kg \cdot m^2$)	0.002
Gear Ratio	150
Rotor Self Reactance (H)	0.1568
Rotor Resistance (Ω)	0.001
Rotor Leakage Reactance (H)	0.0156
Stator Self Reactance (H)	0.1554
Stator Resistance (Ω)	0.001
Stator Leakage Reactance (H)	0.0155
Mutual Reactance (H)	0.15
Pair of Poles	2